National Library
of Canada

Bibliothèque nationale
du Canada

Canadian Theses Service

Service des thèses canadiennes

Ottawa, Canada
K1A 0N4

NOTICE

The quality of this microform is heavily dependent upon the quality of the original thesis submitted for microfilming. Every effort has been made to ensure the highest quality of reproduction possible.

If pages are missing, contact the university which granted the degree.

Some pages may have indistinct print especially if the original pages were typed with a poor typewriter ribbon or if the university sent us an inferior photocopy.

Reproduction in full or in part of this microform is governed by the Canadian Copyright Act, R.S.C. 1970, c. C-30, and subsequent amendments.

AVIS

La qualité de cette microforme dépend grandement de la qualité de la thèse soumise au microfilmage. Nous avons tout fait pour assurer une qualité supérieure de reproduction.

S'il manque des pages, veuillez communiquer avec l'université qui a conféré le grade.

La qualité d'impression de certaines pages peut laisser à désirer, surtout si les pages originales ont été dactylographiées à l'aide d'un ruban usé ou si l'université nous a fait parvenir une photocopie de qualité inférieure.

La reproduction, même partielle, de cette microforme est soumise à la Loi canadienne sur le droit d'auteur, SRC 1970, c. C-30, et ses amendements subséquents.

NL-339 (r. 88/04) c

Canada

National Library
of Canada

Canadian Theses Service

Ottawa, Canada
K1A 0N4

Bibliothèque nationale
du Canada

Service des thèses canadiennes

The author has granted an irrevocable non-exclusive licence allowing the National Library of Canada to reproduce, loan, distribute or sell copies of his/her thesis by any means and in any form or format, making this thesis available to interested persons.

The author retains ownership of the copyright in his/her thesis. Neither the thesis nor substantial extracts from it may be printed or otherwise reproduced without his/her permission.

L'auteur a accordé une licence irrévocable et non exclusive permettant à la Bibliothèque nationale du Canada de reproduire, prêter, distribuer ou vendre des copies de sa thèse de quelque manière et sous quelque forme que ce soit pour mettre des exemplaires de cette thèse à la disposition des personnes intéressées.

L'auteur conserve la propriété du droit d'auteur qui protège sa thèse. Ni la thèse ni des extraits substantiels de celle-ci ne doivent être imprimés ou autrement reproduits sans son autorisation.

ISBN 0-315-55623-4

Canada

THE UNIVERSITY OF ALBERTA

REMOTE INDENTIFICATION OF RAIN AND HAIL WITH A POLARIZATION DIVERSITY RADAR

by

KAIS J.L. AL-JUMILY

A THESIS
SUBMITTED TO THE FACULTY OF GRADUATE STUDIES AND RESEARCH
IN PARTIAL FULFILMENT OF THE REQUIREMENTS FOR THE DEGREE
OF DOCTOR OF PHILOSOPHY
IN
METEOROLOGY

GEOGRAPHY

EDMONTON, ALBERTA
FALL, 1989

THE UNIVERSITY OF ALBERTA

RELEASE FORM

NAME OF AUTHOR KAIS J.L. AL-JUMILY

TITLE OF THESIS REMOTE INDENTIFICATION OF RAIN AND HAIL WITH A POLARIZATION DIVERSITY RADAR

DEGREE FOR WHICH THESIS WAS PRESENTED DOCTOR OF PHILOSOPHY

YEAR THIS DEGREE GRANTED FALL, 1989

Permission is hereby granted to THE UNIVERSITY OF ALBERTA LIBRARY to reproduce single copies of this thesis and to lend or sell such copies for private, scholarly or scientific research purposes only.

The author reserves other publication rights, and neither the thesis nor extensive extracts from it may be printed or otherwise reproduced without the author's written permission.

(SIGNED) Kais Al Jumily

PERMANENT ADDRESS:

Hay Almotanaby
603 - 38 - 48 - 1
BAGHDAD, IRAQ

DATED May 12, 1989

THE UNIVERSITY OF ALBERTA

FACULTY OF GRADUATE STUDIES AND RESEARCH

The undersigned certify that they have read, and recommend to the Faculty of Graduate Studies and Research, for acceptance, a thesis entitled REMOTE INDENTIFICATION OF RAIN AND HAIL WITH A POLARIZATION DIVERSITY RADAR submitted by KAIS J.L. AL-JUMILY in partial fulfilment of the requirements for the degree of DOCTOR OF PHILOSOPHY in METEOROLOGY.

Robert B. Charlton

Supervisor

Edward Lozowski

R. S. Humphries

E. R. Reinelt

J. D. Wilson

G. D. Cormack

Paul L. Smith

External Examiner

Date May 12, 1989

ABSTRACT

Measurements made with the Alberta Research Council 10-cm circular polarization diversity radar are compared with ground-based observations of precipitation to improve the use of polarization techniques for distinguishing hail from rain. Case studies involve light rain, heavy rain, and various mixtures of rain and hail. Cases are selected to represent the spectrum of precipitation rate, type, location, and duration.

Propagation effects due to precipitation between the radar and the target and the way in which they can be recognized and removed from the radar measurements are incorporated into the evaluation. These improve the interpretation of the data and thereby better determine the intrinsic polarization characteristics of precipitation particles.

Relationships between the reflectivity factor and the various polarization parameters are developed. They indicate that certain combinations of reflectivity and polarization measurements can be used to discriminate between rain and hail regions within storms and that neither reflectivity nor polarization measurements can be considered separately. Comparison of these results with the results of studies which used linear polarization indicates that the two approaches are comparable in terms of delineating the type of precipitation particles present.

A new technique for the remote identification of rain and hail with radar is developed. The method is based on a combination of the reflectivity and differential reflectivity derived from circular polarization measurements after propagation effects are removed. The theoretical rain-hail discrimination technique is tested on ground-based observations made by Alberta Research Council personnel. Next, simultaneous radar data and farmers' surface observations of rain and hail over large regions within the Alberta Hail Project areas are used to evaluate the technique. The results show that predicted hail regions correlate well with the surface hail pattern and that the combination of reflectivity and differential reflectivity offers a great improvement over the use of measurements consisting solely of reflectivity.

PREFACE

Since the development of radar meteorology in the late 1940's and early 1950's, there has been an increasing interest in the possibility of using radar to distinguish hailstorms from storms which give other types of precipitation. Although hail is generally more damaging to crops and property than is rain, the scientific drive behind such studies lies not in being able to determine which land locations received damaging hail but rather in being able to understand convective storms so that they might be modified by cloud seeding. Early attempts to detect and measure hail with radar employed measurements of the equivalent reflectivity factor Z_e (Cook, 1958; Douglas and Hitschfeld, 1958; Donaldson, 1961; Geotis, 1963; Pell, 1969). Z_e, which can be thought of as the echo strength corrected for range, is defined in terms equivalent to the sum of the sixth powers of the diameters of spherical liquid water scatterers within unit volume inside the radar illuminated volume. Consequently Z_e should be much larger for hailstones than for smaller particles, other factors being the same. It has been suggested (Pell, 1969) that when Z_e exceeds 43 dBz (dBz=dB above 1 mm^6m^{-3}), hail is likely to be present. However, these methods have not proved to be very successful for detecting hail, especially when Z_e does not reach 50 dBz (Bringi *et al.*, 1984).

McCormick (1968) introduced a more sophisticated technique based on the polarization properties of the precipitation particles. It utilized a polarization diversity radar which, after transmitting a circularly polarized pulse, measures, in addition to Z_e, the circular depolarization ratio CDR, the mean orientation angle ALD of the observed particles, and the degree of preferred orientation $ORTT$. This method has been adopted by the National Research Council of Canada and the Alberta Research Council to study severe storms and hailstorms over the past two decades. It has been reported in various journals by Barge (1972, 1974), Humphries (1974b), McCormick and Hendry (1976), Hendry *et al.* (1976), Hendry and Antar (1984a), and Torlaschi *et al.* (1984). A factor complicating this procedure is that propagation through heavy precipitation can change the circularly polarized pulse to the extent that the pulse becomes elliptically polarized when it reaches the observed cell. In such cases, the radar measurements are dominated by these propagation effects and not by the scattering properties of the precipitation particles within the observed cell (Humphries, 1974a). However, recent studies (Bebbington *et al.*, 1987; Jameson and Davé, 1988) have suggested that these propagation effects can be identified and removed from the measured data.

Another approach for hail detection with radar was proposed by Seliga and Bringi (1976). This method, which involves measurements of differential reflectivity Z_{DR} with a dual linear polarization radar, is still the subject of research in the United States (Bringi *et al.*, 1984; Aydin *et al.*, 1986) and the United Kingdom (Leito and Watson, 1984; Illingworth *et al.*, 1986). Basically, these two methods are closely related such that Z_{DR} can be derived from measurements of CDR and $ORTT$ (McCormick, 1979; Holt, 1984; Jameson, 1987).

The aim of this research is to improve the use of polarization diversity radar in discriminating rain from hail and to ascertain whether polarization techniques offer advantages over the use of measurements consisting solely of Z_e. All the measurements presented in this thesis were carried out with the Alberta Research Council's S-band polarization diversity radar, which is located at Red Deer airport in central Alberta, Canada.

Chapter I covers the basic principles of electromagnetic wave polarization and the use of polarization techniques in radar meteorology. Much of the material presented in this chapter are necessary for the theoretical developments in the successive chapters. Chapter II gives a comprehensive review of polarization studies of precipitation. The principles for the radar determination of the polarization properties of precipitation are discussed in Chapter III. These are necessary to understand how radar measurements are related to the shape, size distribution, and orientation of the scatterers. Chapter IV briefly describes the radar system, calibration procedures, and data processing. Attention is given to the phase calibration, and a method is developed by the author to analyze the calibration data and thus assure accuracy in extracting *ORTT* and *ALD* from the recorded raw data values. In Chapter V, theoretical calculations are carried out to demonstrate how propagation effects can corrupt the radar measurements. Observations of severe propagation effects selected from the ARC radar archives are used to confirm these calculations and to test the correction methods mentioned above. Chapter VI presents an analysis of simultaneous radar measurements and ground observations of different types of precipitation with the radar measurements corrected for propagation effects. The last section of Chapter VI discusses the relative sensitivity of various radar parameters to the presence of hail. Chapter VII describes a new rain and hail identification scheme based on a combination of the equivalent reflectivity factor and differential reflectivity derived from circular polarization measurements. Radar data and ground truth observations collected by the Alberta Research Council storm chase crew and by volunteer farmers are used to confirm and determine the effectiveness of polarization techniques in hail detection. Chapter VIII includes a summary, conclusions, and suggestions for future work.

ACKNOWLEDGMENTS

I would like to express my sincere appreciation to my supervisor, Dr. R. B. Charlton and to Dr. R. G. Humphries from the Alberta Research Council, now with MacDonald Dettwiler, for their invaluable advice and guidance throughout my years of study and research.

I am very grateful to the Resource Technologies Department of the Alberta Research Council for giving complete access to their facilities including computing resources, research trips to the radar site, and office space at their Edmonton headquarters. The staff of the RTD were very helpful and I would like to thank them for their time and effort. I would also like to express my gratitude to the professors and my colleagues of the Meteorology Division at the University of Alberta for their help and advice.

I wish to express special thanks to Dr. A. R. Holt and Dr. R. McGuinness from the University of Essex, England, for the many clarifying discussions. The assistance of Mrs. Leslie Phillips during the early stages of this work is also appreciated.

This research was financially supported by the Alberta Research Council, the University of Alberta, and the Atmospheric Environment Service of Environment Canada. ARC also provided funding to attend the 23rd Conference on Radar Meteorology, Snowmass, Colorado, September 22-26, 1986. This was very beneficial.

TABLE OF CONTENTS

PAGE

LIST OF TABLES xiv

LIST OF FIGURES xv

LIST OF SYMBOLS xxi

CHAPTER

I. REPRESENTATION OF ELECTROMAGNETIC WAVE POLARIZATION 1

The Monochromatic Plane Wave 1

Stokes Parameters 5

The Poincaré Sphere 6

The Quasi-Monochromatic Plane Wave 8

The Coherency Matrix 9

Polarization Techniques in Radar Meteorology 14

II. A REVIEW OF POLARIZATION STUDIES RELATED TO RADAR METEOROLOGY 17

Historical Overview 17

Polarization Diversity Radar Studies 18

Differential Reflectivity Studies 21

Investigations of Propagation Effects 22

CHAPTER PAGE

III. PRINCIPLES OF POLARIZATION DIVERSITY RADAR 25

Introduction 25

Network Representation 25

Propagation between Radar and the Scattering Target 28

Scattering by a Single Target 32

The Net Effects of Propagation and Scattering 35

The Received Signal from an Assembly of Particles 37

Relationship between Differential Reflectivity and Circular Polarization Parameters 42

Intrinsic Polarization Properties of Rain and Hail 45

IV. THE ALBERTA RESEARCH COUNCIL S-BAND RADAR 51

The Radar System 51

Calibration 58

Analysis of Phase Discriminator Calibration Data 63

Data Processing 70

Surface Observations of Precipitation 73

V. PROPAGATION EFFECTS 81

Introduction 81

Influence of Propagation on Circularly Polarized Radar 82

Methods for Correction of Propagation Effects 88

Evidence of Propagation Effects on the ARC Radar Data 92

CHAPTER PAGE

VI. POLARIZATION OBSERVATIONS OF RAIN AND HAIL 102

Introduction 102

Rain Observations 104

Hail Observations 111

Relationships between Z_e' and Polarization Parameters 125

VII. VERIFICATION OF POLARIZATION TECHNIQUES USING RAIN AND HAIL REPORTS FROM FARMERS 135

Identification Scheme and Evaluation Procedures 135

Observations from Three Storms 138

VIII. SUMMARY AND CONCLUSIONS 154

BIBLIOGRAPHY 158

APPENDIX A. Algorithm and Computer Programs Related to Phase Discriminator Calibration 164

A.1 Numerical Algorithm for Phase Shifter Calibration 164

A.2 Listing of Program SINE 167

A.3 Listing of Program GAMMA 170

APPENDIX B. Listing of Program JORTT 172

APPENDIX C. Representation of Circular Polarization Parameters in Terms of p and β 175

LIST OF TABLES

Table Page

4.1 The Alberta Research Council's S-band radar characteristics 54

4.2 Relationship between orientation of a dipole scatterer and the monitor orientation 67

4.3 Analysis of phase calibration data collected during 1983 71

5.1 Effect of propagation on uniform rain along a 10 km path for rain rates of 25, 50, 75, and 100 mm/hr 87

5.2 Comparison between methods for correction of propagation effects 93

LIST OF FIGURES

Figure Page

1.1 Illustrations of elliptical, linear, and circular polarizations 3

1.2 The polarization ellipse 4

1.3 The Poincaré sphere 7

1.4 The Poincaré sphere showing Stokes parameters normalized to $g_o = 1$ 13

3.1 Schematic representation of the network from the scattering target to the radar receivers 26

3.2 Relationship of symmetry axes of an anisotropic medium X_1Y_1Z and the basic coordinate system XYZ 29

3.3a Relationship between the coordinate system X_2Y_2Z attached to the scattering target and the basic coordinate system XYZ 33

3.3b Relationship between the reference axis of the scattering target and the X_2Y_2Z coordinate system. 33

3.4 Degree of orientation ρ_α versus standard deviation of canting angle σ_α 40

3.5 Relationship between Z_e and precipitation rate for an assembly of raindrops only at a temperature of $10^{\circ}C$ and a collection of wet hailstones at a temperature of $0^{\circ}C$ 47

Figure Page

3.6 Relationship between CDR and precipitation rate for an assembly of raindrops only at a temperature of $10^{\circ}C$ and a collection of wet hailstones at a temperature of $0^{\circ}C$ 48

3.7 Relationship between $ORTT$ and precipitation rate for an assembly of raindrops only at a temperature of $10^{\circ}C$ and a collection of wet hailstones at a temperature of $0^{\circ}C$ 49

3.8 Relationship between Z_{DR}^{c} and precipitation rate for an assembly of raindrops only at a temperature of $10^{\circ}C$ and a collection of wet hailstones at a temperature of $0^{\circ}C$ 50

4.1 Location and operational area of the ARC S-band radar 53

4.2 Block diagram of the antenna microwave circuitry of the ARC S-band radar 55

4.3 Block diagram of the receiver system of the ARC S-band radar 57

4.4 Graphs of the ARC S-band receiver calibration for port 1 and port 2 for 7 July 1984 59

4.5 Graphs of the ARC S-band phase shifter calibration for port 3 and port 4 for 7 July 1984 61

4.6 Graphs of the ARC S-band monitor calibration for port 3 and port 4 for 7 July 1984 62

4.7 Best-fit curves for the ARC S-band phase shifter calibration data for port 3 and port 4 for 7 July 1984 65

4.8 The orientation of a dipole scatterer with respect to the vertical as viewed by the radar 66

Figure		Page
4.9	Comparison of observed and calculated monitor calibration data for port 3 and port 4 for 7 July 1984	69
4.10	Plot of ORTT versus J	74
4.11	Standard scan of the ARC radar PPI display	75
4.12	An example of rain and hail observations collected by storm chase crew	76
4.13	Hail card format	78
4.14	An example of coded farmers' reports of rain and hail	79
4.15	Coding sheet for farmers' reports	80
5.1	PPI maps of Z_e, CDR, $ORTT$, and ALD for rain observations on 31 July 1982 at 1850 MDT at 1.3° elevation	94
5.2	Comparison between uncorrected and corrected radar parameters during rain observations on 31 July 1982 at 1850 MDT	96
5.3	Comparison between uncorrected and corrected radar parameters during rain observations on 24 July 1983 at 2039 MDT	98
5.4	Comparison between uncorrected and corrected radar parameters during observations of mixed rain and hail on 5 July 1984 at 1900 MDT	100
6.1	8 July 1983. Corrected radar observations along a radial at 1.7° elevation, 270° azimuth, at 1505 MDT	105
6.2	24 July 1983. PPI maps of corrected radar parameters at 1.6° elevation, at 2039 MDT	107

Figure Page

6.3 24 July 1983. Corrected radar observations along a radial at 1.6° elevation, 221° azimuth, at 2039 MDT 108

6.4 28 July 1983. Corrected radar observations along a radial at 1.8° elevation, 282° azimuth, at 1709 MDT 110

6.5 31 July 1983 Corrected radar observations along a radial at 1.9° elevation, 326° azimuth, at 1850 MDT 112

6.6 12 July 1983. Corrected radar observations along a radial at 1.5° elevation, 196° azimuth, at 1649 MDT 114

6.7 15 August 1983. PPI maps of corrected radar parameters at 1.3° elevation, at 1617 MDT 116

6.8 15 August 1983. Corrected radar observations along a radial at 1.3° elevation, 121° azimuth, at 1617 MDT 118

6.9a 15 August 1983. RHI map of Z_e' at 121° azimuth, at 1617 MDT 119

6.9b 15 August 1983. RHI map of CDR' at 121° azimuth, at 1617 MDT 120

6.9c 15 August 1983. RHI map of $ORTT'$ at 121° azimuth, at 1617 MDT 121

6.9d 15 August 1983. RHI map of $Z_{DR}^{c'}$ at 121° azimuth, at 1617 MDT 122

6.10 25 June 1984. Corrected radar observations for a radial at 1.3° elevation, 126° azimuth, at 1655 MDT 124

6.11 Scatter plot of CDR' versus Z_e' for three rain only storms and four rain and hail mixture storms 126

Figure Page

6.12 Scatter plot of $ORTT'$ versus Z_e' for three rain only storms and four rain and hail mixture storms 127

6.13 Scatter plot of $Z_{DR}^{c'}$ versus Z_e' for three rain only storms and four rain and hail mixture storms 128

6.14 Comparison between uncorrected and corrected data for the Z_e-CDR relationship 132

6.15 Comparison between uncorrected and corrected data for the Z_e-$ORTT$ relationship 133

6.16 Comparison between uncorrected and corrected data for the Z_e-Z_{DR}^{c} relationship 134

7.1 A 2 × 2 contingency table delineating all prediction-observation combinations that can result from comparing radar prediction to ground truth data of precipitation 137

7.2a Maximum Z_e' PPI map at 1.6° elevation for 2000-2100 MDT 24 July 1983 139

7.2b Predicted hail occurrences at 1.6° elevation for 2000-2100 MDT 24 July 1983 140

7.2c Surface observations of precipitation for 24 July 1983 compared to outlines of rain regions and hail regions predicted by a combination of Z_e' and $Z_{DR}^{c'}$ and by Z_e' 141

7.2d Contingency tables for the 24 July 1983 storm 142

7.3a Maximum Z_e' PPI map at 1.3° elevation for 1500-1800 MDT 15 August 1983 144

7.3b Predicted hail occurrences at 1.3° elevation for 1500-1800 MDT 15 August 1983 145

Figure Page

7.3c Surface observations of precipitation for 15 August 1983 compared to outlines of rain regions and hail regions predicted by a combination of Z_e' and $Z_{DR}^{e'}$ and by Z_e' 146

7.3d Contingency tables for the 15 August 1983 storm 147

7.4a Maximum Z_e' PPI map at 1.1° elevation for 1800-2000 MDT 5 July 1984 149

7.4b Predicted hail occurrences at 1.1° elevation for 1800-2000 MDT 5 July 1984 150

7.4c Surface observations of precipitation for 5 July 1984 compared to outlines of rain regions and hail regions predicted by a combination of Z_e' and $Z_{DR}^{e'}$ and by Z_e' 151

7.4d Contingency tables for the 5 July 1984 storm 152

LIST OF SYMBOLS

$a_{X,Y}$	maximum amplitudes of electric field in X,Y directions respectively
ALD	orientation angle of an assembly of particles
C	radar constant
CDR	circular depolarization ratio
CDR'	CDR corrected for propagation effects
dB	decibels
dBm	decibels of power with respect to 1 milliwatt
dBz	unit of the radar reflectivity factor in decibels with respect to 1 $\mathrm{mm}^6\mathrm{m}^{-3}$
E_n	electric field in n direction
E_X^t, E_Y^t	rectangular components of the transmitted field
E_R^t, E_L^t	circular components of the transmitted field
E_X^r, E_Y^r	rectangular components of the received field
E_R^r, E_L^r	circular components of the received field
f	frequency of monochromatic radiation
$\bar{f}$	frequency of quasi-monochromatic radiation
G	antenna gain
g_o, g_1, g_2, g_3	Stokes parameters
I	total intensity of electromagnetic wave
$\mathrm{Im}(\ldots)$	imaginary part of $(\ldots)$
$\mathbf{J}$	coherency matrix of partially polarized wave
$J_{XX}, J_{XY}, J_{YX}, J_{YY}$	elements of the coherency matrix
j	$\sqrt{-1}$
k_o	propagation constant of medium
k', k''	propagation constants of scatterers in horizontal and vertical directions respectively
k	$\frac{k'+k''}{2}$
LDR	linear depolarization ratio
LHC	left hand circular
M_1, M_2	wave amplitudes for transmission
$ORTT$	degree of orientation of an assembly of particles
$ORTT'$	$ORTT$ corrected for propagation effects
$\mathbf{P}$	propagation matrix

p	degree of polarization
R	rainfall rate (mm/hr)
R_1, R_2	wave amplitudes on reception
r	range
$\mathrm{Re}(\ldots)$	real part of $(\ldots)$
RHC	right hand circular
S	scattering target
S_{11}, S_{12}, S_{22}	elements of scattering matrix in rectangular coordinates
t	time
V	scatterer volume
W_1, W_2, W_3, W_4	radar observables at circular polarization
W	complex correlation between two orthogonal components of electric field at circular polarization, $W = W_3 + jW_4$
X	vertical direction
Y	horizontal direction
Y_o	admittance of free space
Z	direction of propagation
Z_{DR}	differential reflectivity
Z_{DR}^{c}	Z_{DR} derived from circular quantities
$Z_{DR}^{c'}$	Z_{DR}^{c} corrected for propagation effects
Z_e	equivalent radar reflectivity factor
Z_e'	Z_e corrected for propagation effects

Subscripts

$\pm$ or $\mp$	upper signs refer to right hand circular and lower signs refer to left hand circular radiation
c	circular polarization
cp	refer to completely polarized wave
l	linear polarization
i	refer to the i^{th} particle
1, 2	refer to orthogonal and main components respectively
X, Y	refer to X, Y directions respectively
X_1, X_2	refer to X_1, Y_1 directions respectively
X_2, Y_2	refer to X_2, Y_2 directions respectively

R, L	refer to right hand circular and left hand circular polarizations respectively
un	refer to unpolarized wave

Superscripts

$\pm$ or $\mp$	upper signs refer to right hand circular and lower signs refer to left hand circular radiation
r	received radiation
t	transmitted radiation
T	transpose matrix
$*$	complex conjugate

Greek letters

α	orientation angle of polarization ellipse; transverse angle of orientation
$\bar{\alpha}$	mean orientation angle of an assembly of particles
β	defined in Figure 1.4
γ	phase shift offset
ΔA	differential attenuation
$\Delta\varphi$	differential phase shift
$\delta_{\pm}$	scattering phase shift
$\bar{\delta}$	mean scattering phase shift
$\varepsilon_{1,2}$	polarizabilities of scatterer
ς	differential reflectivity
η	angle between symmetry axis of particle and direction of propagation
θ	phase shifter setting
λ	radar wavelength
ν	scattering term defined in equation (3.27)
ρ	degree of correlation between two orthogonal components of electric field
ρ_{α}	fraction of scatterers with orientation α
τ	rotation angle between XYZ and X_1Y_1Z coordinate systems

v	complex correlation between two orthogonal components of electric field
Φ	effective phase difference between two orthogonal components of electric field
$\phi_{X,Y}$	phase of electric field in X, Y directions respectively
ϕ	$\phi_Y - \phi_X$
φ	antenna phase pattern
ψ	angle expressing the axial ratio of the polarization ellipse

Abbreviation

ARC	Alberta Research Council
IF	intermediate frequency
MDT	mountain daylight time
NRCC	National Research Council of Canada
PPI	plan position indicator
PRF	pulse repetition frequency
RF	radio frequency
RHI	range height indicator
S-band	radio frequency in the 2-4 GHz band

CHAPTER I

Representation of Electromagnetic Wave Polarization

1.1 The Monochromatic Plane Wave

The parameters that completely describe an electromagnetic wave are the amplitude, frequency, phase, and *polarization.* A propagating electromagnetic wave can be modelled by three orthogonal vectors: the electric and magnetic field vectors, which are perpendicular to each other and to the Poynting field vector, which is in the direction of propagation of the wave. The direction of the electric field vector is used to define the polarization of the wave. Typically, this vector always lies in a plane; we thereby speak of *plane polarized radiation.*

For a plane wave propagating in the positive Z-direction in a Cartesian frame of reference, the electric field vector must lie in the XY-plane perpendicular to the Z-axis. At any point in space, the electric field vector is a function of time. As time progresses, the electric field vector generally moves periodically around an ellipse called the *polarization ellipse* and the wave is said to be *elliptically polarized.* When the electric field vector oscillates along a straight line, the wave is *linearly polarized*; when it traces a circle, the wave is said to be *circularly polarized.* In the case of circular and elliptical polarizations, the electric field vector may move either clockwise or counterclockwise. When looking along the direction of propagation, the wave is said to be *right-hand polarized* if the electric field vector rotates clockwise and *left-hand polarized* if counterclockwise. Figure 1.1 illustrates the three states of polarization (Humphries, 1974a).

The parameters that determine the orientation, shape, and size of the polarization ellipse are the amplitude, the orientation angle α, and the axial ratio of the ellipse n/m (see Figure 1.2) which can be expressed in terms of the angle ψ by (Beckman, 1968)

$$\tan\psi = \pm\frac{n}{m}, \tag{1.1}$$

with the signs distinguishing the two senses of rotation, + standing for left-hand polarization in our convention.

A general mathematical description of wave polarization can be written as

$$\begin{aligned} E_X &= a_X e^{j[2\pi ft-\phi_X]}, \\ E_Y &= a_Y e^{j[2\pi ft-\phi_Y]}, \end{aligned} \tag{1.2}$$

where t is time, f is the frequency, a_X and a_Y are the amplitudes, and ϕ_X and ϕ_Y are the phases.

Equation (1.2) is a general representation for an ellipse centered at the origin in the XY-plane. When $a_X = 0$ or $a_Y = 0$, the wave becomes linearly polarized along the Y or X direction respectively. When $a_X = a_Y$ and $\phi_Y - \phi_X = \pm\frac{\pi}{2}$, the wave is circularly polarized.

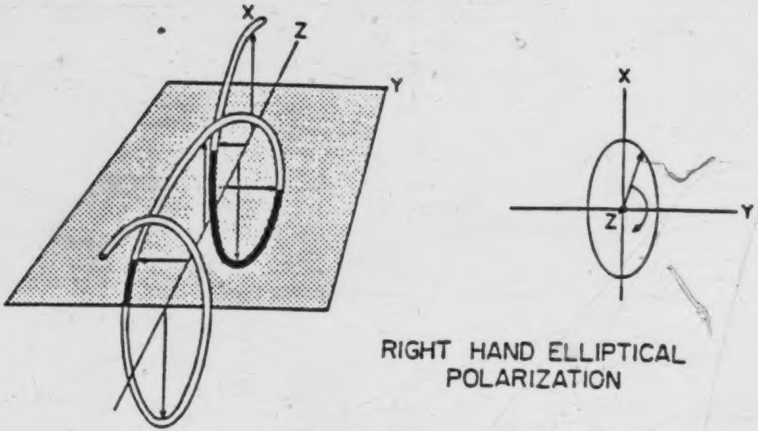

RIGHT HAND ELLIPTICAL POLARIZATION

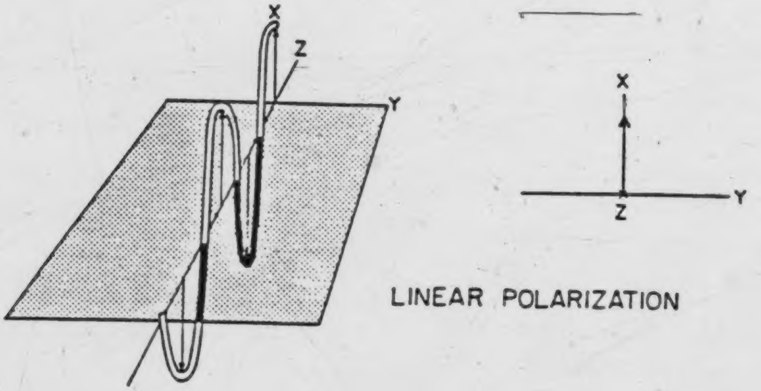

LINEAR POLARIZATION

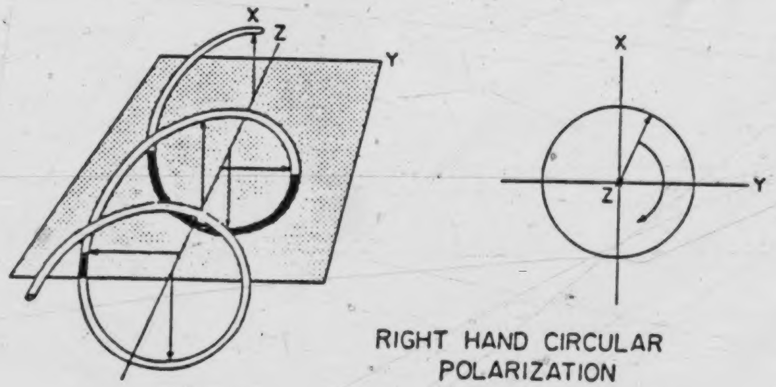

RIGHT HAND CIRCULAR POLARIZATION

Figure 1.1 Illustrations of elliptical, linear, and circular polarizations. The figures on the left represent the paths traced out by the electric field vectors as the waves propagate in the Z direction. The figures on the right represent the paths traced out by the electric field vectors at a fixed point in space.

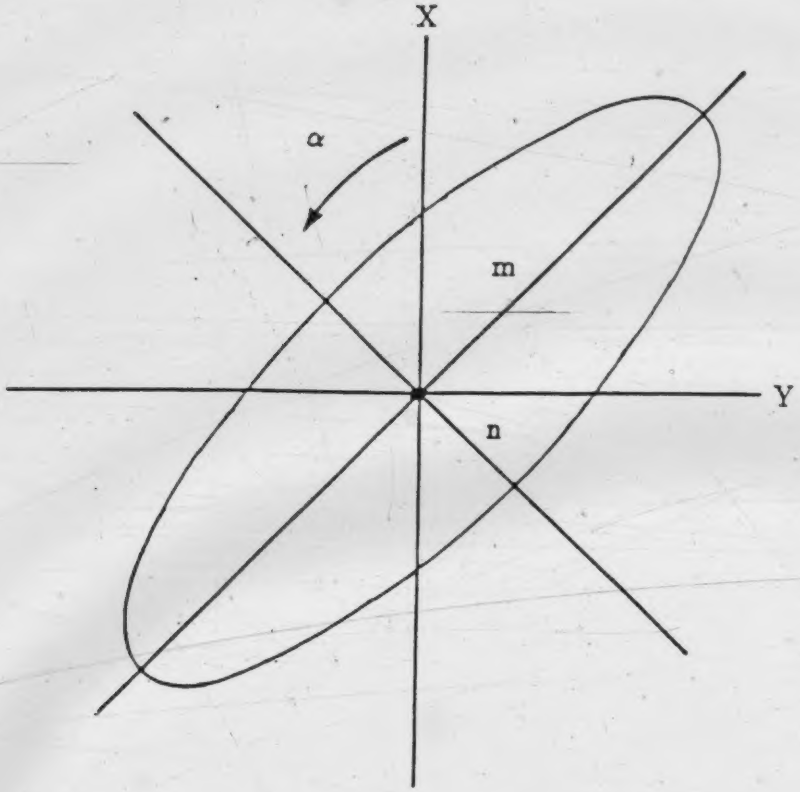

Figure 1.2 The polarization ellipse. α is the angle of the minor axis, n, with respect to the X axis. The propagation direction, Z, is into the page.

1.2 Stokes Parameters

In his studies of quasi-monochromatic radiation, Stokes (1901) introduced four quantities to characterize the amplitude and polarization of a wave. For strictly monochromatic waves, the Stokes parameters are defined by

$$\begin{aligned} g_0 &= |E_X|^2 + |E_Y|^2, \\ g_1 &= |E_X|^2 - |E_Y|^2, \\ g_2 &= 2|E_X||E_Y|\cos\phi, \\ g_3 &= 2|E_X||E_Y|\sin\phi. \end{aligned} \tag{1.3}$$

Substituting equations (1.2) into equations (1.3) yields

$$\begin{aligned} g_0 &= a_X^2 + a_Y^2, \\ g_1 &= a_X^2 - a_Y^2, \\ g_2 &= 2a_X a_Y \cos\phi, \\ g_3 &= 2a_X a_Y \sin\phi, \end{aligned} \tag{1.4}$$

where a_X and a_Y are the amplitudes and $\phi = \phi_Y - \phi_X$ is the phase difference of the two orthogonal field components.

The parameter g_0 is evidently proportional to the intensity of the wave and only three equations of (1.4) are independent, since it can easily be seen that

$$g_0^2 = g_1^2 + g_2^2 + g_3^2. \tag{1.5}$$

The Stokes parameters are related to the polarization angles α and ψ. In fact the following relations hold (see Mott, 1986)

$$\begin{aligned} g_1 &= g_0 \cos 2\psi \cos 2\alpha, \\ g_2 &= g_0 \cos 2\psi \sin 2\alpha, \\ g_3 &= g_0 \sin 2\psi. \end{aligned} \tag{1.6}$$

1.3 The Poincaré Sphere

The relations in (1.6) indicate a simple, geometrical representation of all the different states of polarization. The Stokes parameters g_1, g_2, and g_3 may be regarded as the Cartesian coordinates of a point q on a sphere of radius g_0 such that 2α and 2ψ are the spherical coordinates of this point (see Figure 1.3). This sphere is called the *Poincaré sphere.*

Every state of polarization corresponds to one point on the Poincaré sphere and vice versa:

- Elliptical polarization: For left-hand elliptical (LHE) polarization, $0 < \phi < \pi$, and from equations (1.3), it can be seen that $g_3 > 0$. Thus LHE polarization is represented by points on the sphere which lie above the equatorial plane (XY-plane). For RHE polarization, $\pi < \phi < 2\pi$ and $g_3 < 0$. This indicates that RHE polarization points lie below the equatorial plane.

- Circular polarization: For LHC and RHC polarizations, $|E_X| = |E_Y|$ and $\phi = \frac{\pi}{2}, -\frac{\pi}{2}$, respectively. It follows from equations (1.3) that $g_1 = g_2 = 0$, $g_3 = +g_0$ for LHC polarization, and $g_3 = -g_0$ for RHC polarization. This indicates that the north and south poles of the Poincaré sphere represent LHC and RHC polarization, respectively.

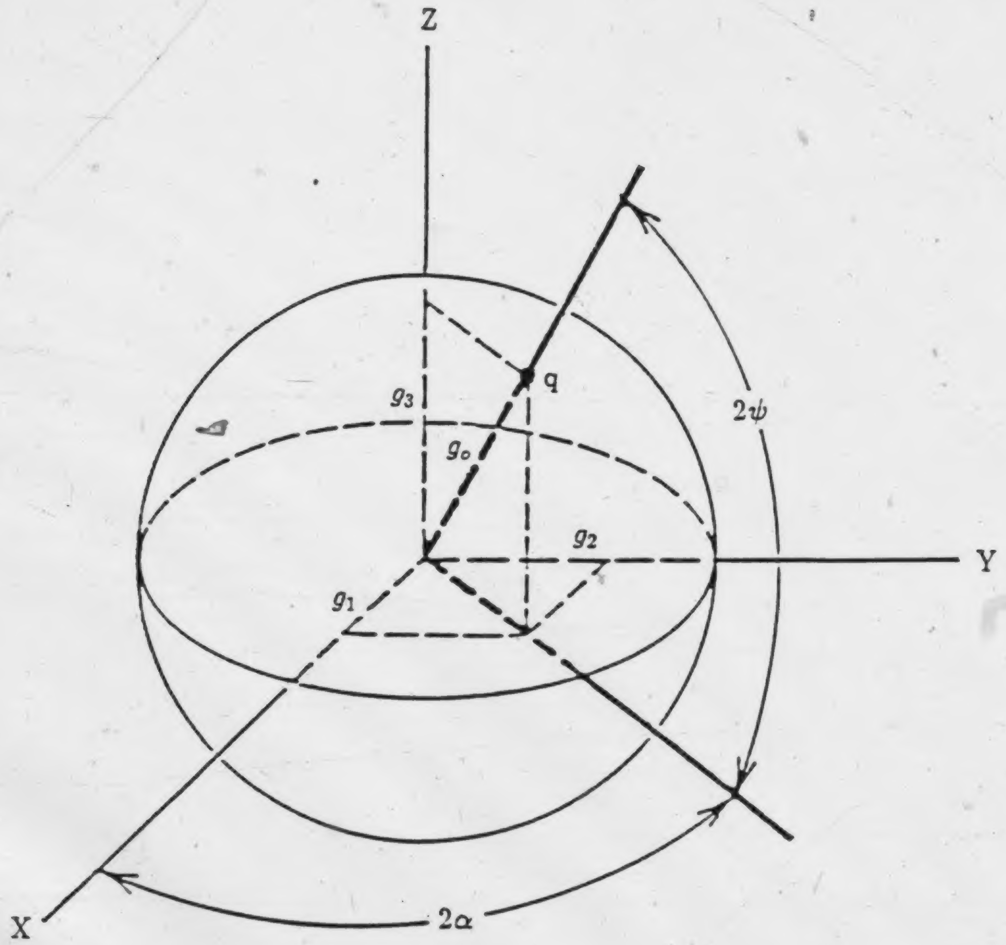
Z
Y
X
q
g_3
g_o
g_2
g_1
2ψ
2α

Figure 1.3 The Poincaré sphere (see text for explanation).

- Linear polarization: If $|E_X|$ and $|E_Y|$ are non-zero, then $\phi = 0, \pi$. Equations (1.3) give $g_3 = 0$, which suggests that linear polarization is represented by points on the equatorial plane. The intersection of the positive X-axis with the sphere corresponds to vertical linear polarization and the intersection of the negative X-axis represents horizontal linear polarization.

1.4 The Quasi-Monochromatic Plane Wave

So far, only a monochromatic wave has been considered. Such a wave is always completely polarized, meaning that the electric field vector traces an ellipse of constant eccentricity and orientation angle. The radiation arising from physical sources or backscattered from targets is never completely polarized and the electric field vector traces an ellipse whose shape and orientation change with time. Such a wave is called *partially polarized or quasi-monochromatic.* If the electric field vector moves extremely irregularly, the wave is said to be *randomly polarized* or *unpolarized.* At this point, it should be noted that the term *depolarization* refers to a change in the polarization state of a wave due to propagation through a medium, scattering from targets, or any other interaction with matter. The wave still remains polarized. Thus the terms *depolarized* and *unpolarized* refer to two different interaction mechanisms.

The field components of a quasi-monochromatic wave at a particular point in space can be represented as

$$\begin{aligned} E_X(t) &= a_X(t) e^{j[2\pi f t - \phi_X(t)]}, \\ E_Y(t) &= a_Y(t) e^{j[2\pi f t - \phi_Y(t)]}, \end{aligned} \tag{1.7}$$

where t is time, $\bar{f}$ is the mean frequency, $a_X(t)$ and $a_Y(t)$ are the amplitudes, and $\phi_X(t)$ and $\phi_Y(t)$ are the phases. The amplitudes and phases are assumed to be slowly varying time functions, i.e., the changes in the amplitudes and phases are relatively small during an interval of time equal to the inverse of the spectral band width Δf.

1.5 The Coherency Matrix

The polarization properties of a partially polarized wave can be determined by using the coherency matrix introduced by Born and Wolf (1964)

$$\mathbf{J} = \begin{pmatrix} J_{XX} & J_{XY} \\ J_{YX} & J_{YY} \end{pmatrix} = \begin{pmatrix} < E_X E_X^* > & < E_X E_Y^* > \\ < E_Y E_X^* > & < E_Y E_Y^* > \end{pmatrix}, \tag{1.8}$$

where the asterisks denote the complex conjugate and $< \ldots >$ denotes an average operator which is needed when the amplitudes or phases of the field components are functions of time

$$< \ldots >= \lim_{T \to \infty} \frac{1}{T} \int_0^T \ldots dt. \tag{1.9}$$

The diagonal elements J_{XX} and J_{YY} of the coherency matrix $\mathbf{J}$ defined by equation (1.8) are real and represent the intensities of the X and Y components of the wave. The off-diagonal elements J_{XY} and J_{YX} define the correlation between the two components of the wave. These elements are complex conjugates of each other. To identify the degree of correlation, Born and Wolf (1964), Ko (1962), and Kraus and Carver (1973) introduced the normalized correlation function. It is defined as follows:

$$\begin{aligned} v &= \rho e^{j\Phi} \\ &= \frac{J_{XY}}{\sqrt{J_{XX}J_{YY}}} \\ &= \frac{< E_X E_Y^* >}{\sqrt{< E_X E_X^* >< E_Y E_Y^* >}}, \end{aligned} \tag{1.10}$$

where $\rho = |v|$ is a measure of the degree of correlation between the X and Y components of the wave and Φ is the effective phase difference between them. The limiting cases of unpolarized and completely polarized waves correspond to $\rho = 0$ and 1 respectively.

The general form of the Stokes parameters of a quasi-monochromatic wave is defined as

$$\begin{aligned} g_0 &=< |E_X|^2 > + < |E_Y|^2 >, \\ g_1 &=< |E_X|^2 > - < |E_Y|^2 >, \\ g_2 &= 2 < |E_X||E_Y| \cos\phi >, \\ g_3 &= 2 < |E_X||E_Y| \sin\phi > . \end{aligned} \tag{1.11}$$

For time-independent amplitude and phase of the wave components, i.e., a monochromatic wave, equations (1.11) reduce to the monochromatic Stokes parameters defined by equations (1.3).

By comparing the Stokes parameters to the elements of the coherency matrix defined by equation (1.8), we see that

$$\begin{aligned} g_0 &= J_{XX} + J_{YY}, \\ g_1 &= J_{XX} - J_{YY}, \\ g_2 &= J_{XY} + J_{YX}, \\ g_3 &= -j(J_{XY} - J_{YX}), \end{aligned} \tag{1.12}$$

or, solving for the coherency matrix elements

$$\begin{aligned} J_{XX} &= \tfrac{1}{2}(g_0 + g_1), \\ J_{YY} &= \tfrac{1}{2}(g_0 - g_1), \\ J_{XY} &= \tfrac{1}{2}(g_2 + jg_3), \\ J_{YX} &= \tfrac{1}{2}(g_2 - jg_3). \end{aligned} \tag{1.13}$$

Written in matrix form, equations (1.13) read

$$\mathbf{J} = \frac{1}{2}\begin{pmatrix} g_o + g_1 & g_2 + jg_3 \\ g_2 - jg_3 & g_o - g_1 \end{pmatrix}. \tag{1.14}$$

The degree of polarization p, defined as the ratio of the intensity of the polarized portion to the total intensity of a wave, is given by

$$p = \sqrt{1 - \frac{4\det[\mathbf{J}]}{(\mathrm{Tr}[\mathbf{J}])^2}}, \tag{1.15}$$

where the trace and determinant of **J** are given by

$$\mathrm{Tr}[\mathbf{J}] = J_{XX} + J_{YY}, \tag{1.16}$$

$$\det[\mathbf{J}] = J_{XX}J_{YY} - J_{XY}J_{YX}. \tag{1.17}$$

The degree of polarization p varies from zero for an unpolarized wave to unity for a completely polarized wave and assumes fractional values for a partially polarized wave.

Combining equations (1.13) and (1.15), p can be represented by Stokes parameters as

$$p = \sqrt{\frac{g_1^2 + g_2^2 + g_3^2}{g_0^2}}. \tag{1.18}$$

For a given value of the total intensity I of a wave (for example unity, i.e., $g_0 = 1$), p represents the radius of the Poincaré sphere. In other words, the polarization state of a quasi-monochromatic wave is represented by a point whose polar coordinates are p, 2α, and 2ψ (or 2β), as shown in Figure 1.4.

The coherency matrix of a partially polarized wave of intensity I, degree of polarization p, and polarization angles α and ψ can be obtained by constructing two independent components, a completely polarized component and an unpolarized component (Born and Wolf, 1964), such that

$$\mathbf{J} = \mathbf{J}_{cp} + \mathbf{J}_{un}, \tag{1.19}$$

where $\mathbf{J}$ is the coherency matrix of the total wave, and $\mathbf{J}_{un}$ and $\mathbf{J}_{cp}$ are the coherency matrices of its unpolarized and completely polarized components respectively.

In general, the coherency matrix of a completely polarized monochromatic or quasi-monochromatic wave can be obtained by substituting the Stokes parameters of equations (1.6) into equation (1.14). This gives the following coherency matrix

$$\mathbf{J}_{cp} = \frac{I}{2}\begin{pmatrix} 1 + \cos 2\alpha \cos 2\psi & \sin 2\alpha \cos 2\psi + j \sin 2\psi \\ \sin 2\alpha \cos 2\psi - j \sin 2\psi & 1 - \cos 2\alpha \cos 2\psi \end{pmatrix}. \tag{1.20}$$

From Figure 1.4, $2\beta = \frac{\pi}{2} - 2\psi$. Substituting in equation (1.20) yields

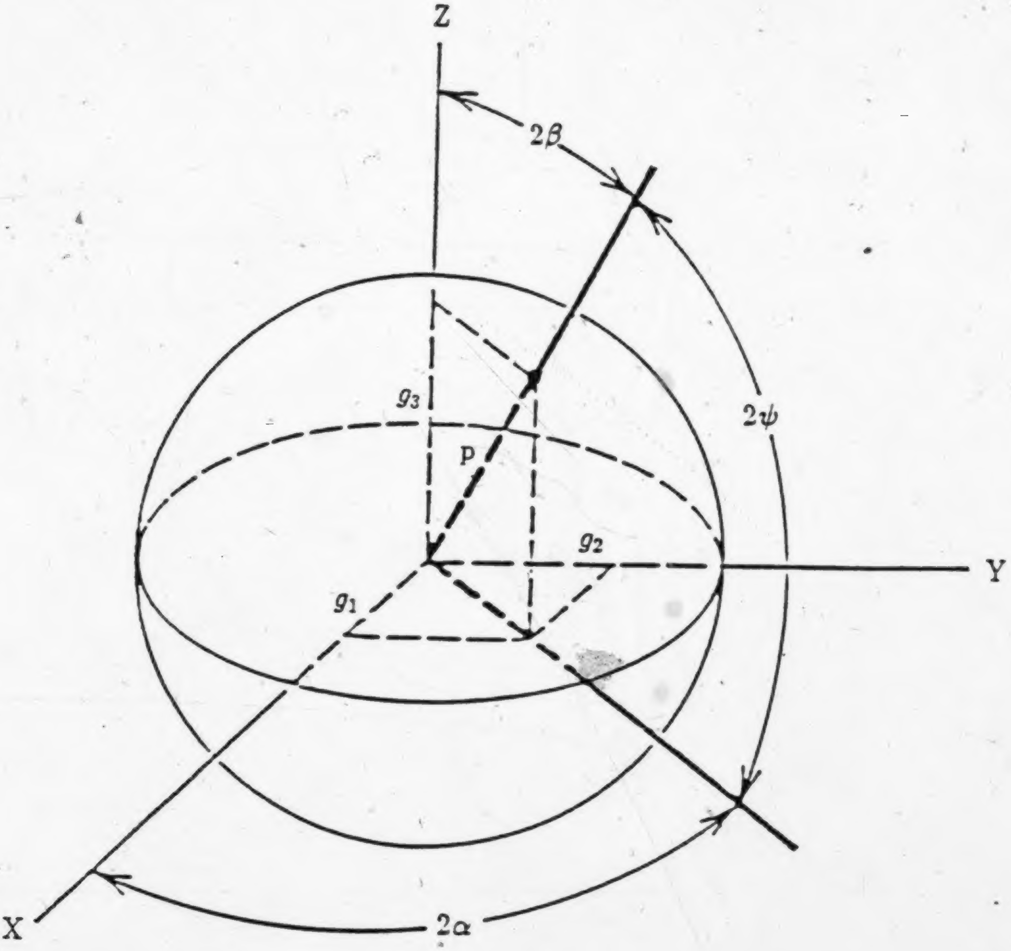
Z
2β
2ψ
g_3
P
g_2
Y
g_1
X
2α

Figure 1.4 The Poincaré sphere showing Stokes parameters normalized to $g_o = 1$. The radius of the polarization vector, p, is the degree of polarization.

$$\mathbf{J}_{cp} = \frac{I}{2}\begin{pmatrix} 1+\cos 2\alpha \sin 2\beta & \sin 2\alpha \sin 2\beta + j\cos 2\beta \\ \sin 2\alpha \sin 2\beta - j\cos 2\beta & 1-\cos 2\alpha \sin 2\beta \end{pmatrix}. \qquad (1.21)$$

For the unpolarized wave, $J_{XX} = J_{YY} = \frac{\mathrm{Tr}[\mathbf{J}]}{2}$ and $J_{XY} = J_{YX} = 0$. From equation (1.8), it follows that

$$\mathbf{J}_{un} = \frac{I}{2}\begin{pmatrix} 1 & 0 \\ 0 & 1 \end{pmatrix}. \qquad (1.22)$$

Multiplying equation (1.21) by p and equation (1.22) by $(1-p)$ and adding the results gives

$$\mathbf{J} = \frac{I}{2}\begin{pmatrix} 1+p\cos 2\alpha \sin 2\beta & p(\sin 2\alpha \sin 2\beta + j\cos 2\beta) \\ p(\sin 2\alpha \sin 2\beta - j\cos 2\beta) & 1-p\cos 2\alpha \sin 2\beta \end{pmatrix}. \qquad (1.23)$$

which is the Cartesian coherency matrix of partially polarized radiation of intensity I, degree of polarization p, and polarization angles α and β. This equation will be used in Chapter V to develop the corresponding circular coherency matrix.

1.6 Polarization Techniques in Radar Meteorology

Conventional weather radars usually employ horizontal and vertical polarization. Generally speaking, antennas which transmit horizontally polarized radiation are set to receive only the horizontally polarized component of the returning signal and vertically set antennas transmit and receive vertically polarized radiation. This means that without special design and construction, weather radars are incapable of receiving the component orthogonal to that which is transmitted. Polarization diversity radars are designed to transmit any arbitrarily chosen polarization and measure the power returned in the orthogonal component as well as in the component with the same sense of polarization as the transmitted component. This class of radars is also usually capable of measuring the time averaged correlation and phase between the two orthogonal components, and hence provides four information signals (instead of one for a conventional radar). In meteorology, polarization diversity radars have been used to study severe storms and hail storms in particular. Such studies have practical applications in severe storm forecasting, weather modification, and agricultural meteorology.

Consider a radar which transmits radiation with a known polarization state and suppose that the radiation is backscattered by a region of precipitation. The backscattered wave will, in general, be elliptically polarized and will be completely described by the backscattered ellipse. The polarization properties of the backscattered ellipse can be determined by resolving it into a main and an orthogonal component.

For linearly polarized radar, the backscattered ellipse is resolved into horizontal and vertical components. The main component lies in the same plane as the transmitted radiation, and the orthogonal is perpendicular to this plane. In the case of circularly polarized radar, the backscattered ellipse is resolved into RHC and LHC components. The main component has a sense of rotation opposite to that of the transmitted radiation, and the orthogonal component has the same sense of rotation as the transmitted radiation.

The ratio of the orthogonal component to the main component is called the *linear depolarization ratio* (LDR) for linearly polarized radar and *circular depolarization ratio* (CDR) for circularly polarized radar. LDR and CDR are related to the shape of the backscattered ellipse.

In an extension to the coherency matrix defined by equation (1.8), the elements are considered to be composed of any two mutually orthogonal electric fields, for example RHC and LHC polarizations. Therefore, for circularly polarized radar, the coherency matrix of the backscattered radiation and the complex correlation will be written as (McCormick, 1968)

$$\mathbf{J}' = \begin{pmatrix} W_1 & W_3 + jW_4 \\ W_3 - jW_4 & W_2 \end{pmatrix}, \tag{1.24}$$

$$\begin{aligned} v_c &= \rho_c e^{j\Phi_c} \\ &= \frac{W_3 + jW_4}{\sqrt{W_1 W_2}}. \end{aligned} \tag{1.25}$$

The elements of the coherency matrix W_1 , W_2 , W_3, and W_4 will be called the *observables.* ρ_c and Φ_c are the degree of correlation and the phase difference between the two orthogonal components. In Chapters III and V we shall relate these observables to the properties of precipitation and to the polarization properties of the backscattered radiation (I, p, and β).

CHAPTER II

A Review of Polarization Studies Related to Radar Meteorology

2.1 Historical Overview

Studies relating the polarization properties of backscattered echoes to specific types of precipitation date back to the invention of radar. During the 1950's, theoretical studies suggested the possibility of distinguishing between spherical and nonspherical precipitation particles using radar. The basis of these studies was Gans' extension of Rayleigh's scattering theory to ellipsoids (Gans, 1912). Among these early works are those of Kerker and Hitschfeld (1950), Labrum (1952), Atlas *et al.* (1953), and Stevenson (1953). Later works reported by Shupiatskii (1959) and Gershenzon and Shupiatskii (1961) gave additional theoretical consideration to the depolarization caused by small ellipsoids. These two later works related depolarization to the axial ratio of the scatterers for various combinations of transmitted and received polarizations.

Experimental procedures for verifying these theoretical results were reported by Newell *et al.* (1955), Marshall and Gordon (1957), and Shupiatskii and Morgunov (1963). Early polarization observations of precipitation were presented by Browne and Robinson (1952), Hunter (1954), Wexler (1955), and Newell *et al.* (1955). These researchers employed linearly and circularly polarized antennas to observe LDRs and cancellation ratios [1] of the backscatter radiation from rain, snow, and the melting layer. Gent *et al.* (1963) reported on depolarization characteristics caused by aircraft, precipitation, and terrain. Morgunov and Shupiatskii (1964) made polarization observations during experiments into hail suppression by cloud seeding. They suggested that their data proved progressive glaciation due to seeding, because at the top of the seeded clouds the cancellation ratio increased from about -17 dB before seeding to -10 dB afterwards. Newell *et al.* (1957) and Peter (1966) presented polarization observations of thunderstorms which produced hail. Their results were contradictory, suggesting that radar measurements of LDR or CDR alone were not sufficient to differentiate between hail and rain.

In a recent paper, Seliga *et al.* (1987) gave an excellent, comprehensive review of the early developments of polarization techniques in radar meteorology. They traced major early developments in polarization research in the United States, Canada, and the Soviet Union.

2.2 Polarization Diversity Radar Studies

In the late 1960's, two polarization diversity radar systems for the purpose of meteorological observations were designed and built by G. C. McCormick and his associates at the National Research Council of Canada (NRCC). Both included a polarization diversity system comprised of a dual-polarization antenna and a dual-channel receiving unit. The two systems provided: 1) transmission of any polarization state, 2) simultaneous reception of the main and the orthogonal components of the backscattered radiation, and 3) measurements of the correlation between the two received signals and their relative phase. One of the radars was originally operated at 16.5 GHz but in 1981 it was replaced with a new radar operating at 9.6 GHz. It was used initially by the NRCC in Ottawa to study precipitation effects on propagation of microwave communication. The other radar operated at 2.88 GHz and was designed for the Alberta Hail Project. Both systems used the circular mode of transmission in most studies.

---

[1] The cancellation ratio is the ratio of the power of the orthogonal backscattered component when circular polarization is transmitted to that of the main backscattered component when linear polarization is transmitted.

The first observations using the NRCC system were reported by McCormick and Hendry (1970), Hendry and McCormick (1971), and McCormick and Hendry (1972). Their results showed that for rain, the circular depolarization ratio CDR tended to increase as reflectivity increased and correlation [2] assumed high values. Their observations of the relative phase angle seemed to confirm that large raindrops tend to fall with their minor axes oriented vertical. McCormick and Hendry (1975, 1979) developed the basic principles and techniques for radar determination of the polarization properties of precipitation. Hendry *et al.* (1976) reported on polarization observations of different types of precipitation. Their results showed that high correlation is a characteristic of moderate or heavy rain. Low correlation implies the presence of ice-phase hydrometeors. Hendry and Antar (1984a) presented observations of various types of precipitation made with circular polarization at 16.5 GHz and 9.6 GHz. They reported the extent to which simultaneous measurements of reflectivity, CDR, and correlation can be used to distinguish among various precipitation types. Hendry *et al.* (1986) described an experimental technique in which measurements were made sequentially at circular and linear polarizations to determine the relationship between the degree of preferred orientation of precipitation particles and the characteristics of the polarization radar echo. They concluded that both orientation and shape effects were significant in remote sensing of precipitation type with polarization diversity radar. In a recent paper, Antar and Hendry (1987) showed that correlation detection techniques used with circular polarization are applicable to the linear polarization case. They suggested that, in addition to circular polarization data, measurements at linear polarization can enhance the utility of correlation measurements in precipitation identification.

---

[2] Hereafter the term correlation refers to the correlation between the two orthogonal components of the received signal which is related to the fraction of oriented scatterers in the target volume.

The first major presentation using the Alberta radar was by Barge (1972). He correlated several hundred CDR measurements with reflectivity from echo regions below which (within 2 km) ground observations allowed him to judge whether the fallout was hail or rain. He also presented measurements of the relative phase angle and described their value in the detection of hail. Barge's work suggested that circular polarization radar could be used to detect hail. Humphries and Barge (1979) reported on the polarization and dual-wavelength radar observations of the bright band, a phenomenon related to partial and complete melting of snowflakes as they fall below the freezing level. Their results indicated that the combination of both polarization and dual-wavelength techniques was more powerful for the determination of the type and size of hydrometeors than either technique used alone. Barge and Humphries (1980) found that four polarization parameters could be used not only to detect hail but to assess whether rain was contributing significantly to the total precipitation. A theoretical model of rain and wet hail was developed by Torlaschi *et al.* (1984). It computes reflectivity, CDR, and correlation for various combinations of rainfall and hailfall. The calculations when applied to hail implied that measurements of reflectivity and correlation could determine the relative contribution of rain and hail to the total precipitation.

2.3 Differential Reflectivity Radar Studies

A differential reflectivity radar was developed by Seliga and Bringi (1976) wherein the transmitted pulses were switched rapidly and sequentially between horizontal and vertical polarizations. The reception was co-polar, yielding reflectivity factors for horizontal and vertical polarization from which the differential reflectivity (Z_{DR}) was derived. This technique has been used by Bringi *et al.* (1983), Aydin *et al.* (1984, 1986), and at the Rutherford Appleton Laboratory in the United Kingdom (Hall *et al.*, 1980; Goddard and Cherry, 1984).

Evidence of hail detection using this differential reflectivity radar was provided by Bringi *et al.* (1984). Using observations of two hailstorms, they reported that although reflectivity could be high for both rain and hail, Z_{DR} in hail regions was close to 0 dB while for rain regions Z_{DR} was greater than 1 dB. They suggested that the difference in Z_{DR} signals resulted from oblate raindrops falling mostly with their minor axes vertical, whereas hail particles are generally non-spherical and often tumble. Illingworth *et al.* (1986) presented observations of an intense convective storm and suggested that the occurrence of low Z_{DR} near the ground where reflectivity was high appeared to be a reliable signature of hail.

McCormick (1979) demonstrated that a relationship exists between differential reflectivity and circular polarization measurements. This relationship was supported by model calculations (Holt, 1984) and verified by measurements carried out with linear and circular polarizations (Hendry *et al.*, 1986). Based on the assumption that raindrops are aligned with their minor axes vertical, Metcalf (1980) and Seliga *et al.* (1984) developed relationships specifically linking Z_{DR} and CDR.

2.4 Investigations of Propagation Effects

Propagation through a precipitation medium comprised of non-spherical particles with a preferred alignment might alter the polarization state of the transmitted signal to the extent that the polarization properties of the received signal are dominated by the intervening medium rather than the properties of the scatterers in the target volume. This problem was first approached by the microwave communications people who viewed precipitation as an attenuating medium. Oguchi (1960) developed formulas for computing forward scattering by raindrops and calculated the differential attenuation and differential phase shift as a function of rainfall rate. Oguchi (1964, 1966) calculated the forward and backward scattering amplitudes for non-spherical raindrops which were not small compared to the wavelength. Similar calculations were performed by Watson and Arbabi (1973) and by Morrison *et al.* (1973). Observations of such propagation effects were reported by McCormick *et al.* (1972) and Semplak (1974).

The effects of propagation through precipitation on the Alberta circularly polarized radar operating at 2.88 GHz were investigated by Humphries (1974a, 1974b). Using the scattering theory of Van de Hulst (1957), he calculated the differential attenuation and the differential phase shift caused by the Marshall-Palmer (1948) size distribution of raindrops with shapes according to Pruppacher and Pitter (1971). He found the differential attenuation to be negligible but the differential phase shift to be significant. Humphries also found evidence for these propagation effects in radar observations of heavy rain and demonstrated that these effects would influence measured values of CDR, correlation, and phase angle, making them larger than the intrinsic values for scattering alone.

Seliga *et al.* (1984) examined the relative sensitivity of CDR and Z_{DR} measurements in the S-band to propagation effects. They found that CDR can be seriously affected by propagation through rainfall, but Z_{DR} is generally unaffected because Z_{DR} depends only on differential attenuation, which is very small in the S-band frequencies. In a recent paper, McGuinness *et al.* (1987) modelled effects of S-band propagation through precipitation for both linearly and circularly polarized radars. They reported that in the S-band, linearly polarized radar does not suffer significant propagation effects except when sensing through heavy rain over long paths, while circularly polarized radar suffers from propagation effects at lighter rainfall rates.

Bebbington *et al.* (1987) developed a procedure for correcting for propagation effects in S-band. By assuming that in the S-band any deviation from zero in the phase angle between the two orthogonal components of the received signal can be attributed to the differential phase shift, they showed that the phase angle can be used to remove effects of propagation on the other parameters. Another approach for removing propagation effects on circular polarization measurements was proposed by Jameson and Davé (1988). This method involves re-expressing the circular polarization quantities in terms of the linear polarization parameters which are unaffected by propagation and then re-computing the circular polarization quantities from these linear polarization estimates. The techniques will be discussed in detail in Chapter V.

CHAPTER III

Principles of Polarization Diversity Radar

3.1 Introduction

This chapter covers the principles involved in the use of radar to determine the polarization properties of precipitation. The radar observables introduced in Chapter I will be related to 1) the effects of propagation on a wave travelling between the radar and the scattering target and 2) the influence of the scattering process by the target. These effects will be considered separately and then combined to see how the radar observables are affected by propagation and scattering. Relationships will be obtained in terms of RHC and LHC polarizations. Much of the material presented in this chapter was developed by Barge (1972), Humphries (1974a), McCormick and Hendry (1975, 1976), and Holt (1984).

3.2 Network Representation

Figure 3.1 shows a schematic of the network from the scattering target to the receivers (McCormick and Hendry, 1975). The radar system considered is an ideal polarization diversity radar equipped with a two-channel antenna which provides transmission of any selected polarization and reception of the transmitted polarization and that orthogonal to it. Four information signals are thereby obtained:

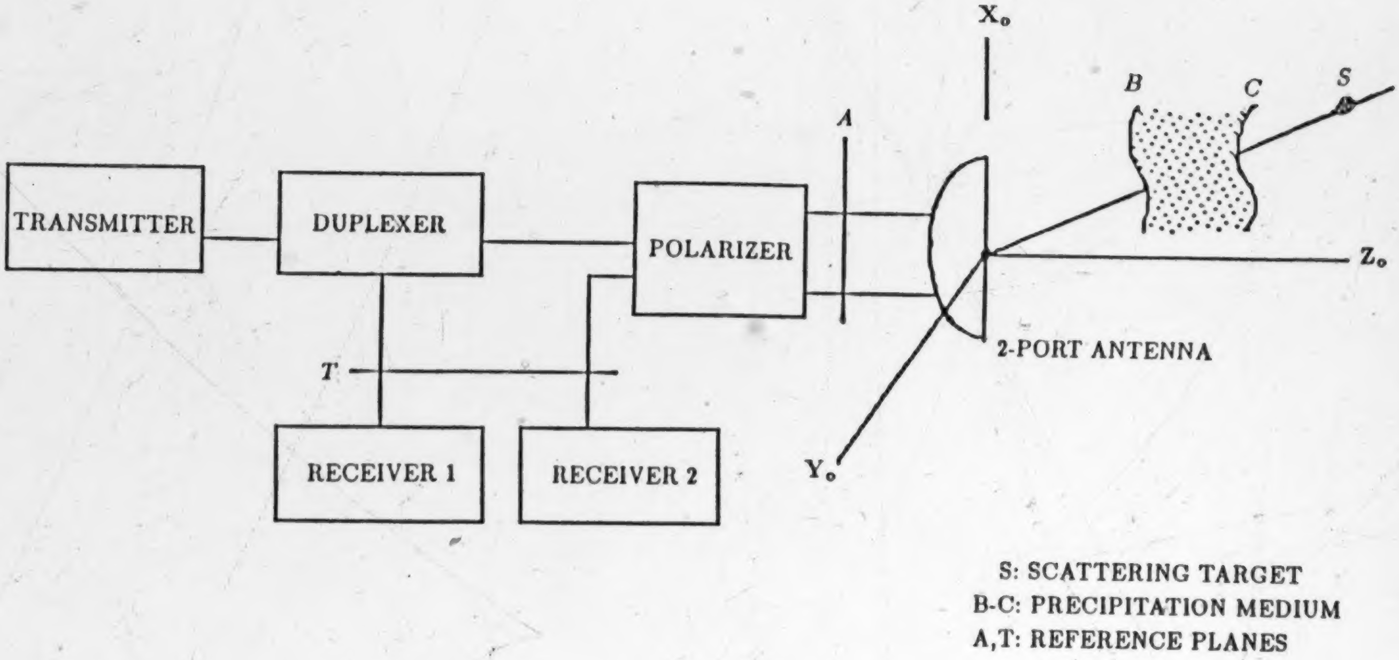
X₀
B
C
S
A
TRANSMITTER
DUPLEXER
POLARIZER
Z₀
2-PORT ANTENNA
T
RECEIVER 1
RECEIVER 2
Y₀
S: SCATTERING TARGET
B-C: PRECIPITATION MEDIUM
A,T: REFERENCE PLANES

Figure 3.1 Schematic representation of the network from the scattering target to the radar receivers.

namely the powers of the two orthogonal components and the correlation and phase angle between them. A detailed description of the Alberta Research Council's polarization diversity radar system will be given in the next chapter.

Consider radar transmitting elliptically polarized radiation and that the radiation is intercepted by a scattering target located at a distance r from the radar referenced to the basic XYZ coordinate system. In this coordinate system, the Z-axis is along the direction of propagation from the radar towards the target, the Y-axis is along the horizontal direction, and the X-axis is orthogonal to the Z- and Y-axes. The radar echo will in general be elliptically polarized. Any elliptically polarized wave can be treated as a superposition of two linear or circular orthogonal components

$$\vec{E} = E_X \hat{X} + E_Y \hat{Y}, \tag{3.1}$$

or

$$\vec{E} = E_R \hat{R} + E_L \hat{L}, \tag{3.2}$$

where $\hat{X}$ and $\hat{Y}$ are unit vectors along the X and Y directions and $\hat{R}$ and $\hat{L}$ are unit vectors representing RHC and LHC polarizations.

As indicated by Crispin and Siegel (1968) (see also Azzam and Bashara, 1977), the relation between the unit vectors for circular and linear polarizations is given by

$$\begin{pmatrix} \hat{R} \\ \hat{L} \end{pmatrix} = \frac{1}{\sqrt{2}} \begin{pmatrix} 1 & -j \\ 1 & j \end{pmatrix} \begin{pmatrix} \hat{X} \\ \hat{Y} \end{pmatrix} = \mathbf{U} \begin{pmatrix} \hat{X} \\ \hat{Y} \end{pmatrix}, \tag{3.3}$$

where $j = \sqrt{-1}$. The transmitted field components are related by

$$\begin{pmatrix} E_R^t \\ E_L^t \end{pmatrix} = \frac{1}{\sqrt{2}} \begin{pmatrix} 1 & j \\ 1 & -j \end{pmatrix} \begin{pmatrix} E_X^t \\ E_Y^t \end{pmatrix} = \mathbf{U}^* \begin{pmatrix} E_X^t \\ E_Y^t \end{pmatrix}, \qquad (3.4)$$

or

$$\begin{pmatrix} E_X^t \\ E_Y^t \end{pmatrix} = \frac{1}{\sqrt{2}} \begin{pmatrix} 1 & 1 \\ -j & j \end{pmatrix} \begin{pmatrix} E_R^t \\ E_L^t \end{pmatrix} = \mathbf{U}^T \begin{pmatrix} E_R^t \\ E_L^t \end{pmatrix}, \qquad (3.5)$$

where the asterisk denotes the complex conjugate and the T denotes the transpose. The superscript t, for transmitted, indicates propagation away from the radar.

For the backscattered field components, $\mathbf{U}^*$ and $\mathbf{U}^{\mathrm{T}}$ are replaced by their complex conjugates so that

$$\begin{pmatrix} E_R^r \\ E_L^r \end{pmatrix} = \frac{1}{\sqrt{2}} \begin{pmatrix} 1 & -j \\ 1 & j \end{pmatrix} \begin{pmatrix} E_X^r \\ E_Y^r \end{pmatrix} = \mathbf{U} \begin{pmatrix} E_X^r \\ E_Y^r \end{pmatrix}, \qquad (3.6)$$

or

$$\begin{pmatrix} E_X^r \\ E_Y^r \end{pmatrix} = \frac{1}{\sqrt{2}} \begin{pmatrix} 1 & 1 \\ j & -j \end{pmatrix} \begin{pmatrix} E_R^r \\ E_L^r \end{pmatrix} = \mathbf{U}^{T*} \begin{pmatrix} E_R^r \\ E_L^r \end{pmatrix}, \qquad (3.7)$$

where the superscript r, for backscattered, indicates propagation towards the radar.

3.3 Propagation between the Radar and the Scattering Target

Assume that a precipitation medium exists between the radar and the scattering target (the layer between B and C in Figure 3.1) and that this medium consists of non-spherical particles with a preferred orientation. Such a medium will have vertical and horizontal anisotropy axes X_1 and Y_1, and this new X_1Y_1Z coordinate system will be inclined at an angle τ to the basic coordinate system XYZ (see Figure 3.2).

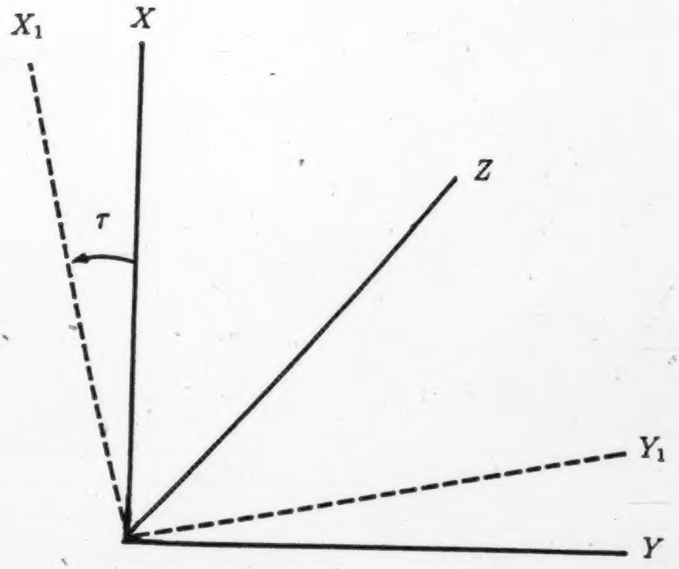

Figure 3.2 Relationship of symmetry axes of an anisotropic medium X_1Y_1Z and the basic coordinate system XYZ. Propagation is along the Z-axis.

For propagation from the radar to the target, the field components at the scattering target are related to the field components at the radar by (McCormick, 1975)

$$\begin{pmatrix} E^t_{X_1} \\ E^t_{Y_1} \end{pmatrix}_S = \frac{1}{r} \begin{pmatrix} e^{-jk'r} & 0 \\ 0 & e^{-jk''r} \end{pmatrix} \begin{pmatrix} E^t_{X_1} \\ E^t_{Y_1} \end{pmatrix}_{Z=0} , \tag{3.8}$$

where r is the distance between the radar and the target. The complex propagation constants k' and k'' are functions of the eccentricity and refractivity of the particles.

The field components in the X_1Y_1Z coordinate system are related to the field components in the basic XYZ coordinate system by

$$\begin{pmatrix} E_X \\ E_Y \end{pmatrix} = \begin{pmatrix} \cos\tau & \sin\tau \\ -\sin\tau & \cos\tau \end{pmatrix} \begin{pmatrix} E_{X_1} \\ E_{Y_1} \end{pmatrix} = \mathbf{R}_1 \begin{pmatrix} E_{X_1} \\ E_{Y_1} \end{pmatrix} , \tag{3.9}$$

or

$$\begin{pmatrix} E_{X_1} \\ E_{Y_1} \end{pmatrix} = \begin{pmatrix} \cos\tau & -\sin\tau \\ \sin\tau & \cos\tau \end{pmatrix} \begin{pmatrix} E_X \\ E_Y \end{pmatrix} = \mathbf{R}_1^T \begin{pmatrix} E_X \\ E_Y \end{pmatrix} . \tag{3.10}$$

Application of equations (3.9) and (3.10) to equation (3.8) leads to

$$\begin{pmatrix} E^t_X \\ E^t_Y \end{pmatrix}_S = \mathbf{R}_1 \frac{1}{r} \begin{pmatrix} e^{-jk'r} & 0 \\ 0 & e^{-jk''r} \end{pmatrix} \mathbf{R}_1^T \begin{pmatrix} E^t_X \\ E^t_Y \end{pmatrix}_{Z=0} . \tag{3.11}$$

From equations (3.4) , (3.5), and (3.11), it follows that the circular field components at the target are

$$\begin{pmatrix} E^t_R \\ E^t_L \end{pmatrix}_S = \mathbf{U}^* \mathbf{R}_1 \frac{1}{r} \begin{pmatrix} e^{-jk'r} & 0 \\ 0 & e^{-jk''r} \end{pmatrix} \mathbf{R}_1^T \mathbf{U}^T \begin{pmatrix} E^t_R \\ E^t_L \end{pmatrix}_{Z=0} . \tag{3.12}$$

Expanding this equation yields

$$\begin{pmatrix} E_R^t \\ E_L^t \end{pmatrix}_S = \frac{e^{-jkr}}{r}\mathbf{P}\begin{pmatrix} E_R^t \\ E_L^t \end{pmatrix}_{Z=0}, \tag{3.13}$$

where

$$k = \frac{k' + k''}{2}, \tag{3.14}$$

and the propagation matrix $\mathbf{P}$ is given by

$$\mathbf{P} = \frac{1}{\sqrt{1-(pe^{j\chi})^2}}\begin{pmatrix} 1 & pe^{j(\chi-2\tau)} \\ pe^{j(\chi+2\tau)} & 1 \end{pmatrix}, \tag{3.15}$$

where

$$pe^{j\chi} = \tanh\left[\frac{j(k''-k')r}{2}\right]. \tag{3.16}$$

By treating the propagation problem as forward scattering problem, Humphries (1974a) showed that the propagation term $pe^{j\chi}$ is related to the differential attenuation and the differential phase shift by

$$pe^{j\chi} = \tanh[(0.0575\Delta A + j\frac{\pi}{360}\Delta\phi)], \tag{3.17}$$

where ΔA is the differential attenuation (in dB) and $\Delta\phi$ is the phase differential shift (in degrees) between the linear horizontal and vertical components of a circularly polarized wave.

For a wave propagating from the target towards the radar, the angle τ must change sign. Therefore, the propagation matrix $\mathbf{P}$ of equation (3.13) must be replaced by its transpose $\mathbf{P}^T$ so that

$$\begin{pmatrix} E_R^r \\ E_L^r \end{pmatrix}_{Z=0} = \frac{e^{-jkr}}{r}\mathbf{P}^T\begin{pmatrix} E_R^r \\ E_L^r \end{pmatrix}_S. \tag{3.18}$$

3.4 Scattering by a Single Target

We now consider the influence of the scattering by the target. Assume that the scattering target is arbitrarily oriented and referenced to the X_2Y_2Z coordinate system and that this new coordinate system is inclined at an angle α (canting angle) to the basic coordinate system XYZ (see Figure 3.3a). The reference axis of the scatterer is related to the X_2Y_2Z coordinate system through an angle η and lies in the X_2Z plane (see Figure 3.3b).

The components of the incident and the backscattered fields are related by a scattering matrix which transforms the incident wave at the target into a backscattered wave towards the radar so that

$$\begin{pmatrix} E^r_{X_2} \\ E^r_{Y_2} \end{pmatrix}_S = \begin{pmatrix} S_{11} & S_{12} \\ S_{12} & S_{22} \end{pmatrix} \begin{pmatrix} E^t_{X_2} \\ E^t_{Y_2} \end{pmatrix}_S , \tag{3.19}$$

where S_{11}, S_{22}, and S_{12} are the elements of the scattering matrix. These elements depend upon the size, shape, and dielectric constant of the scattering target.

The components in the X_2Y_2Z and the XYZ coordinate systems are related by

$$\begin{pmatrix} E_X \\ E_Y \end{pmatrix} = \begin{pmatrix} \cos\alpha & \sin\alpha \\ -\sin\alpha & \cos\alpha \end{pmatrix} \begin{pmatrix} E_{X_2} \\ E_{Y_2} \end{pmatrix} = \mathbf{R}_2 \begin{pmatrix} E_{X_2} \\ E_{Y_2} \end{pmatrix} , \tag{3.20}$$

or

$$\begin{pmatrix} E_{X_2} \\ E_{Y_2} \end{pmatrix} = \begin{pmatrix} \cos\alpha & -\sin\alpha \\ \sin\alpha & \cos\alpha \end{pmatrix} \begin{pmatrix} E_X \\ E_Y \end{pmatrix} = \mathbf{R}_2^T \begin{pmatrix} E_X \\ E_Y \end{pmatrix} . \tag{3.21}$$

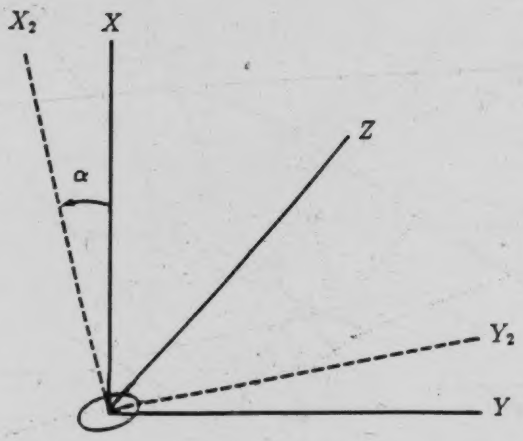
X_2
X
Z
α
Y_2
Y

Figure 3.3a Relationship between the coordinate system X_2Y_2Z attached to the scattering target and the basic coordinate system XYZ.

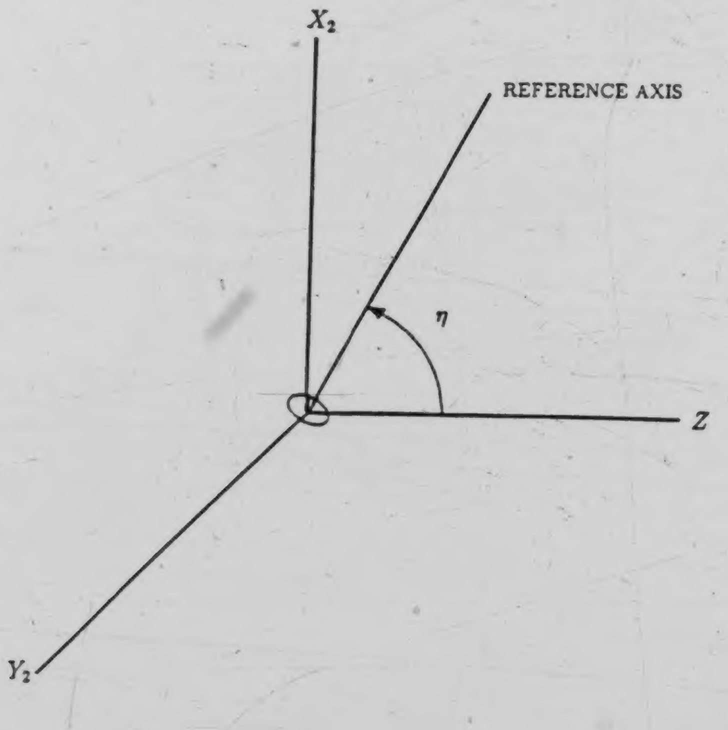
X_2
REFERENCE AXIS
η
Z
Y_2

Figure 3.3b Relationship between the reference axis of the scattering target and the X_2Y_2Z coordinate system. The reference axis lies in the X_2Z plane.

Therefore, the field components in the XYZ coordinate system are

$$\begin{pmatrix} E_X^r \\ E_Y^r \end{pmatrix}_s = \mathbf{R}_2 \begin{pmatrix} S_{11} & S_{12} \\ S_{12} & S_{22} \end{pmatrix} \mathbf{R}_2^T \begin{pmatrix} E_X^t \\ E_Y^t \end{pmatrix}_s . \tag{3.22}$$

The corresponding circular components are obtained by applying equations (3.5) and (3.6) to equation (3.22)

$$\begin{pmatrix} E_R^r \\ E_L^r \end{pmatrix}_s = \mathbf{U}\mathbf{R}_2 \begin{pmatrix} S_{11} & S_{12} \\ S_{12} & S_{22} \end{pmatrix} \mathbf{R}_2^T \mathbf{U}^T \begin{pmatrix} E_R^t \\ E_L^t \end{pmatrix}_s . \tag{3.23}$$

Expansion of this equation leads to

$$\begin{pmatrix} E_R^r \\ E_L^r \end{pmatrix}_s = \frac{S_{11} + S_{22}}{2} \begin{pmatrix} \nu^+ & 1 \\ 1 & \nu^- \end{pmatrix} \begin{pmatrix} E_R^t \\ E_L^t \end{pmatrix}_s , \tag{3.24}$$

where the scattering term $\nu^\pm$ is given by

$$\nu^\pm = \frac{(S_{11} - S_{22} \mp 2jS_{12})}{S_{11} + S_{22}} e^{\pm 2j\alpha}. \tag{3.25}$$

Equation (3.25) can also be written as

$$\nu^\pm = \left| \frac{S_{11} - S_{22} \mp 2jS_{12}}{S_{11} + S_{22}} \right| e^{j(\delta_\pm \pm 2\alpha)}, \tag{3.26}$$

where $\delta_\pm$ is the scattering differential phase shift.

For ellipsoids, $S_{12} = 0$ (Humphries, 1974a) so that $\delta_+ = \delta_-$ and equation (3.26) reduces to

$$\nu^\pm = \left| \frac{S_{11} - S_{22}}{S_{11} + S_{22}} \right| e^{j(\delta \pm 2\alpha)} = \nu e^{j(\delta \pm 2\alpha)}, \tag{3.27}$$

S_{11} and S_{22} are given by

$$S_{11} = k_o^2[(\varepsilon_1 - \varepsilon_2)\sin^2\eta + \varepsilon_2], \tag{3.28}$$

$$S_{22} = k_o^2\varepsilon_2, \tag{3.29}$$

where k_o is the propagation constant of the surrounding medium and η, as defined in Figure 3.3b, is the angle between the reference axis of the scatterer and the Z-axis. The polarizabilities of the scatterer ε_1 and ε_2 are given by (Van de Hulst, 1957)

$$\frac{V}{4\pi\varepsilon_i} = L_i + \frac{1}{m^2 - 1} \qquad i = 1, 2, \tag{3.30}$$

where V and m^2 are the volume and the dielectric constant of the particle. For oblate spheroids the shape factor L_i is given by

$$L_1 = \frac{1 + F^2}{F^2}[1 - \frac{1}{F}\arctan F], \tag{3.31}$$

$$L_2 = \frac{1 - L_1}{2}, \tag{3.32}$$

where

$$F^2 = \left(\frac{a}{b}\right)^2 - 1, \tag{3.33}$$

where a is the length of the symmetry axis and b is the length of the axis perpendicular to a.

3.5 The Net Effects of Propagation and Scattering

The net effects of propagation and scattering on the transmitted wave are obtained by combining equations (3.13), (3.18), and (3.24)

$$\begin{pmatrix} E^r_R \\ E^r_L \end{pmatrix}_{Z=0} = \frac{e^{-2jkr}}{2r^2}(S_{11}+S_{22})\mathbf{P}^T \begin{pmatrix} \nu^+ & 1 \\ 1 & \nu^- \end{pmatrix} \mathbf{P} \begin{pmatrix} E^t_R \\ E^t_L \end{pmatrix}_{Z=0} , \tag{3.34}$$

which upon expansion gives

$$\begin{pmatrix} E^r_R \\ E^r_L \end{pmatrix}_{Z=0} = \frac{e^{-2jkr}}{2r^2}(S_{11}+S_{22}) \begin{pmatrix} \xi^+ & \xi^o \\ \xi^o & \xi^- \end{pmatrix} \begin{pmatrix} E^t_R \\ E^t_L \end{pmatrix}_{Z=0} , \tag{3.35}$$

where

$$\xi^o = \frac{1 + \nu^+ pe^{j(\chi-2\tau)} + \nu^- pe^{j(\chi+2\tau)} + (pe^{j\chi})^2}{1-(pe^{j\chi})^2}, \tag{3.36}$$

$$\xi^\pm = \frac{\nu^\pm + 2pe^{j(\chi\pm2\tau)} + \nu^\mp [pe^{j(\chi\pm2\tau)}]^2}{1-(pe^{j\chi})^2}. \tag{3.37}$$

As indicated by McCormick and Hendry (1975), the transmitted field components at $Z=0$ are related to the transmitted wave amplitudes (M_1 and M_2) at the reference plane A (see Figure 3.1) by

$$\begin{pmatrix} E^t_R \\ E^t_L \end{pmatrix}_{Z=0} = \left(\frac{G}{2\pi Y_o}\right)^{\frac{1}{2}} e^{j\varphi} \begin{pmatrix} M_1 \\ M_2 \end{pmatrix}_A , \tag{3.38}$$

and the received field components at $Z=0$ are related to the received wave amplitudes (R_1 and R_2) at the reference plane T by

$$\begin{pmatrix} R_1 \\ R_2 \end{pmatrix}_T = \frac{-j\lambda}{2}\left(\frac{GY_o}{\pi}\right)^{\frac{1}{2}} e^{j\varphi} \begin{pmatrix} E^r_R \\ E^r_L \end{pmatrix}_{Z=0} , \tag{3.39}$$

where G and φ are the gain and the phase patterns of the antenna, λ is the wavelength, and Y_o is the free space admittance.

Substituting equations (3.38) and (3.39) into equation (3.35) gives

$$\begin{pmatrix} R_1 \\ R_2 \end{pmatrix}_T = C\sigma^{\frac{1}{2}} \begin{pmatrix} \xi^+ & \xi^o \\ \xi^o & \xi^- \end{pmatrix} \begin{pmatrix} M_1 \\ M_2 \end{pmatrix}_A , \tag{3.40}$$

where the particle backscatter cross section σ is defined as

$$\sigma = \pi(S_{11} + S_{22})^2, \tag{3.41}$$

and

$$C = \frac{-j\lambda G}{8\pi^{\frac{3}{2}} r^2} e^{2j(\varphi - kr)}. \tag{3.42}$$

In general, only one polarization is transmitted. If circular polarization radiation of unit amplitude is transmitted, then it follows from equation (3.40) that the orthogonal and main components of the radiation backscattered by a single particle are

$$R_1 = C\sigma^{\frac{1}{2}}\xi^{\pm}, \tag{3.43}$$

$$R_2 = C\sigma^{\frac{1}{2}}\xi^{o}, \tag{3.44}$$

where upper and lower signs refer to the transmission of RHC and LHC polarizations respectively.

3.6 The Received Signal from an Assembly of Particles

To this point only a single scatterer has been considered. For targets comprising assemblies of precipitation particles, the main and orthogonal components of the received signal can be written as

$$R_1 = \sum_{i=1}^{N} R_{1_i} , \quad R_2 = \sum_{i=1}^{N} R_{2_i}, \tag{3.45}$$

where single scattering is assumed. N is the total number of particles and the subscript i refers to the i^{th} particle. The received wave amplitudes R_{1_i} and R_{2_i} are given by equations (3.43) and (3.44).

As discussed in Chapter I, the radar observables are the time-averaged products of $R_1R_1^*$, $R_2R_2^*$, and $R_1R_2^*$, i.e.,

$$W_1 = < R_1R_1^* >, \tag{3.46}$$

$$W_2 = < R_2R_2^* >, \tag{3.47}$$

$$W = W_3 + jW_4 =< R_1R_2^* > . \tag{3.48}$$

McCormick and Hendry (1975, 1976) suggested a model where precipitation particles were divided into groups according to size, shape, phase state, and orientation. They identified these groups by the index l, l =1, 2, 3, ..., L, with N_l scatterers in group l. It was further assumed that in group l there was a distribution $T_l(\alpha - \alpha_l)$ of the canting angle α about the mean canting angle $\bar{\alpha}_l$. Under these assumptions, the radar observables W_1, W_2, and W can be obtained from equations (3.46), (3.47) and (3.48) by summing over the L groups. For negligible propagation effects, i.e.,

$$pe^{j(\chi \pm 2\tau)} = 0,$$

it follows that

$$W_1 = |C|^2 \sum_{l=1}^{L} N_l\sigma_l |\nu e^{j(\delta_l \pm 2\alpha_l)}|^2, \tag{3.49}$$

$$W_2 = |C|^2 \sum_{l=1}^{L} N_l\sigma_l, \tag{3.50}$$

$$W = |C|^2 \sum_{l=1}^{L} N_l \sigma_l \nu_l \int_{-\frac{\pi}{2}+\bar{\alpha}_l}^{\frac{\pi}{2}+\bar{\alpha}_l} T_l(\alpha - \bar{\alpha}_l) e^{j(\delta_l \pm 2\alpha)} d\alpha \tag{3.51}$$

$$= |C|^2 \sum_{l=1}^{L} N_l \sigma_l \nu_l \rho_{\alpha_l} e^{j(\delta \pm 2\bar{\alpha}_l)}, \tag{3.52}$$

where T_l is symmetrical about $\bar{\alpha}$. The degree of orientation, ρ_{α_l}, is given by

$$\rho_{\alpha_l} = \int_{-\frac{\pi}{2}}^{\frac{\pi}{2}} \cos(\alpha - \bar{\alpha}_l) T_l(\alpha - \bar{\alpha}_l) d(\alpha - \bar{\alpha}_l). \tag{3.53}$$

The integration of equation (3.53) may readily be performed for different distribution functions. Assuming a Gaussian probability distribution, Torlaschi *et al.* (1984) showed that

$$\rho_\alpha = e^{-2\sigma_\alpha^2} \operatorname{Re}\left\{ \operatorname{erf}\left(\frac{\pi}{2\sqrt{2\sigma_\alpha}} + j\sqrt{2\sigma_\alpha} \right) \right\}, \tag{3.54}$$

where σ_α is the standard deviation of the canting angle (in radians). Figure 3.4 (Torlaschi *et al.*, 1984) shows ρ_α for different σ_α. It can be seen that the more aligned the particles, the closer ρ_α is to unity and the more randomly canted the particles, the closer ρ_α is to zero.

For convenience, consider the following relation

$$\begin{aligned} \frac{W}{W_2} &= \frac{W_3 + jW_4}{W_2} \\ &= \sum_{l=1}^{L} N_l \sigma_l \rho_{\alpha_l} \nu_l e^{j(\delta_l \pm 2\bar{\alpha}_l)} / \sum_{l=1}^{L} N_l \sigma_l \\ &= \rho_\alpha \bar{\nu} e^{j(\bar{\delta} \pm 2\bar{\alpha})}. \end{aligned} \tag{3.55}$$

The complex correlation, as defined by equation (1.25), is

$$v_c = \rho_c e^{j\Phi} = \frac{W}{\sqrt{W_1 W_2}} = \frac{W_3 + jW_4}{\sqrt{W_1 W_2}}. \tag{3.56}$$

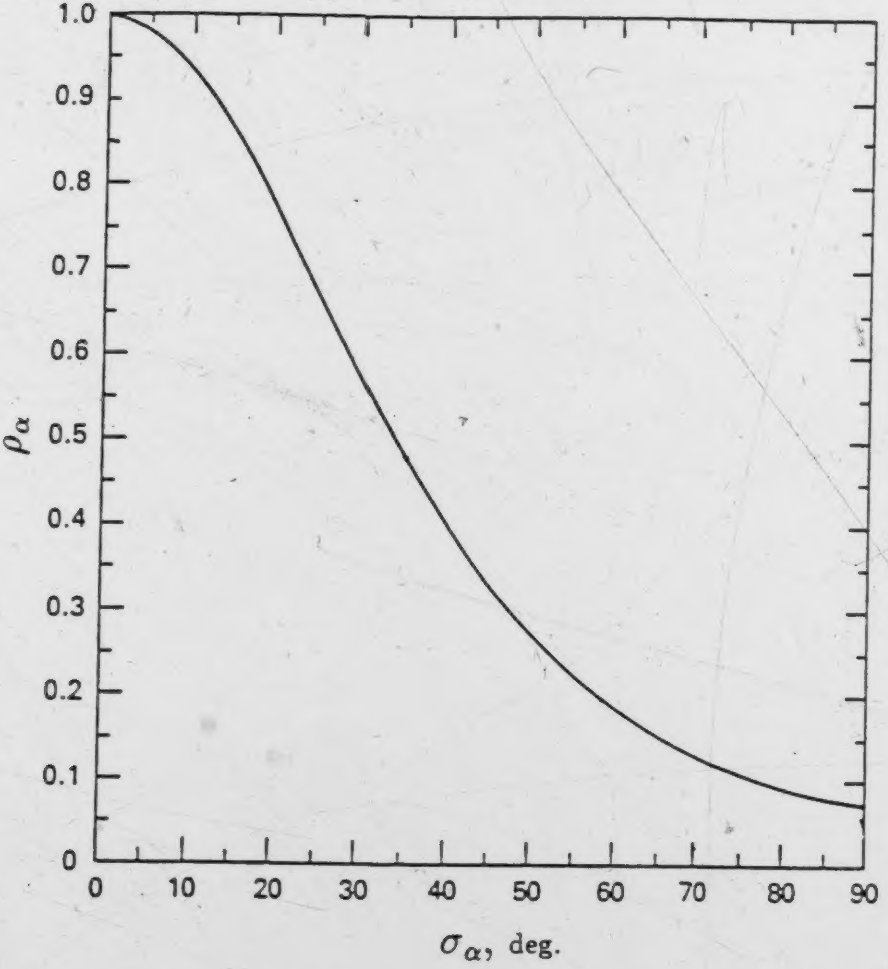

Figure 3.4 Degree of orientation ρ_α versus standard deviation of canting angle σ_α.

It can be shown that the effective phase difference between the two orthogonal components Φ_c is given by

$$\Phi_c = \arg W = \arctan \frac{W_4}{W_3}, \tag{3.57}$$

and from equation (3.55), it follows that

$$\Phi_c = \bar{\delta} \pm 2\bar{\alpha}. \tag{3.58}$$

The degree of correlation ρ_c is given by

$$\rho_c = \frac{|W|}{\sqrt{W_1 W_2}}, \tag{3.59}$$

which can be rewritten as

$$\rho_c = \left(\frac{|W|^2}{W_1 W_2} \right)^{\frac{1}{2}} = \left(\frac{|W|^2}{W_2^2} \frac{W_2}{W_1} \right)^{\frac{1}{2}}. \tag{3.60}$$

The ratio of the orthogonal component W_1 to the main component W_2 is

$$\begin{aligned} \frac{W_1}{W_2} &= \sum_{l=1}^{L} N_l \sigma_l \left| \nu_l e^{j(\delta_l \pm 2\alpha_l)} \right|^2 \Big/ \sum_{l=1}^{L} N_l \sigma_l \\ &= \overline{\left| \nu e^{j(\delta \pm 2\alpha)} \right|^2}. \end{aligned} \tag{3.61}$$

Combining equations (3.55) and (3.60) with equation (3.61) gives

$$\rho_c = \frac{\rho_\alpha \left| \bar{\nu} e^{j(\bar{\delta} \pm 2\bar{\alpha})} \right|}{\left(\overline{\left| \nu e^{j(\delta \pm 2\alpha)} \right|^2} \right)^{\frac{1}{2}}}. \tag{3.62}$$

In addition to the equivalent radar reflectivity factor Z_e which is obtained from the main component W_2, three other radar parameters are derived from the observables. These are defined by (Barge, 1972; McCormick and Hendry, 1975)

$$\begin{aligned} CDR &= 10 \log_{10} \frac{W_1}{W_2}, && (3.63) \\ ORTT &\equiv \rho_c = \frac{|W|}{\sqrt{W_1 W_2}}, && (3.64) \\ ALD &= \frac{1}{2} (\arg W - \pi), && (3.65) \end{aligned}$$

and from equations (3.58), (3.61), and (3.62) it follows that

$$CDR \doteq 10\log_{10}\left(\overline{|\nu e^{j(\bar{\delta}\pm 2\bar{\alpha})}|^2}\right), \tag{3.66}$$

$$ORTT = \frac{\bar{\rho}_\alpha |\bar{\nu} e^{j(\bar{\delta}\pm 2\bar{\alpha})}|}{\left(\overline{|\nu e^{j(\delta\pm 2\alpha)}|^2}\right)^{\frac{1}{2}}}, \tag{3.67}$$

$$ALD = \frac{1}{2}\left\{(\bar{\delta} \pm 2\bar{\alpha}) - \pi\right\}, \tag{3.68}$$

which indicate that for negligible propagation effects, the circular depolarization ratio CDR is directly related to the scattering properties of the particles, the correlation parameter $ORTT$ is a measure of degree of orientation, and the parameter ALD is a function of the mean canting angle $\bar{\alpha}$ and the mean scattering differential phase shift $\bar{\delta}$. This is not true when propagation effects become an important factor. Such effects on these parameters will be discussed in Chapter V.

3.7 Relationship between Differential Reflectivity and Circular Polarization Parameters

As previously mentioned, the differential reflectivity (Z_{DR}) technique proposed by Seliga and Bringi (1976) involves measuring the reflectivity factors due to horizontally and vertically polarized incident radiation. McCormick (1979) demonstrated that circular polarization quantities, namely CDR and the real part of W/W_2, provide a very good estimate of Z_{DR}.

The differential reflectivity is defined as

$$Z_{DR} = 10\log_{10}\frac{Z_H}{Z_V}. \tag{3.69}$$

Assuming no propagation effects and a single symmetric particle oriented with its minor axis near vertical ($\alpha \approx 0^o$)

$$\frac{Z_H}{Z_V} = \frac{|S_{11}|^2}{|S_{22}|^2}. \tag{3.70}$$

For a single particle, the circular complex correlation W is obtained from equations (3.43) and (3.44)

$$W = R_1 R_2^* = \pi |C|^2 (|S_{11}|^2 - |S_{22}|^2) e^{j(\delta \pm 2\alpha)}, \tag{3.71}$$

and for a Rayleigh scatterer ($\delta = 0^o$) it reduces to

$$W = \pi |C|^2 (|S_{11}|^2 - |S_{22}|^2) e^{\pm 2j\alpha}. \tag{3.72}$$

The real part of W is given by

$$\mathrm{Re}(W) = \pi |C|^2 (|S_{11}|^2 - |S_{22}|^2) \cos 2\alpha, \tag{3.73}$$

which for $\alpha \approx 0^o$ reduces to

$$\mathrm{Re}(W) = \pi |C|^2 (|S_{11}|^2 - |S_{22}|^2). \tag{3.74}$$

The observables W_1 and W_2 are also obtained from equations (3.43) and (3.44)

$$W_1 = R_1 R_1^* = \pi |C|^2 |S_{11} - S_{22}|^2, \tag{3.75}$$

$$W_2 = R_2 R_2^* = \pi |C|^2 |S_{11} + S_{22}|^2. \tag{3.76}$$

Hence

$$W_1 + W_2 = 2\pi |C|^2 (|S_{11}|^2 + |S_{22}|^2). \tag{3.77}$$

Combination of equations (3.74) and (3.77) gives

$$|S_{11}|^2 = \frac{1}{4\pi |C|^2} [W_1 + W_2 + 2\mathrm{Re}(W)], \tag{3.78}$$

$$|S_{22}|^2 = \frac{1}{4\pi |C|^2} [W_1 + W_2 - 2\mathrm{Re}(W)]. \tag{3.79}$$

Therefore equation (3.70) becomes

$$\frac{Z_H}{Z_V} = \frac{|S_{11}|^2}{|S_{22}|^2} = \frac{W_1 + W_2 + 2\mathrm{Re}(W)}{W_1 + W_2 - 2\mathrm{Re}(W)}, \tag{3.80}$$

which can be rewritten as

$$\frac{Z_H}{Z_V} = \frac{1 + [2\mathrm{Re}(\frac{W}{W_2}) \times \frac{1}{1+W_1/W_2}]}{1 - [2\mathrm{Re}(\frac{W}{W_2}) \times \frac{1}{1+W_1/W_2}]}. \tag{3.81}$$

Finally, Z^c_{DR}[1] is obtained by a combination of equations (3.69) and (3.81).

$$Z^c_{DR} = 10\log_{10}\frac{1+\mu}{1-\mu}, \tag{3.82}$$

where

$$\mu = \frac{2\mathrm{Re}(\frac{W}{W_2})}{1 + \frac{W_1}{W_2}}, \tag{3.83}$$

which can be expressed in terms of $ORTT$ and CDR as

$$\mu = \frac{2ORTT(10^{\frac{CDR}{10}})^{\frac{1}{2}}}{1 + 10^{\frac{CDR}{10}}}. \tag{3.84}$$

Here $ORTT$ is a fraction (0 to 1) and CDR is in decibels.

The radar determines $< |S_{11}|^2 >, < |S_{22}|^2 >, W_1 = < R_1R_1^* >, W_2 = < R_2R_2^* >$, and $W = < R_1R_2^* >$ and not the respective instantaneous values. However for rain, R_1 and R_2 are highly correlated (McCormick and Hendry, 1975). Hence

$$\left\langle \frac{R_1R_2^*}{|R_1|^2 + |R_2|^2} \right\rangle \approx \frac{< R_1R_2^* >}{< |R_1|^2 > + < |R_2|^2 >}. \tag{3.85}$$

The correlation between S_{11} and S_{22} is even higher (Seliga and Bringi, 1976). Therefore

$$\left\langle \frac{|S_{11}|^2}{|S_{22}|^2} \right\rangle \approx \frac{< |S_{11}|^2 >}{< |S_{22}|^2 >}. \tag{3.86}$$

---

[1] The superscript c will be used to denote values of Z_{DR} derived from circular polarization measurements.

The calculation of Z_{DR}^{c} using the above approximation has been found to be valid at 2.88 GHz and 9.6 GHz in the absence of propagation effects (Holt, 1984). Hendry and Antar (1984b) and Hendry *et al.* (1986) showed that there is agreement between values of Z_{DR} measured with linear polarization and the corresponding quantities calculated using the approximation of equation (3.82).

3.8 Intrinsic Polarization Properties of Rain and Hail

The principles of polarization diversity radar discussed in the previous sections were modelled by Torlaschi *et al.* (1984) to calculate Z_e, CDR, and $ORTT$ for rain only and hail only. These theoretical models were based on the assumption that propagation has a negligible effect so that calculated values represent the intrinsic properties of precipitation particles. For raindrops, Torlaschi *et al.* (1984) used the drop size distribution of Marshall and Palmer (1948) and the shape-size relationship of Pruppacher and Pitter (1971). For hailstones, they employed the size distribution of Cheng and English (1983) and the shape-size relationship of Barge and Isaac (1973). Figures 3.5 through 3.7 show how Z_e, CDR, and $ORTT$ are related to an assembly of raindrops at a temperature of 10 °C and to a collection of hailstones at a temperature of 0 °C. These calculations were carried out for the operating frequency of the Alberta Research Council's radar (2.88 GHz). The results clearly indicate that rain produces values of Z_e, CDR, and $ORTT$ different from those of precipitation consisting solely of hail. It should be noted that the Cheng and English hail size distribution is limited to a maximum precipitation rate of 88 mm/hr. Therefore caution must be exercised when using the hail curves to interpret values of hail precipitation rate greater then about 50 mm/hr. However, such values are unlikely to occur often (Torlaschi *et al.*, 1984).

The values of CDR and $ORTT$ presented in Figures 3.6 and 3.7 along with equation (3.82) were used to calculate Z_{DR}^{c}. The results are shown in Figure 3.8. It is apparent that for rain, Z_{DR}^{c} lies between 0.55 and 2.5 dB and increases with rainfall rate. For hail, Z_{DR}^{c} assumes values less than 0.5 dB quite independent of hailfall rate. These results are in agreement with those of Aydin *et al.* (1986), confirming McCormick's (1979) approximation for deriving Z_{DR}^{c} from CDR and $ORTT$ where propagation effects are negligible.

So far it has been assumed that propagation effects are not significant, an assumption which is invalid for the propagation of centimeter waves through heavy precipitation. These effects will be discussed in Chapter V.

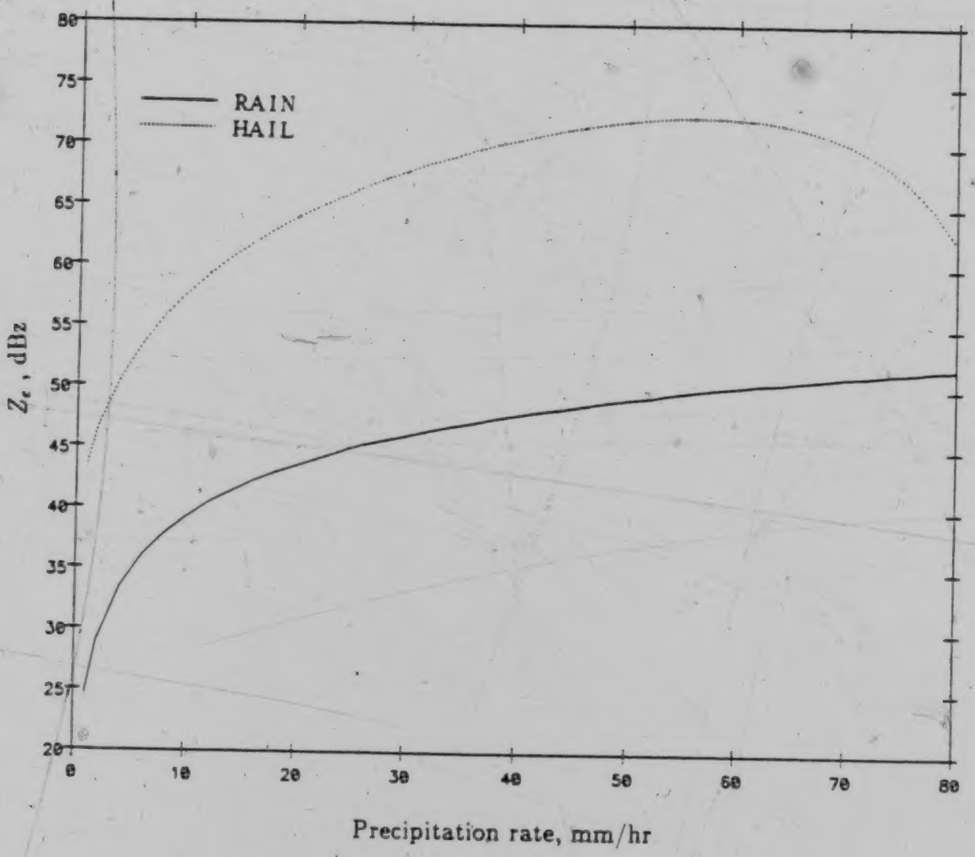

Figure 3.5 Relationship between intrinsic Z_e and precipitation rate for an assembly of raindrops only at a temperature of $10^{\circ}C$ and a collection of wet hailstones at a temperature of $0^{\circ}C$.

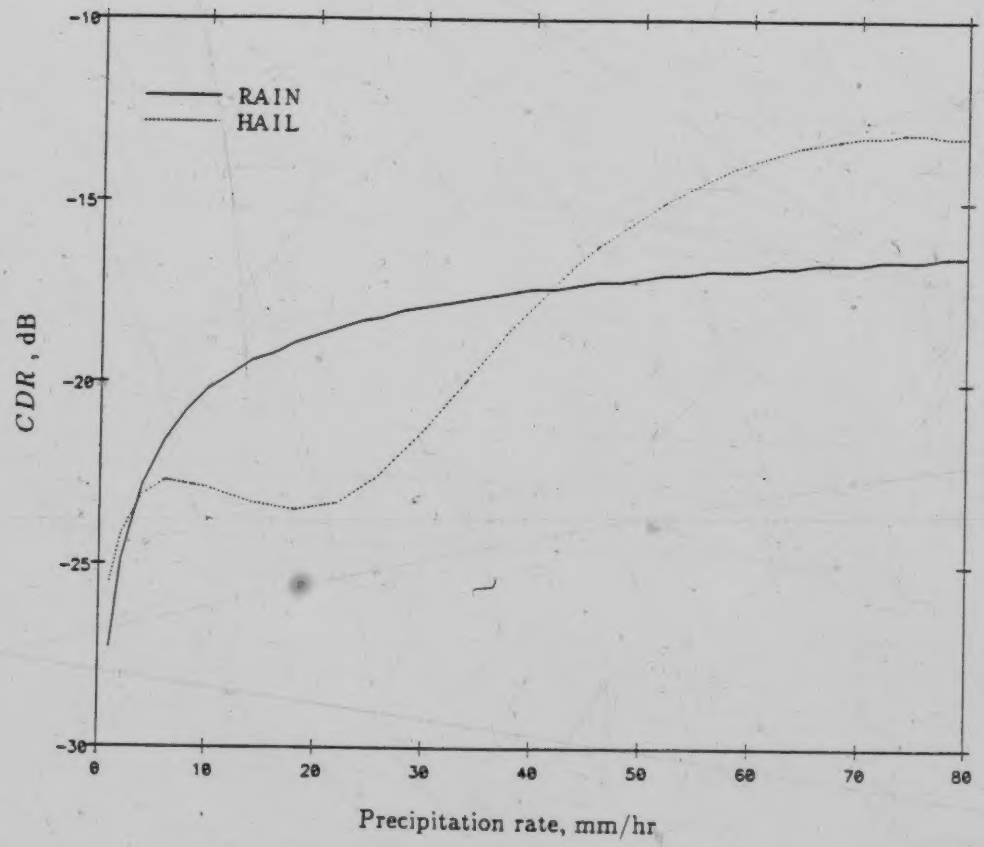

Figure 3.6 Relationship between intrinsic CDR and precipitation rate for an assembly of raindrops only at a temperature of 10°C and a collection of wet hailstones at a temperature of 0°C.

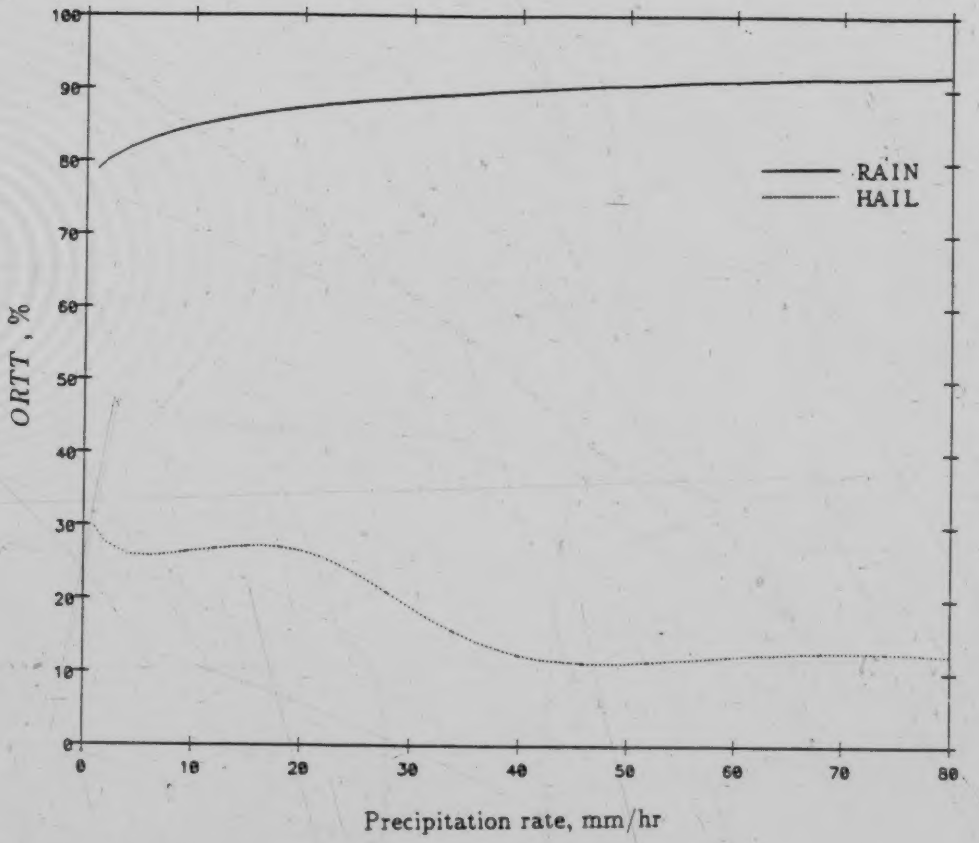

Figure 3.7 Relationship between intrinsic *ORTT* and precipitation rate for an assembly of raindrops only at a temperature of 10°*C* and a collection of wet hailstones at a temperature of 0°*C*.

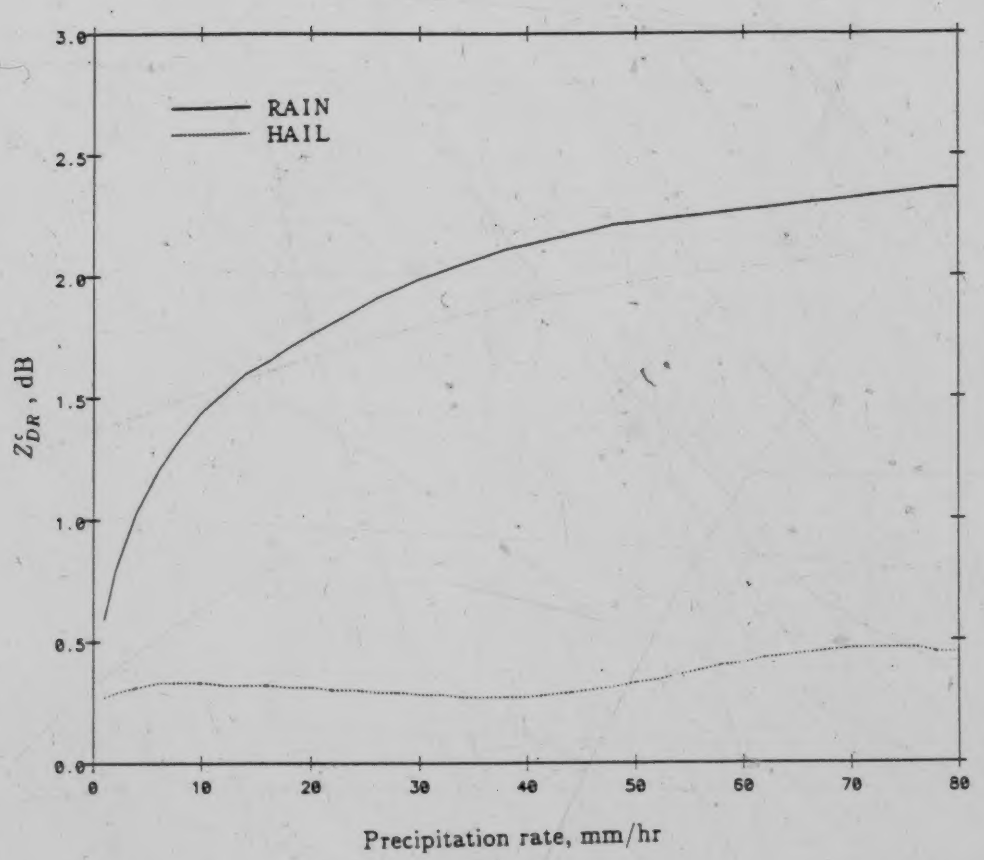

Figure 3.8 Relationship between intrinsic Z_{DR}^{c} and precipitation rate for an assembly of raindrops only at a temperature of $10°C$ and a collection of wet hailstones at a temperature of $0°C$.

CHAPTER IV

The Alberta Research Council S-band Radar

4.1 The Radar System

All the observations presented in this research were made with the Alberta Research Council's S-band radar (see Plate I). The operational area and location of the radar are illustrated in Figure 4.1. The radar characteristics are summarized in Table 4.1.

The radar includes a polarization diversity system comprising a dual-polarization antenna and a dual-channel receiving system. A complete description of the radar system has been given by Leung (1976) and Stanley-Jones *et al.* (1984). A simplified block diagram of the microwave circuitry of the antenna is shown in Figure 4.2 (Leung, 1976). The turnstile located in front of the antenna dish is a rectangular waveguide to circular waveguide coupler with two inputs. The signal in the upper waveguide is radiated as a RHC polarized wave while the signal in the lower waveguide is radiated as a LHC wave. Transmission of RHC or LHC is produced by excitation of the appropriate waveguide. Linear and elliptical polarizations are transmitted by superposition of RHC and LHC polarized waves having the correct phase and amplitude relationship to produce the desired radiation. The phase shifter is a microwave device which controls the phase difference between the RHC and LHC polarized signals and hence determines the orientation of the transmitted

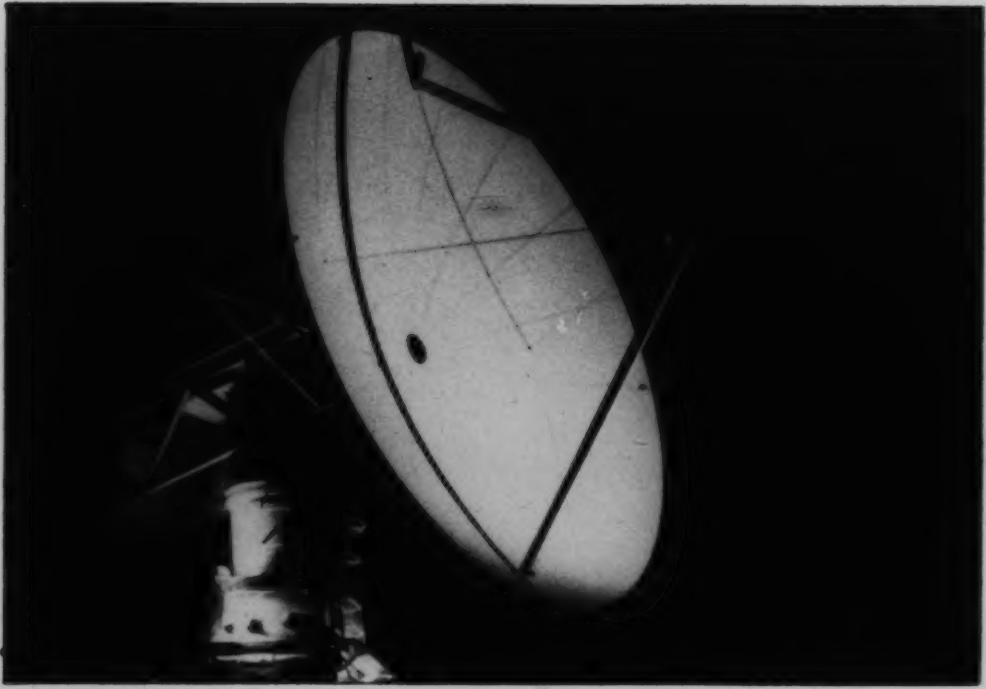

Plate I The Alberta Research Council's S-band polarization diversity radar.

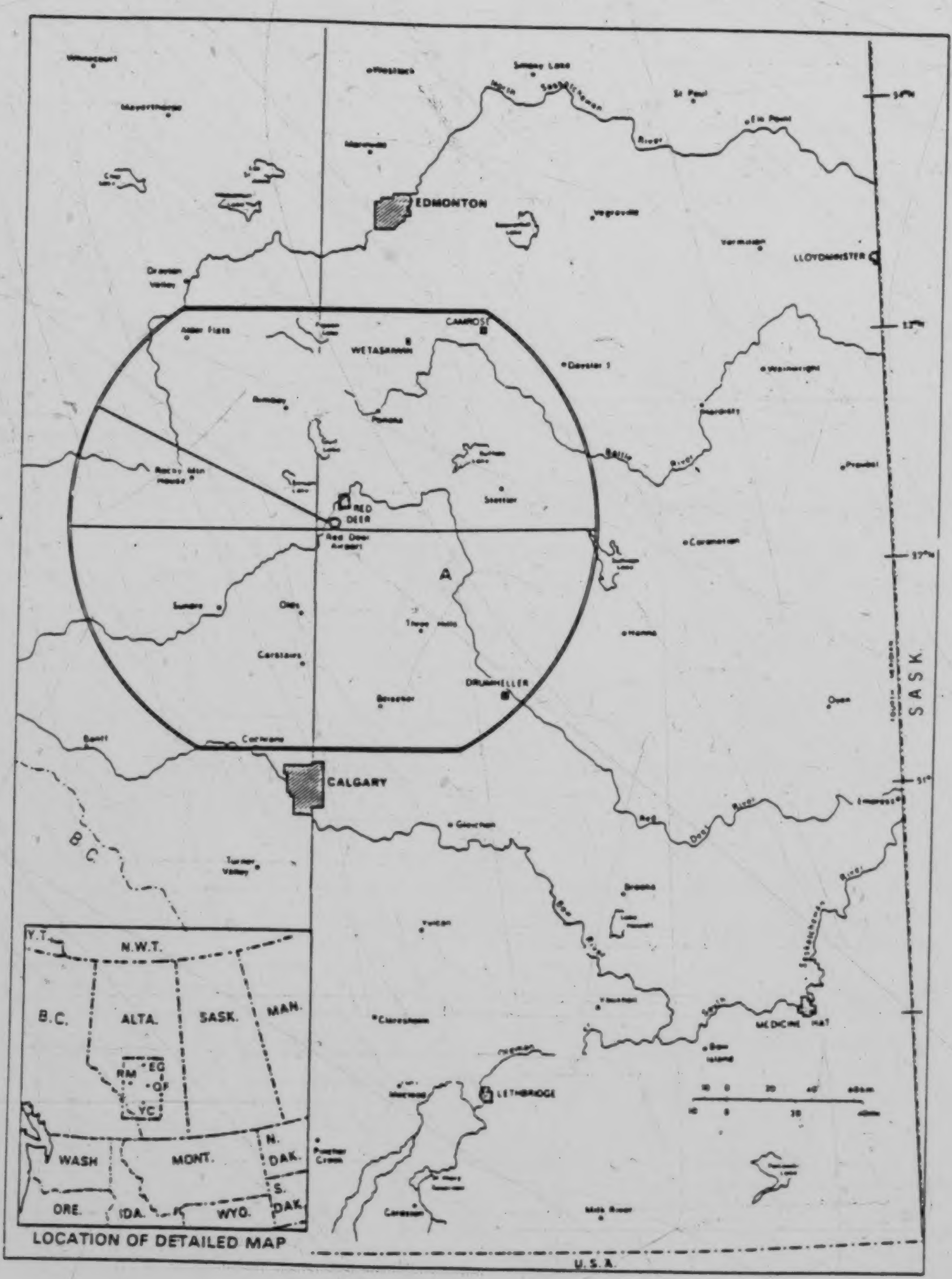
Whitecourt
Mayerthorpe
Westlock
Smoky Lake
North Saskatchewan River
St Paul
Elk Point
EDMONTON
Vegreville
Vermilion
LLOYDMINSTER
Drayton Valley
Alder Flats
CAMROSE
WETASKIWIN
Rimbey
Ponoka
Battle River
Wainwright
Provost
Rocky Mtn House
RED DEER
Red Deer Airport
Stettler
Coronation
A
Sundre
Olds
Three Hills
Hanna
Carstairs
DRUMHELLER
Oyen
Banff
Cochrane
CALGARY
Red Deer River
Empress
Gleichen
B.C.
SASK
Turner Valley
Brooks
Bow River
Vulcan
Claresholm
MEDICINE HAT
LETHBRIDGE
54°N
53°N
52°N
51°
Y.T.
N.W.T.
B.C.
ALTA.
SASK.
MAN.
RM
EG
OF
YC
WASH
MONT.
N. DAK.
S. DAK.
ORE.
IDA.
WYO.
LOCATION OF DETAILED MAP
U.S.A.

Figure 4.1 Location and operational area of the ARC S-band radar.

Table 4.1 The Alberta Research Council S-band radar characteristics

frequency	2.88 GHz
PRF	478 Hz
pulse duration	1.0 μsec
typical peak power	400 kW
beam width	1.15° (all planes)
antenna gain	43.2 dB (at pedestal)
azimuth rotation rate	8 RPM
elevation program	helical scan: 1° per azimuth rotation: 0° to 8° or 0° to 20° (complete cycle time 1.5 min or 3 min)

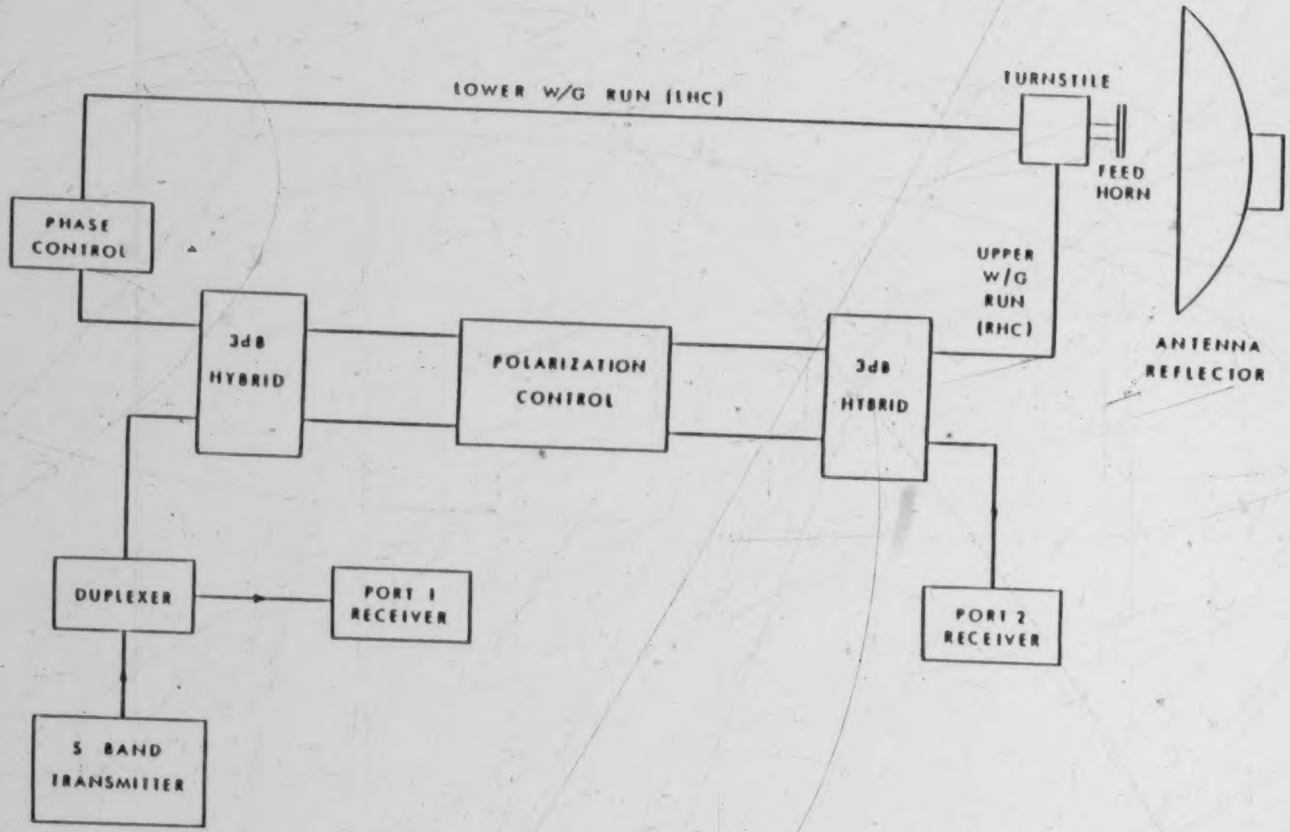
LOWER W/G RUN (LHC)
TURNSTILE
FEED HORN
PHASE CONTROL
UPPER W/G RUN (RHC)
ANTENNA REFLECTOR
3dB HYBRID
POLARIZATION CONTROL
3dB HYBRID
DUPLEXER
PORT 1 RECEIVER
PORT 2 RECEIVER
S BAND TRANSMITTER

Figure 4.2 Block diagram of the antenna microwave circuitry of the ARC S-band radar.

ellipse. The duplexer is an automatic switch that protects the receivers from the powerful transmitted pulse. The horn is a waveguide to free space matching device. The 3 dB hybrid and the polarization control are microwave devices which split the input power between the two waveguides and therefore determine the shape and sense of rotation of the transmitted ellipse. During the Alberta Hail Project operations the antenna was adjusted to transmit LHC polarized wave and the phase difference was set to 0°.

The radar echo, which in general is elliptically polarized, is resolved by the turnstile into a main (RHC) component and an orthogonal (LHC) component. These signals are received by two separate receivers (port 1 and port 2). Figure 4.3 (Humphries and Barge, 1979) shows a block diagram of the receiver system. In each port, the intermediate frequency (IF) signal is logarithmically detected and then integrated in 7 μs intervals, or bins, which correspond to 1.05 km in range. The signals are digitized and then fed to an azimuth integrator which adds the data from the same range bin for 1° azimuth (equivalent to 10 radar pulses). The phase discriminator differentiates the phase between port 1 and port 2 IF signals. It utilizes two balanced mixers. One is fed by an IF signal of port 1 and port 2 and the other is fed by a 90° phase shifted port 1 IF signal and the unaltered port 2 IF signal. The range and azimuth integration of the outputs of the two mixers, port 3 and port 4, is similar to that for port 1 and port 2. The data of the four ports, together with the time and antenna elevation and azimuth information, are stored on magnetic tape.

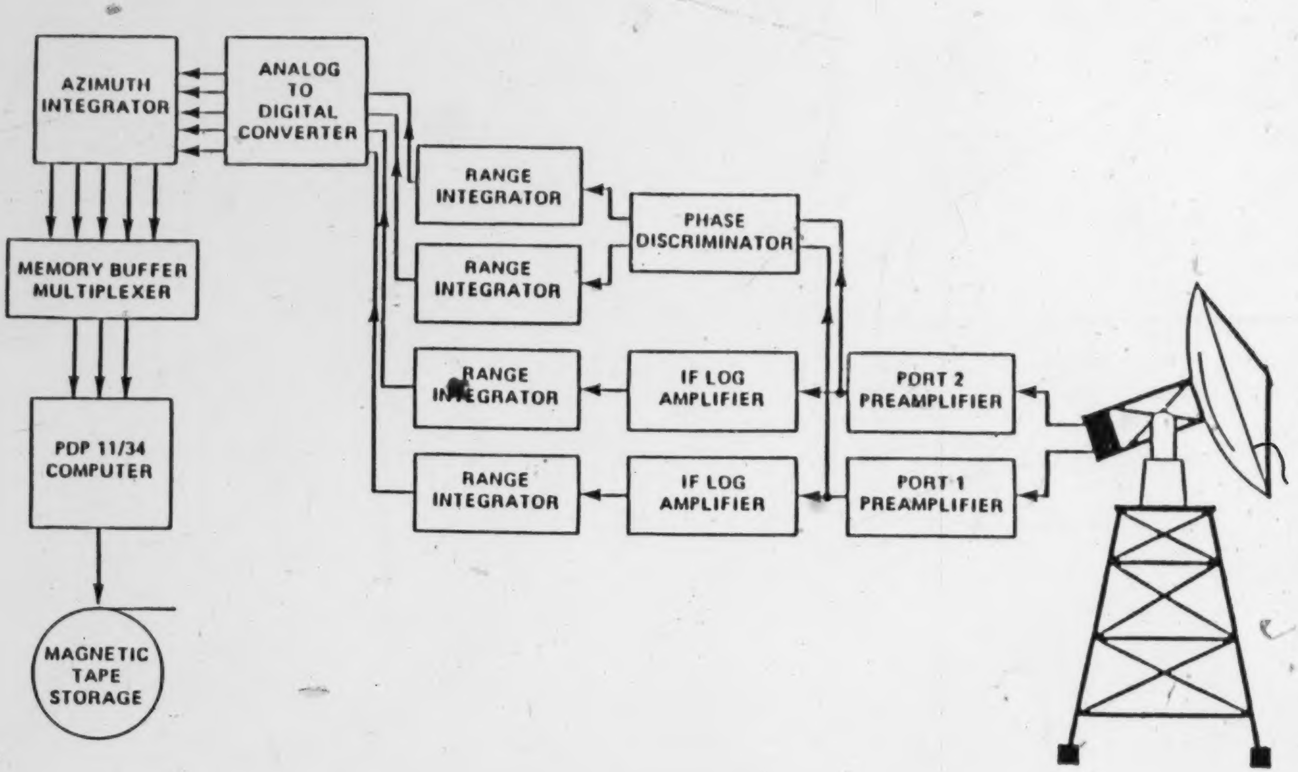
AZIMUTH INTEGRATOR
ANALOG TO DIGITAL CONVERTER
RANGE INTEGRATOR
PHASE DISCRIMINATOR
RANGE INTEGRATOR
MEMORY BUFFER MULTIPLEXER
RANGE INTEGRATOR
IF LOG AMPLIFIER
PORT 2 PREAMPLIFIER
PDP 11/34 COMPUTER
RANGE INTEGRATOR
IF LOG AMPLIFIER
PORT 1 PREAMPLIFIER
MAGNETIC TAPE STORAGE

Figure 4.3 Block diagram of the receiver system of the ARC S-band radar.

4.2 Calibration

A full description of the calibration procedures for the radar system has been given by Barge *et al.* (1976), Humphries *et al.* (1977), and Stanley-Jones *et al.* (1984). Briefly, the major calibration is carried out by injecting a known RF signal into the antenna. With the polarization control set to linear polarization, the signal is split equally into port 1 and port 2. The injected signal and the corresponding digital data values are stored in the computer. A computer program is available to extract and display these calibration data graphically. Figure 4.4 shows an example of a set of the major calibration data performed on 7 July 1984. The known signal levels are plotted versus the corresponding raw data values. The major calibration is performed at least once a day when the radar is operational. The calibration data are required to convert the collected raw data values of port 1 and port 2 to power levels.

The calibration of the antenna and the phase discriminator is carried out by pointing the antenna at a remote transmitter, or monitor, situated on top of a 27.4 m tower located 400 m from the radar. This monitor can be set to transmit RHC or LHC polarizations as well as linear polarization of any orientation.

In antenna calibration, the polarization control device is used to direct a signal transmitted by the monitor to the appropriate port. By setting the antenna to transmit LHC while the monitor is transmitting LHC, the signal is directed to port 1 so that the amount of signal which leaks into port 2 can be measured. The difference between the signals received by port 1 and port 2 is called the isolation. By setting

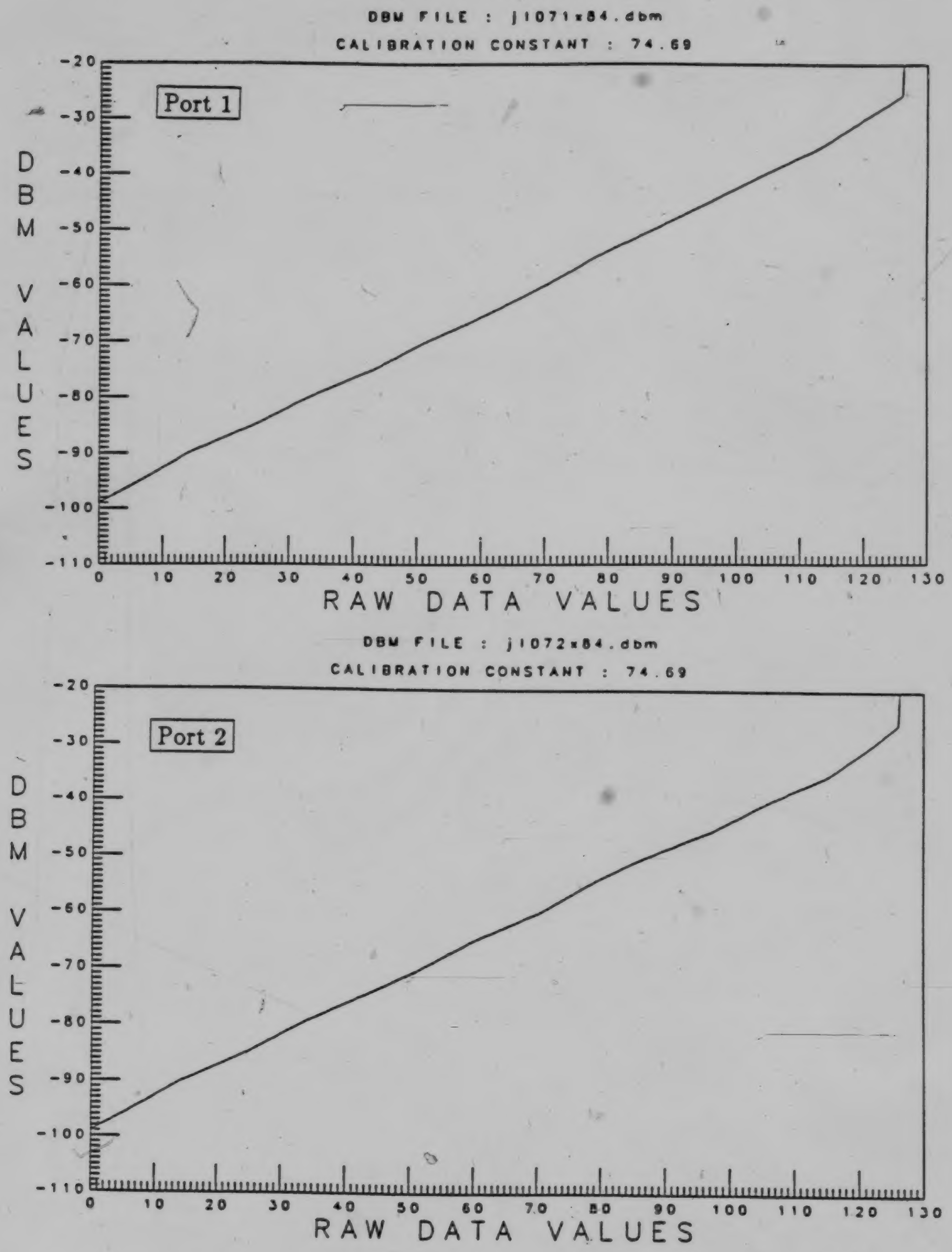

Figure 4.4 Graphs of the ARC S-band receiver calibration for port 1 and port 2 for 7 July 1984. Shown are the known RF input signals as a function of the raw data values.

the antenna to transmit LHC and the monitor to transmit linear polarization, equal signals should be received by the two ports. By inserting appropriate attenuation, the relative signal to noise ratio can be measured.

To calibrate the phase discriminator outputs, two methods are used. In the first method (phase shifter method), the antenna is set to transmit LHC polarization while the monitor transmits linear vertical polarization. The RF phase shifter is then rotated. This changes the phase of one of the received components with respect to the other. At each step, the outputs of the phase ports, port 3 and port 4, are obtained. In general, the phase shifter is rotated in 20° steps until a complete revolution is obtained. The raw data values of port 3 and port 4, together with the phase shifter setting, are then stored in the computer. This procedure is performed on a daily basis. Figure 4.5 shows an example of a set of phase shifter calibration curves for 7 July 1984. The phase shifter setting is plotted along the abscissa and the corresponding raw data values of port 3 and port 4 are plotted along the ordinate.

The second method (monitor method) involves setting the phase shifter to 0° and rotating the monitor while it is transmitting linear polarization. The monitor orientation is then recorded, along with the outputs of port 3 and port 4. This method is carried out at irregular intervals over each summer of operation. It provides information on the correspondence between the phase shift and the monitor orientation which is related to the orientation of a dipole scatterer. Figure 4.6 shows an example of a set of the monitor calibration data for 7 July 1984. The outputs of port 3 and port 4 are plotted versus the monitor orientation. The curves represent one complete rotation in a clockwise fashion as viewed from the radar site. Since

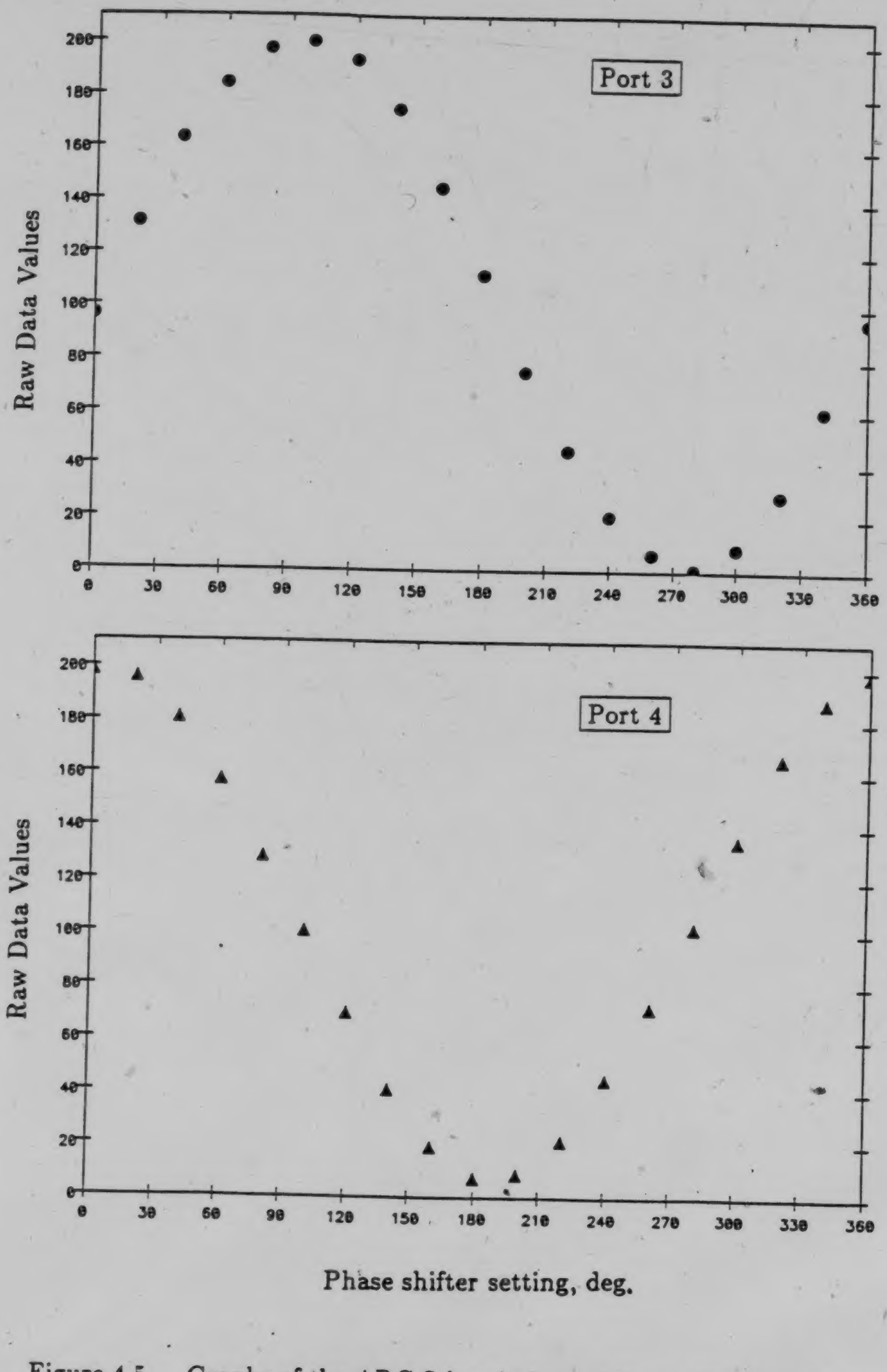

Figure 4.5 Graphs of the ARC S-band phase shifter calibration for port 3 and port 4 for 7 July 1984. Shown are the raw data values as a function of the phase shifter setting.

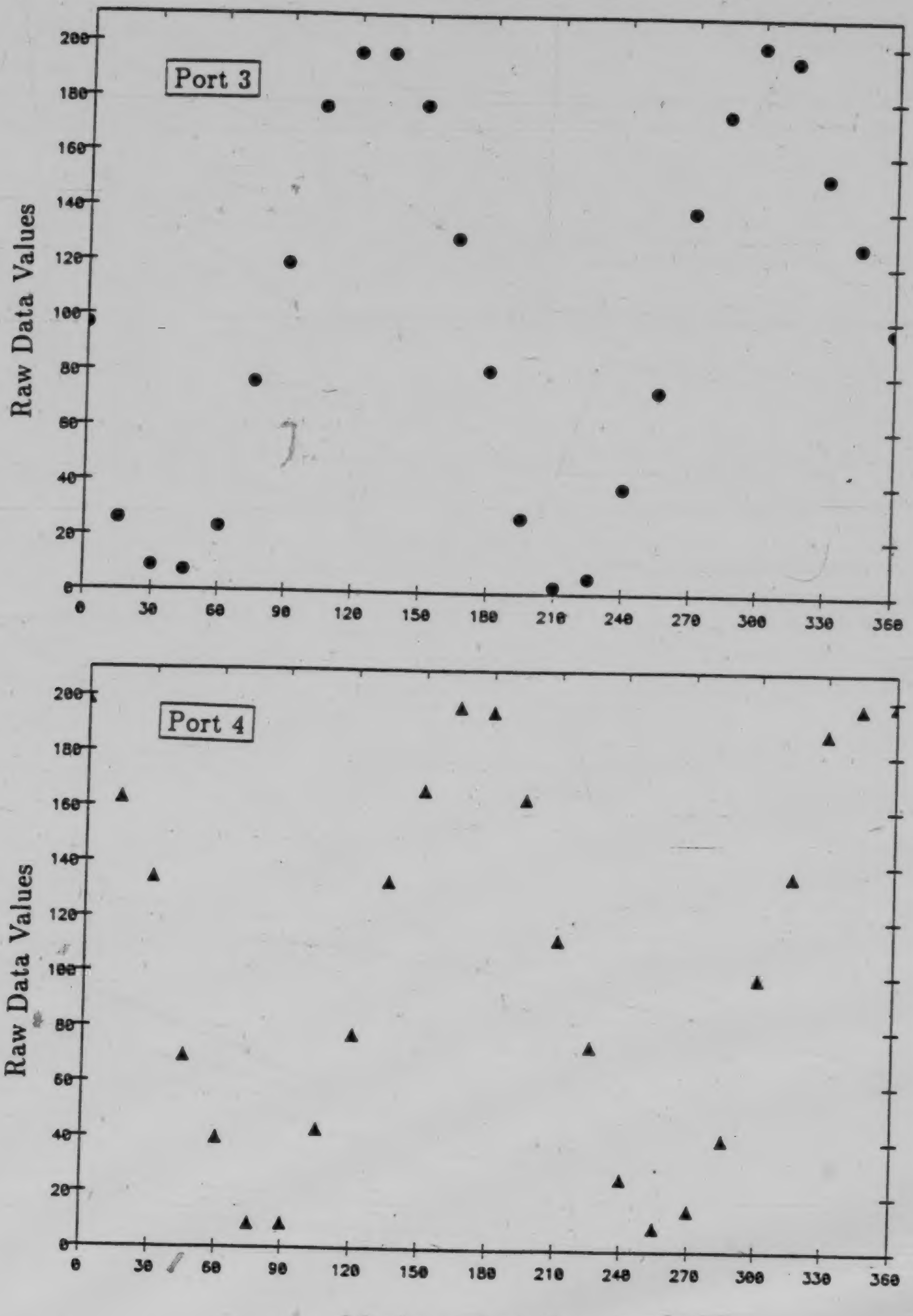

Figure 4.6 Graphs of the ARC S-band monitor calibration for port 3 and port 4 for 7 July 1984. Shown are the raw data values as a function of the monitor orientation.

linear vertical polarization is transmitted when the monitor is pointing up or down, the curves repeat themselves twice during one complete rotation of the monitor.

4.3 Analysis of Phase Discriminator Calibration Data

To assure consistency and accuracy in the analysis, it was recognized that the calibration data of port 3 and port 4 should be carefully examined. No previous investigations of these data were available. A method was developed by the author to accomplish such examinations. To describe this method, the calibration data for 7 July 1984 will be used as an illustrative example.

From Figure 4.5, it can be seen that, in general, the outputs of the phase shifter method can be expressed as

$$P_3 = JA_3\sin(\theta+\gamma_3)+C_3, \tag{4.1}$$

$$P_4 = JA_4\cos(\theta+\gamma_4)+C_4, \tag{4.2}$$

where J is related to the correlation and θ is the phase angle between the two orthogonal components of the received signal.

To determine the amplitudes (A_3 and A_4), phase offsets (γ_3 and γ_4), and zero offsets, (C_3 and C_4), a computer program was developed. This program, which is based on the least squares estimates (see Weltner *et al.*, 1986), first converts the raw data values (RDV) into computer values (CV) in the same range as the recorded real data of port 3 and port 4 (between -64 and 64) and then determines the best-fit curves for the two ports. The numerical algorithm and listing of the computer program are given in Appendix A. For the case of 7 July 1984, the best-fit curves are shown in Figure 4.7. The corresponding equations are

$$P_3 = 62.82J\sin(\theta - 4.69) + 0.06, \tag{4.3}$$

$$P_4 = 59.33J\cos(\theta - 8.27) - 0.09. \tag{4.4}$$

To establish the relationship between the phase shift and the orientation of a dipole scatterer, the monitor calibration curves are required. By convention, the orientation of the dipole scatterer, α', is defined by the angle of the minor axis with respect to the vertical (see Figure 4.8). The relationship between α' and the monitor orientation, α'', is given in Table 4.2. Using this relationship and the data of Figure 4.6, it can be shown that the outputs of the monitor rotation curves for 7 July 1984 can be expressed as

$$P_3 = JA_3\sin(2\alpha' + \gamma_3') + C_3, \tag{4.5}$$

$$P_4 = -JA_4\cos(2\alpha' + \gamma_4') + C_4. \tag{4.6}$$

Substituting for the amplitudes (A_3 and A_4) and the zero offsets (C_3 and C_4) from the phase shifter method gives

$$P_3 = 62.82J\sin(2\alpha' + \gamma_3') + 0.06, \tag{4.7}$$

$$P_4 = -59.33J\cos(2\alpha' + \gamma_4') - 0.09. \tag{4.8}$$

When the phase shifter is set at 0° ($\theta = 0^o$) and the monitor is pointing up ($\alpha' = -\frac{\pi}{2}$), the outputs of the phase shifter method must be equal to the outputs of the monitor rotation method. In other words, equation (4.1) must be equal to equation (4.5) and equation (4.2) to equation (4.6), Hence

$$\gamma_i' = -\gamma_i \qquad i = 3, 4, \tag{4.9}$$

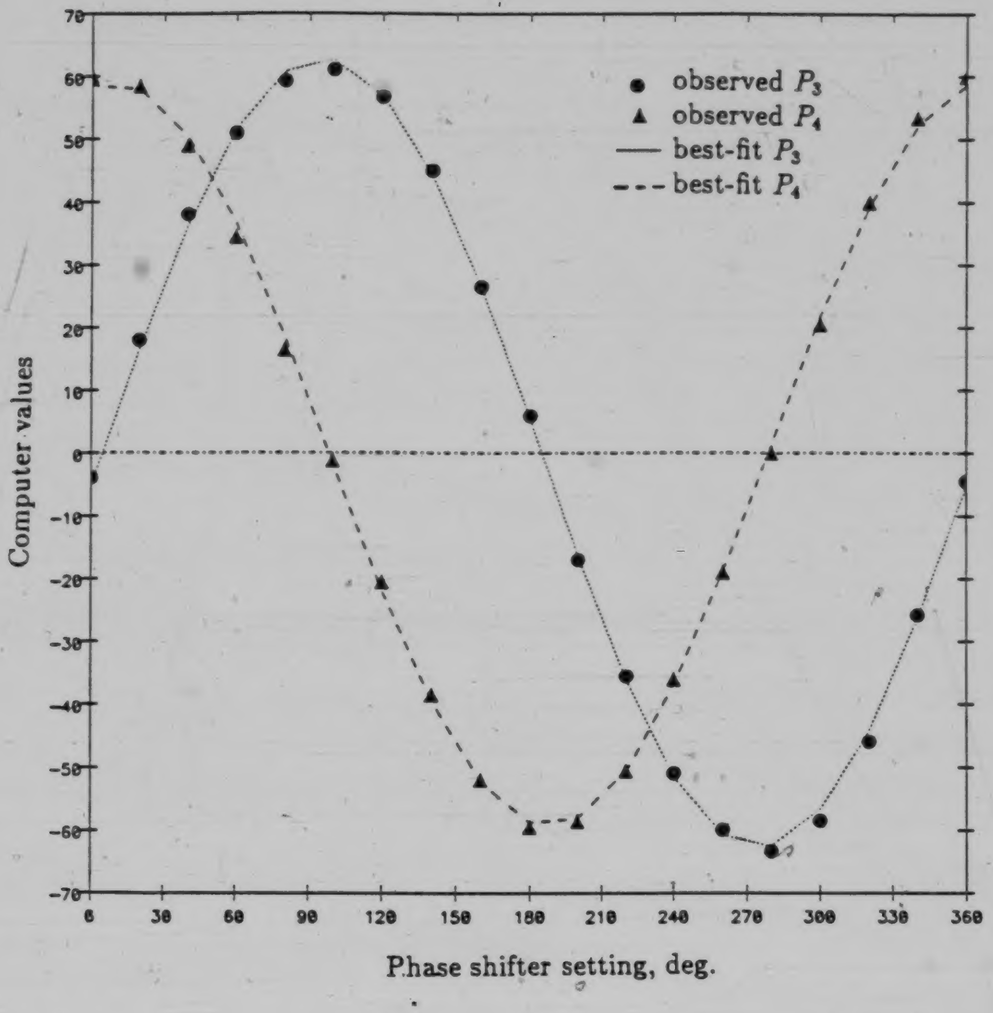

Figure 4.7 Best-fit curves for the ARC S-band phase shifter calibration data for port 3 and port 4 for 7 July 1984.

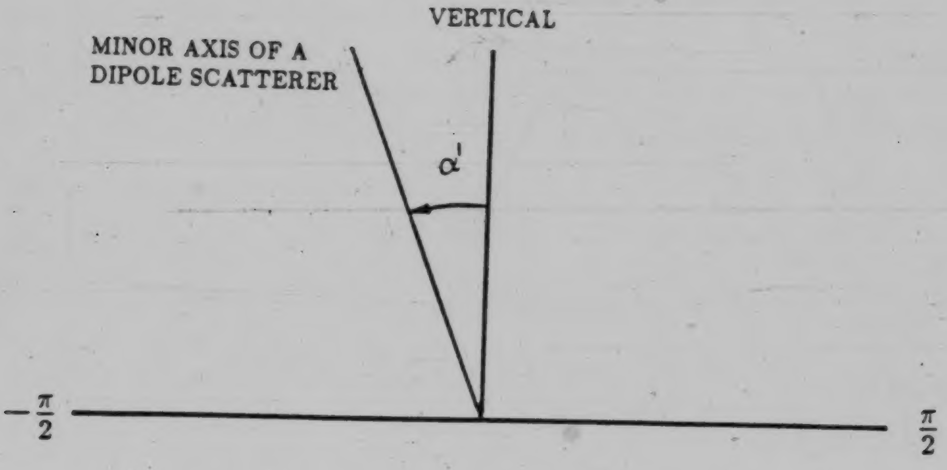
VERTICAL
MINOR AXIS OF A DIPOLE SCATTERER
α'
$-\frac{\pi}{2}$
$\frac{\pi}{2}$

Figure 4.8 The orientation of a dipole scatterer, α', with respect to the vertical as viewed by the radar.

Table 4.2 Relationship between orientation of a dipole scatterer α' and the monitor orientation α'' as viewed from the radar site.

Monitor position	Recorded orientation (deg)	α'' (deg.)	α' (deg.)
↕	0	0	± 90
⤢	45	45	−45
↔	90	±90	0
⤡	135	−45	45
↕	180	0	±90
⤢	225	45	−45
↔	270	±90	0
⤡	315	−45	45
↕	360	0	±90

or

$$\gamma_i' = \gamma_i + \pi \qquad i = 3, 4. \tag{4.10}$$

The proper selection of γ_i' is made based on the monitor rotation curves. This is carried out by a computer program which compares the monitor calibration data with the curves obtained using both possibilities of γ_i' and chooses that which minimizes the mean square error. A listing of the program is given in Appendix A. For the case of 7 July 1984, it was found that $\gamma_3' = -\gamma_3 = 4.69$ and $\gamma_4' = -\gamma_4 = 8.27$ so that

$$P_3 = 62.82J\sin(2\alpha' + 4.69) + 0.06, \tag{4.11}$$

$$P_4 = -59.33J\cos(2\alpha' + 8.27) - 0.09. \tag{4.12}$$

The comparison of the observed monitor calibration data and the curves obtained using equations (4.11) and (4.12) is shown in Figure 4.9. Note that only half a cycle is required, since the monitor rotation curves repeat themselves twice during one complete rotation. The monitor data appear to be shifted from the curves. This is because the monitor was rotated according to time which corresponded to a rotation through some angle. This resulted in only approximate positioning of the monitor.

Having determined the calibration constants A_3, A_4, C_3, C_4, γ_3', and γ_4', one now can determine J and α' using the real recorded data of port 3 and port 4.

To examine the consistency of the calibration data of port 3 and port 4, the above procedures were applied to several calibration data sets recorded throughout the summers of 1982 to 1985. The selection of the data was based on the availability of

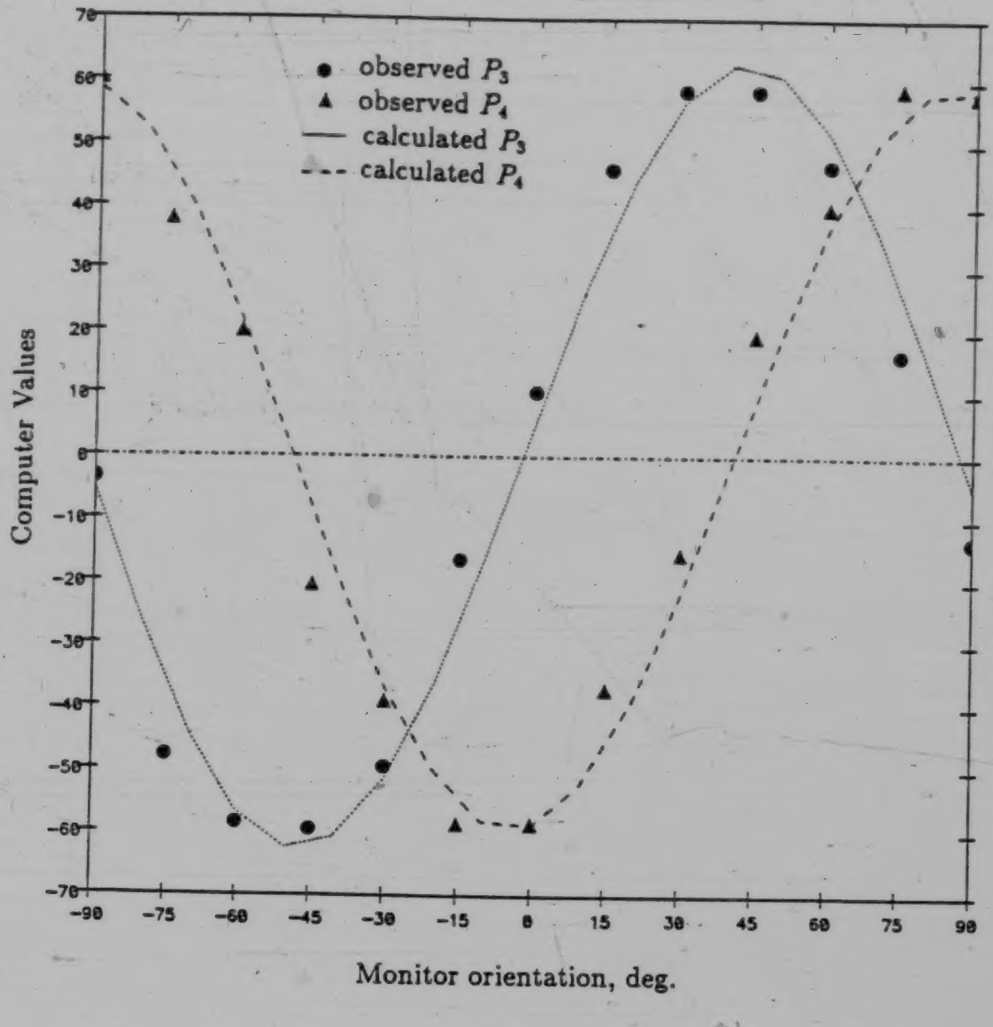

Figure 4.9 Comparison of the ARC S-band monitor calibration data for port 3 and port 4 for 7 July 1984 to the monitor curves obtained from equations (4.11) and (4.12) (see text for discussion).

the monitor calibrations. It was found that port 3 and port 4 have slightly different gain and phase characteristics and that differences between successive calibrations were not significant. The difference between γ_3' and γ_4' is typically less than 4°. As an example, Table 4.3 presents the calibration analysis for several data sets collected during the summer of 1983.

4.4 Data Processing

Four parameters can be derived from the data of the four ports: namely the equivalent reflectivity factor (Z_e), the circular depolarization ratio (CDR), the degree of correlation ($ORTT$), and the orientation angle (ALD). The calculation of Z_e and CDR requires the power levels of port 1 and port 2. By applying the major calibration data to the recorded raw data values of port 1 and port 2, CDR (in dB) is calculated from

$$CDR = P_1 - P_2, \tag{4.13}$$

where P_1 and P_2 are the power levels of port 1 and port 2 (in dBm). The value of Z_e (in dBz) is calculated from the following form of the radar equation (Battan, 1973)

$$Z_e = 10\log_{10} K_z + 20\log_{10} r + P_2, \tag{4.14}$$

where r is the range (in km) and P_2 is the power level of port 2 (in dBm). The radar constant K_z is determined for each day during time of operation and included in the major calibration files stored in the computer.

The extraction of $ORTT$ and ALD requires the phase discriminator calibration data. As discussed in the previous section, the outputs of port 3 and port 4 are

Table 4.3 Analysis of phase calibration data collected during 1983

$$\begin{aligned} P_3 &= JA_3\sin(2\alpha' + \gamma_3') + C_3 \\ P_4 &= JA_4\cos(2\alpha' + \gamma_4') + C_4 \end{aligned}$$

Date	A_3	C_3	γ_3' (deg.)	A_4	C_4	γ_4' (deg.)	$\lvert\gamma_3' - \gamma_4'\rvert$ (deg.)
20 05 1983	60.96	-2.28	-9.77	-57.22	-8.59	-5.83	3.94
31 05 1983	60.75	-2.33	-9.20	-57.00	-8.25	-5.23	3.97
23 06 1983	61.15	1.73	-8.27	-57.69	-1.28	-4.39	3.88
08 07 1983	61.23	0.29	-8.60	-57.38	0.19	-4.69	3.91
12 07 1983	61.44	-0.04	-6.41	-57.55	-0.02	-2.66	3.75
24 07 1983	61.12	1.35	-7.31	-57.42	1.29	-3.51	3.80
28 07 1983	61.00	3.00	-6.94	-57.38	1.43	-3.11	3.83
01 08 1983	60.03	3.70	-6.86	-56.81	1.11	-3.07	3.79
04 08 1983	61.03	3.60	-6.89	-57.39	1.57	-3.06	3.83
15 08 1983	60.92	-0.70	-7.10	-57.05	-1.60	-3.12	3.98

related to the correlation, J, and orientation angle α', by

$$P_3 = JA_3 \sin(2\alpha' + \gamma'_3) + C_3, \tag{4.15}$$

$$P_4 = JA_4 \cos(2\alpha' + \gamma'_4) + C_4. \tag{4.16}$$

To solve for J and α', equations (4.15) and (4.16) may be rewritten in the following matrix form

$$\begin{pmatrix} J\sin 2\alpha' \\ J\cos 2\alpha' \end{pmatrix} = \begin{pmatrix} \cos\gamma'_3 & -\sin\gamma'_4 \\ \sin\gamma'_3 & \cos\gamma'_4 \end{pmatrix} \begin{pmatrix} (P_3 - C_3)/A_3 \\ (P_4 - C_4)/A_4 \end{pmatrix}, \tag{4.17}$$

so that

$$J\sin 2\alpha' = D_3\cos\gamma'_3 - D_4\sin\gamma'_4, \tag{4.18}$$

$$J\cos 2\alpha' = D_3\sin\gamma'_3 + D_4\cos\gamma'_4, \tag{4.19}$$

where

$$D_3 = (P_3 - C_3)/A_3, \tag{4.20}$$

$$D_4 = (P_4 - C_4)/A_4. \tag{4.21}$$

Finally

$$\alpha' \equiv ALD = \frac{1}{2}\arctan\left(\frac{D_3\cos\gamma'_3 - D_4\sin\gamma'_4}{D_3\sin\gamma'_3 + D_4\cos\gamma'_4}\right), \tag{4.22}$$

$$J = \left[(D_3\cos\gamma'_3 - D_4\sin\gamma'_4)^2 + (D_3\sin\gamma'_3 + D_4\cos\gamma'_4)^2\right]^{\frac{1}{2}}. \tag{4.23}$$

As defined by McCormick and Hendry (1979), J is related to $ORTT$ by

$$J = \frac{1}{ORTT}[E(ORTT^2) - (1 - ORTT^2)K(ORTT^2)], \tag{4.24}$$

where K and E are the complete elliptic integrals of the first and second kinds.

$$E(x^2) = \int_0^{\frac{\pi}{2}} \sqrt{1 - x^2 \sin^2 y}\,dy, \tag{4.25}$$

$$K(x^2) = \int_0^{\frac{\pi}{2}} \frac{1}{\sqrt{1 - x^2 \sin^2 y}}\,dy. \tag{4.26}$$

A table of values of J and the corresponding values of $ORTT$ has been computed using IBM subroutine DCEL2 for complete elliptic integrals. These values are stored in a look-up table. A listing of the Fortran program is given in Appendix B. Figure 4.10 shows the variation of $ORTT$ with J.

The ARC radar software system provides for extraction of a complete radar cycle from which a Plan-Position-Indicator PPI map for a given elevation angle can be generated. The PPI map is divided into 90 slices (see Figure 4.11) so that radar data for any particular location within the map can be extracted. For example, slices # 8 and 9 contain data for 24° to 48° azimuth and 31.0 to 81.4 km range. For any given azimuth, a Range-Height-Indicator RHI can be generated from a set of PPI maps.

4.5 Surface Observations of Precipitation

During each summer of operation, qualitative surface measurements of precipitation were made by trained observers in radio-equipped ground vehicles which were directed underneath the high reflectivity zones of severe storms. One of the primary objectives of this program was to collect sequential time-resolved hailstone samples and rainfall measurements so that a relationship between the type of precipitation and values of the radar parameters could be established. Figure 4.12 shows an

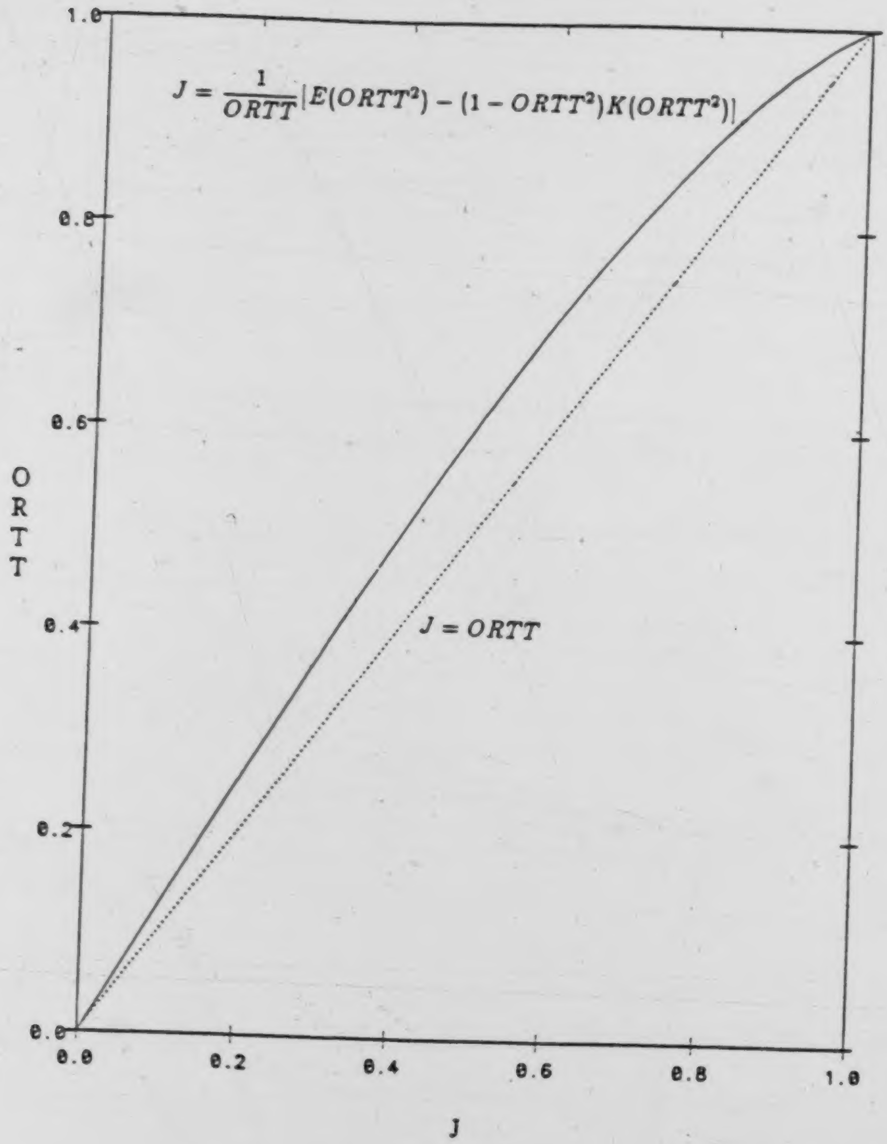

Figure 4.10 Plot of ORTT versus J.

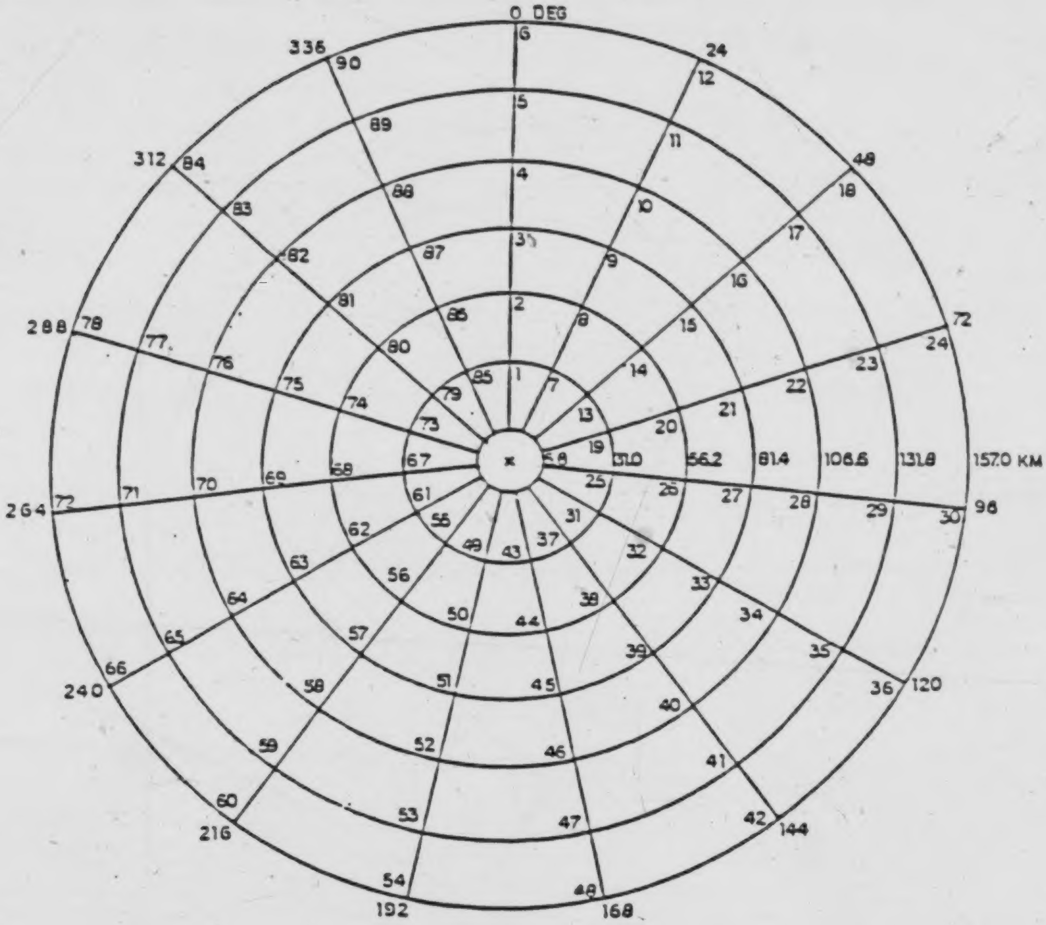
0 DEG
24
48
72
96
120
144
168
192
216
240
264
288
312
336
5.8
31.0
56.2
81.4
106.6
131.8
157.0 KM
1
2
3
4
5
6
7
8
9
10
11
12
13
14
15
16
17
18
19
20
21
22
23
24
25
26
27
28
29
30
31
32
33
34
35
36
37
38
39
40
41
42
43
44
45
46
47
48
49
50
51
52
53
54
55
56
57
58
59
60
61
62
63
64
65
66
67
68
69
70
71
72
73
74
75
76
77
78
79
80
81
82
83
84
85
86
87
88
89
90

Figure 4.11 Standard scan of the ARC radar PPI display. The map is divided into 90 slices so that radar data can be extracted for any particular location within the map. The radar location is at the center of the map.

Date: 15 August 1983
Location: NE 23 35 25 5 (34 km range and 121° azimuth)

Rain Observations

Start Time	End Time	Duration (sec)	Rainfall Rate (mm/hr)
16:16:00	16:16:30	30	45.6
16:16:30	16:17:00	30	18.0
16:17:00	16:18:00	60	47.4
16:18:00	16:18:30	30	72.0
16:18:30	16:19:00	30	194.4
16:19:00	16:20:00	60	74.4

Hail Observations

Start Time	End Time	Duration (sec)	Maximum Size (mm)	Total Stones
16:18:00	16:18:30	30	12	36
16:18:30	16:19:00	30	14	53
16:19:00	16:19:30	30	13	27
16:19:30	16:20:00	30	12	21

Figure 4.12 An example of time resolved observations of rain and hail collected by the storm chase crew. Shown are data collected on 15 August 1983 at 34 km range and 121° azimuth from the radar site.

example of rain and hail observations collected by the storm chase crew on 15 August 1983. To supplement the samples obtained from the chase vehicles, a network of 653 volunteer stations (within 13,400 km^2 surroundings Red Deer) was established during each summer of operation to collect time-integrated hail samples. The samples were picked up from the volunteers by the chase crew on no hail days. In addition, telephone surveys were conducted and hail reporting cards were mailed to 71,946 farms in Alberta; 19,464 of these were inside the project area. The hail card format is shown in Figure 4.13. These surface reports were coded and stored in the computer. Figure 4.14 shows the reports for 15 August 1983 between 1600 and 1700 MDT. The coding sheet for these reports is presented in Figure 4.15.

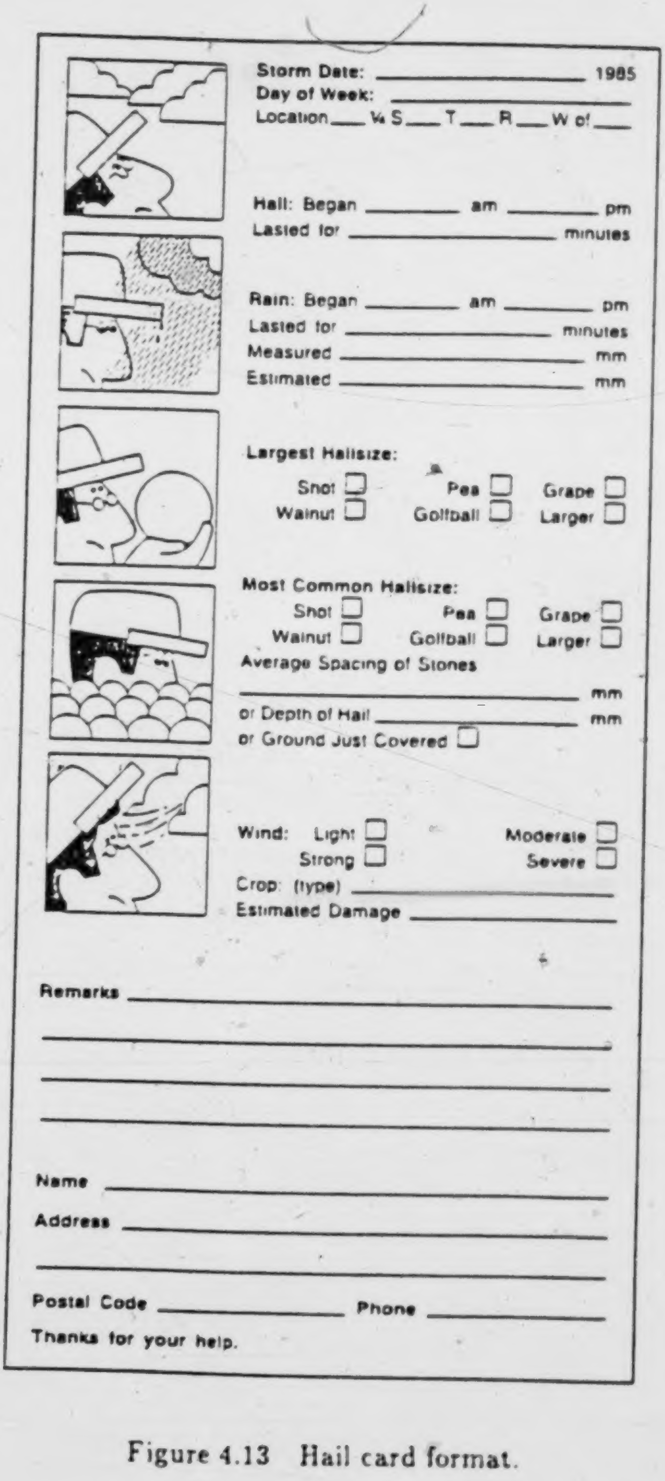

Storm Date: ____________ 1985
Day of Week: ____________
Location___ ¼ S___ T___ R___ W of___

Hail: Began ________ am ________ pm
Lasted for ________________ minutes

Rain: Began ________ am ________ pm
Lasted for ________________ minutes
Measured ________________ mm
Estimated ________________ mm

Largest Hailsize:
Shot ☐ Pea ☐ Grape ☐
Walnut ☐ Golfball ☐ Larger ☐

Most Common Hailsize:
Shot ☐ Pea ☐ Grape ☐
Walnut ☐ Golfball ☐ Larger ☐
Average Spacing of Stones
________________ mm
or Depth of Hail ________________ mm
or Ground Just Covered ☐

Wind: Light ☐ Moderate ☐
Strong ☐ Severe ☐
Crop: (type) ________________
Estimated Damage ________________

Remarks ________________________________
____
____
____

Name ________________________________
Address ________________________________
____
Postal Code ____________ **Phone** ____________
Thanks for your help.

Figure 4.13 Hail card format.

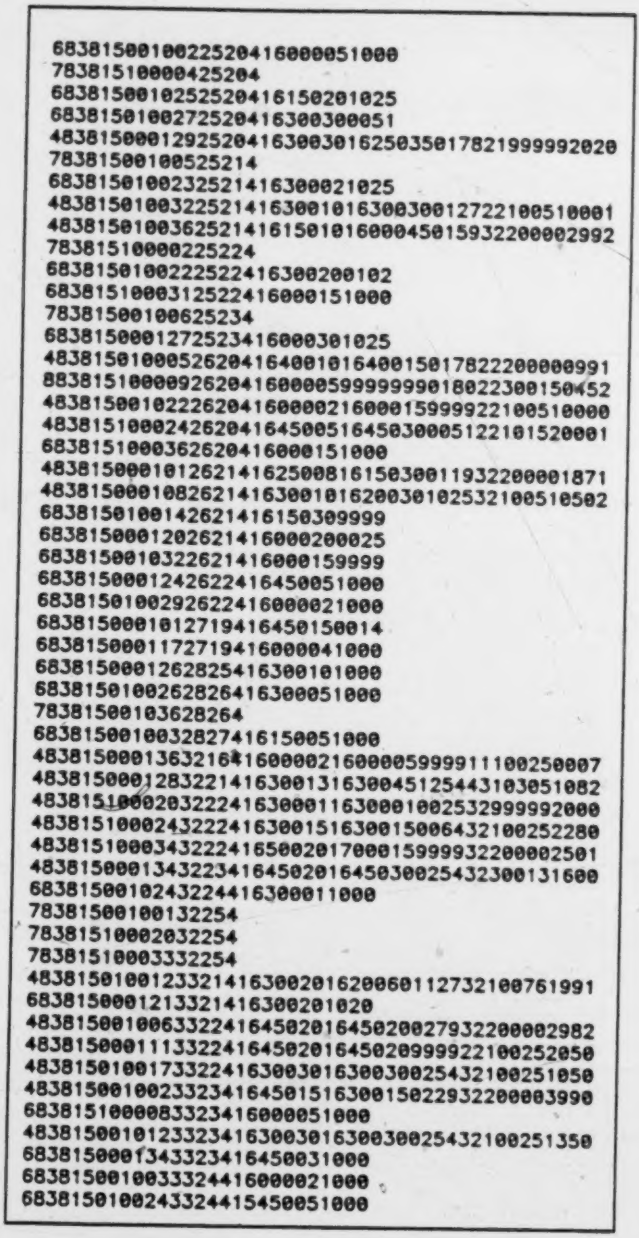

```
683815001002252041600000051000
78381510000425204
683815001025252041615020102 5
683815010027252041630030005 1
48381500012925204163003016250350178219999202 0
78381500100525214
683815010023252141630002102 5
48381501003225214163001016300300127221005100 01
48381501003625214161501016000450159322000029 92
78381510000225224
683815010022252241630020010 2
683815100031252241600015100 0
78381500100625234
683815000127252341600030102 5
48381501000526204164001016400150178222000009 91
88381510000926204160000599999990180223001504 52
48381500102226204160000216000159999221005100 00
48381510002426204164500516450300051221015200 01
683815100036262041600015100 0
48381500010126214162500816150300119322000018 71
48381500010826214163001016200301025321005105 02
683815010014262141615030999 9
683815000120262141600020002 5
683815001032262141600015999 9
683815000124262241645005100 0
683815010029262241600002100 0
683815000101271941645015001 4
683815000117271941600004100 0
683815000126282541630010100 0
683815010026282641630005100 0
78381500103628264
683815001003282741615005100 0
48381500013632164160000216000059999111002500 07
48381500012832214163001316300451254431030510 82
48381510002032224163000116300010025329999920 00
48381510002432224163001516300150064321002522 80
48381510003432224165002017000159999322000025 01
48381500013432234164502016450300254323001316 00
683815001024322441630001100 0
78381500100132254
78381510002032254
78381510003332254
48381501001233214163002016200601127321007619 91
683815000121332141630020102 0
48381500100633224164502016450200279322000029 82
48381500011133224164502016450209999221002520 50
48381501001733224163003016300300254321002510 50
48381500100233234164501516300150229322000039 90
683815100008332341600005100 0
48381500101233234163003016300300254321002513 50
683815000134332341645003100 0
683815001003332441600002100 0
683815010024332441545005100 0
```

Figure 4.14 An example of coded farmers' reports. Shown are reports for 15 August 1983 between 1600 and 1659 MDT.

[1] Blank
[2] TYPE OF REPORT
1 Mailed in 6 Rain only
2 Tele in 7 No hail/rain
3 Network rpts. 8 Out of proj. area
4 Tele Survey

[3]
[4] YEAR
(Last two digits of year)

[5] MONTH
4 April 8 August
5 May 9 September
6 June 0 October
7 July

[6] DAY OF MONTH
[7] (e.g. 03,14, etc.)

[8] QUARTER (8,9,10,11)
[9] (NE,SE,SW,NW)
[10] 0 - No
1 - Yes
[11] 9999 Missing

[12] SECTION
[13] 01 - 36

[14] TOWNSHIP
[15] 01 - 99

[16] RANGE
[17] 01 - 30

[18] MERIDIAN
4,5 or 6

[19] TIME OF HAIL - MDT
[20] 0000-2359
[21] Noon - 1200
[22] Midnight - 0000

[23] DURATION - Minutes
[24] 000-998
[25] 999 - missing
1/2 min. - 001

[26] TIME OF RAIN - MDT
[27]
[28] Same as hail
[29] 8888 - No Rain

[30] DURATION - MINUTES
[31]
[32] Same as Hail
999 Missing or No Rain
[33] MEASURED ESTIMTED MISSING
0 1 9

[34] RAINFALL EXAMPLE
[35] 000 - Trace 12.2-122
[36] 001 - 998 mm 1.2-012
998 - Not mentioned .2-002

HAIL SIZE
1 shot
2 pea
3 grape
4 walnut
5 golfball
6 larger
9 missing
[37] Maximum Size
[38] Common Size

[39] HAIL SPACING OR DEPTH
(Largest Stones)
1 Spacing
2 Just covered
3 Depth
9 Missing or Melted

[40] ACTUAL SPACING OR DEPTH
Spacing in mm or depth
[41] 9998 if greater than 9999mm
2.5mm-0003
25.4mm-0025
[42] 2544mm-0254
[43] 2544.4-2544
00-Just Covered

[44] HAIL SPACING OR DEPTH
1 Spacing
2 Just Covered
3 Depth
9 Missing or Melted

[45] ACTUAL SPACING OR DEPTH
Spacing in mm or depth in mm.
[46]
[47] 9998 if 9999 mm or more
[48] 00 - Just Covered

[49] SOFT HAIL
0-No 1-Yes 9-Missing

% of soft hail
99 Missing or hard hail
[50] 01-98% of soft stones
[51] 00-100% soft stones

[52] SHAPE OF LARGEST STONES
1 conical 4 round
2 flattened 8 others
3 egg 9 missing

[53] SURFACE TEXTURE
1 smooth 8 others
2 raspberry 9 missing
3 knobby

[54] WINDS
0 light (0 - 15 km/h)
1 moderate(15 - 40 km/h)
2 strong (40 - 65 km/h)
3 severe (over 65 km/h)
9 missing or gusty

[55] LIGHTINING
0-No 1-Yes 9-Don't know

[56] DAMAGE PERCENTAGE
00 - 97
[57] 98 code 100%
99 missing

[58] CROP TYPES
0 mixed grain 5 rapseed
1 wheat 6 garden
2 barley 7 rye
3 oats 8 other
4 hay 9 missing

[59] GROWTH STAGE
1 3-5 leaf 5 dough
2 shot blade 6 mature
3 heading 9 missing
4 blooming
[60] STORM APROACH DIRECTION
1-N 4-SE 7-W
2-NE 5-S 8-NW
3-E 6-SW 9-MISSING

Figure 4.15 Coding sheet for farmers' reports. [ ] represents columns. If only rain is observed (6 in column 2) columns 19-25 are used for rain time and duration.

CHAPTER V

Propagation Effects

5.1 Introduction

Propagation effects are an important factor in the use of circularly polarized radar for meteorological measurements. These effects usually occur when moderate to heavy rain fills a long path between the radar and the backscatter volume of interest. Because raindrops are generally oblate spheroids in shape and tend to fall with their minor axes vertical (McCormick *et al.*, 1972; Beard and Jameson, 1983), different polarizations are affected differently. For example, when a circularly polarized wave propagates through a rain medium, the vertical and horizontal components of this wave will be attenuated differently and the phase of the horizontal component will lag behind that of the vertical component. As a result, the wave will become elliptically polarized and consequently the return signal will be altered and no longer directly related to the scatterers within the volume cell under investigation. Propagation effects have been considered by Humphries (1974a), McCormick (1975), Metcalf (1981), and McGuinness *et al.* (1987). As an extension to these works, this chapter examines the relative sensitivity of the radar parameters to propagation effects and reports on tests of newly developed methods for removing these effects from the radar data. Examples of severe propagation effects selected from the ARC radar archives are also presented.

5.2 Influence of Propagation on Circularly Polarized Radar

As discussed in Chapter 3, the propagation effects are governed by equation (3.17)

$$pe^{jx} = \tanh(0.0575\Delta A + j\frac{\pi}{360}\Delta\phi), \qquad (5.1)$$

where ΔA is the differential attenuation (in dB) and $\Delta\phi$ is the differential phase shift (in degrees) between the linear vertical and horizontal components of a circularly polarized wave.

Using the Marshall and Palmer (1948) drop size distribution for raindrops with Pruppacher and Pitter (1971) shapes, Humphries (1974a) calculated ΔA and $\Delta\phi$ as a function of rainfall rate at 3 GHz. His results showed a nearly linear dependence of $\Delta A'$ (in dB/km) and $\Delta\phi'$ (in deg./km) on rainfall rate R (in mm/hr)

$$\Delta\phi' \cong 0.036R, \qquad (5.2)$$

$$\Delta A' \cong 1.2 \times 10^{-4}R, \qquad (5.3)$$

which indicate that ΔA is negligible while for intense rainfall $\Delta\phi$ is significant so that equation (5.1) reduces to

$$pe^{jx} = \tanh(j\frac{\pi}{360}\Delta\phi), \qquad (5.4)$$

which can be rewritten as

$$pe^{jx} = j\tan(\frac{\pi}{360}\Delta\phi). \qquad (5.5)$$

To illustrate how propagation through rain can affect the radar measurements, recall equations (3.46) through (3.48)

$$W_1 = < R_1 R_1^* >, \tag{5.6}$$

$$W_2 = < R_2 R_2^* >, \tag{5.7}$$

$$W = W_3 + jW_4 = < R_1 R_2^* >, \tag{5.8}$$

where W_1, W_2, W_3, and W_4 are the radar observables. The received wave amplitudes R_1 and R_2, as defined by equations (3.43) and (3.44), are

$$R_1 = C\sigma^{\frac{1}{2}}\xi^{\pm}, \tag{5.9}$$

$$R_2 = C\sigma^{\frac{1}{2}}\xi^{o}, \tag{5.10}$$

C is a constant and σ is the target backscatter cross section. ξ^o and $\xi^{\pm}$ are obtained from equations (3.36) and (3.37)

$$\xi^o = \frac{1 + \nu^+ pe^{j(\chi - 2\tau)} + \nu^- pe^{j(\chi + 2\tau)} + (pe^{j\chi})^2}{1 - (pe^{j\chi})^2}, \tag{5.11}$$

$$\xi^{\pm} = \frac{\nu^{\pm} + 2pe^{j(\chi \pm 2\tau)} + \nu^{\mp}[pe^{j(\chi \pm 2\tau)}]^2}{1 - (pe^{j\chi})^2}. \tag{5.12}$$

Consider a rain medium comprised of Rayleigh scatterers ($\delta = 0^o$) with orientation $\alpha = 0^o$ and assume an anistropic orientation of $\tau = 0^o$. Under these assumptions the scattering term $\nu^{\pm} = \nu e^{j(\delta \pm 2\alpha)} \rightarrow \nu$ and the propagation term $p^{j(\chi \pm 2\tau)} \rightarrow pe^{j\chi}$. Hence, equations (5.11) and (5.12) reduce to

$$\xi^o = \frac{1 + 2\nu pe^{j\chi} + (pe^{j\chi})^2}{1 - (pe^{j\chi})}, \tag{5.13}$$

$$\xi^{\pm} = \xi = \frac{\nu[1 + (pe^{j\chi})^2] + 2pe^{j\chi}}{1 - (pe^{j\chi})^2}. \tag{5.14}$$

Let

$$j\kappa = pe^{j\chi} = j\tan(\frac{\pi}{360}\Delta\phi), \tag{5.15}$$

so that

$$\xi^{o} = \frac{(1 - \kappa^2) + 2j\nu\kappa}{1 + \kappa^2}, \tag{5.16}$$

$$\xi = \frac{\nu(1 - \kappa^2) + 2j\kappa}{1 + \kappa^2}. \tag{5.17}$$

By substituting equations (5.16) and (5.17) into equations (5.9) and (5.10) and combining the results with equations (5.6) through (5.8), it can be shown that

$$\begin{aligned} Z_e(\mathrm{dB}) - [Z_e(\mathrm{dB})]_{\kappa=0} &= 10\log_{10}\frac{W_2}{(W_2)_{\kappa=0}} \\ &= 10\log_{10}\frac{(1 - \kappa)^2 + 4\nu^2\kappa^2}{(1 + \kappa^2)^2}, \end{aligned} \tag{5.18}$$

$$\begin{aligned} CDR(\mathrm{dB}) &= 10\log_{10}\frac{W_1}{W_2} \\ &= 10\log_{10}\frac{\nu^2(1 - \kappa^2)^2 + 4\kappa^2}{(1 - \kappa^2)^2 + 4\nu^2\kappa^2}. \end{aligned} \tag{5.19}$$

$$\begin{aligned} ALD &= \frac{1}{2}\Phi_c = \frac{1}{2}\arctan\frac{W_4}{W_3} \\ &= \frac{1}{2}\arctan\frac{2\kappa(1 - \kappa^2)[1 - (\rho_o\nu)^2]}{\rho_o\nu[4\kappa^2 + (1 - \kappa^2)^2]}. \end{aligned} \tag{5.20}$$

$$\begin{aligned} ORTT &= \frac{|W|}{\sqrt{W_1 W_2}} \\ &= \frac{\left|\rho_\alpha \bar{\nu}[4\kappa^2 + (1-\kappa^2)^2] + 2j\kappa(1-\kappa^2)[1-(\rho_\alpha\bar{\nu})^2]\right|}{\left\{\overline{\nu^2[16\kappa^4 + (1-\kappa^2)^4] + 4\kappa^2(1-\kappa^2)^2(1+\nu^4)}\right\}^{\frac{1}{2}}}, \end{aligned} \tag{5.21}$$

where ρ_α, as defined in Section 3.6, is the degree of orientation of the scatterers within the radar volume cell.

Now consider the situation where an unobstructed view exists between the radar and the volume cell of interest. In this case, $\Delta\phi = 0^o$ and the propagation term κ can be dropped from the equations above. The resulting approximations are

$$Z_e(\text{dB}) = [Z_e(\text{dB})]_{\kappa=0}, \tag{5.22}$$

$$CDR(\text{dB}) = 10\log_{10}\overline{\nu^2}, \tag{5.23}$$

$$ALD = 0^o, \tag{5.24}$$

$$ORTT = \frac{\rho_\alpha\bar{\nu}}{(\overline{\nu^2})^{\frac{1}{2}}}, \tag{5.25}$$

which provide information about the scattering properties of the particles within the observed volume cell.

When the radar beam passes through a considerable pathlength of heavy rain before reaching an area of light rain, the propagation term dominates the scattering term. In such case, the scattering term may be neglected so that equations (5.18) through (5.21) can be approximated to

$$Z_e(\text{dB}) - [Z_e(\text{dB})]_{\kappa=0} = 10\log_{10}\frac{(1-\kappa^2)^2}{(1+\kappa^2)^2}, \tag{5.26}$$

$$CDR(\text{dB}) = 10\log_{10}\frac{4\kappa^2}{(1-\kappa^2)^2}, \tag{5.27}$$

$$ALD = 45^\circ, \tag{5.28}$$

$$ORTT = 1, \tag{5.29}$$

which indicate that the radar parameters are no longer related to the properties of the scatterers in the target volume. Note that 1) when propagation effects dominate the signal, ALD and $ORTT$ reach their saturation values of 45° and 1 (or 100%) respectively; 2) If the propagation effects are such that the received signal becomes linearly polarized, i.e, $\Delta\Phi = 45^o$ ($\kappa = 0.4142$), equations (5.26) and (5.27) imply that $Z_e - (Z_e)_{\kappa=0} = 10\log(0.5) = -3$ dB and $CDR = 10\log_{10}(1) = 0$ dB. In other words, the main component loses half of its power to the orthogonal component to provide equal returns in the two orthogonal channels.

At this point recall equation (3.82)

$$Z_{DR}^c = 10\log_{10}\frac{1+\mu}{1-\mu}, \tag{5.30}$$

where

$$\mu = \frac{2ORTT(10^{\frac{CDR}{10}})^{\frac{1}{2}}}{1+10^{\frac{CDR}{10}}}. \tag{5.31}$$

As discussed above, CDR and $ORTT$ are affected by propagation. Consequently, Z_{DR}^c is likewise affected by propagation.

To examine the relative sensitivity of the radar parameters to the propagation effects, equations (5.18) through (5.21) along with equation (5.30) were used to calculate the propagation effects on Z_e, CDR, ALD, $ORTT$, and Z_{DR}^c for a 10 km long uniform rain-filled path for a frequency of 2.88 GHz and a temperature of 10 °C. Table 5.1 presents the results for rain rates of 25, 50, 75, and 100 mm/hr.

Table 5.1 Effect of propagation on uniform rain cell along a 10 km path for rain rates of 25, 50, 75, and 100 mm/hr at a temperature of 10 °C for frequency of 2.88 GHz. The deviation from the true values at 1 km range is the result of propagation effects.

Rain rate (mm/hr)	Range (km)	Z_e (dBz)	CDR (dB)	ALD (deg.)	ORTT (%)	Z_{DR}^c (dB)
25	1	44.9	-18.2	0.0	88.1	1.9
	2	44.9	-18.2	4.1	88.3	1.9
	3	44.9	-18.0	8.0	88.9	2.0
	4	44.9	-17.6	11.7	89.8	2.0
	5	44.9	-17.2	14.9	90.7	2.2
	6	44.9	-16.7	17.8	91.8	2.3
	7	44.9	-16.2	20.3	92.8	2.5
	8	44.9	-15.7	22.5	93.6	2.7
	9	44.9	-15.1	24.4	94.4	2.9
	10	44.8	-14.5	26.0	95.1	3.1
50	1	49.1	-17.1	0.0	90.5	2.2
	2	49.1	-16.9	6.9	91.0	2.3
	3	49.1	-16.3	13.0	92.2	2.5
	4	49.1	-15.5	18.1	93.6	2.8
	5	49.0	-14.5	22.0	94.9	3.1
	6	49.0	-13.5	25.1	96.0	3.6
	7	48.9	-12.5	27.6	96.8	4.0
	8	48.9	-11.6	29.5	97.4	4.5
	9	48.8	-10.7	31.0	97.9	5.1
	10	48.8	-9.8	32.2	98.3	5.7
75	1	51.5	-16.6	0.0	91.7	2.4
	2	51.4	-16.2	9.4	92.5	2.5
	3	51.4	-15.1	17.0	94.2	2.9
	4	51.4	-13.7	22.6	95.8	3.5
	5	51.3	-12.3	26.5	97.0	4.1
	6	51.2	-11.0	29.3	97.8	4.9
	7	51.1	-9.7	31.3	98.3	5.7
	8	51.0	-8.6	32.8	98.7	6.7
	9	50.8	-7.5	34.0	99.0	7.7
	10	50.7	-6.5	34.9	99.2	8.8
100	1	53.1	-16.2	0.0	92.5	2.5
	2	53.1	-15.6	11.6	93.6	2.7
	3	53.0	-14.0	20.3	95.6	3.3
	4	52.9	-12.2	25.8	97.1	4.2
	5	52.8	-10.5	29.4	98.1	5.2
	6	52.7	-8.9	31.8	98.6	6.4
	7	52.5	-7.5	33.5	99.0	7.7
	8	52.2	-6.1	34.7	99.3	9.3
	9	52.0	-4.9	35.5	99.4	11.1
	10	51.6	-3.7	36.1	99.5	13.2

The values of the radar parameters at 1 km range correspond to the true values (values unaffected by propagation). The deviation from these values is the influence of propagation. It can be seen that: 1) propagation effects depend on the rainfall rate and the distance through the rain; 2) CDR, $ORTT$, ALD, and Z_{DR}^{c} are severely affected by propagation. For example, along a 10 km path of 50 mm/hr rain rate, CDR increased by 7.3 dB, ALD progressed from its true value of 0° to 32.2°, and $ORTT$ and Z_{DR}^{c} increased by 7.8% and 3.5 dB respectively; and 3) the effects on Z_e are only detectable at 75 mm/hr, decreasing by 0.8 dB over a 10 km path. These results are generally in agreement with the results of Humphries (1974a) and McGuinness *et al.* (1987), suggesting that the propagation effects can be assessed by examining the behavior of the radar measurements with range.

5.3 Methods of Correction for Propagation Effects

A procedure for correcting S-band circularly polarized radar measurements has recently been developed by Bebbington *et al.* (1987). This method derives corrected $Z_e, CDR, ORTT$, and Z_{DR}^{c} at any individual range bin using only parameters measured at that bin. Based on the coherency matrix, they related the radar observables W_1, W_2, and W to the degree of polarization p and the ellipticity of the scattered field β as (see Appendix C)

$$p = \left[1 - \frac{4(W_1 W_2 - |W|^2)}{(W_1 + W_2)^2}\right]^{\frac{1}{2}}, \tag{5.32}$$

$$\beta = \frac{1}{2}\arctan\frac{2|W|}{W_2 - W_1}, \tag{5.33}$$

and the radar parameters are related to p and β by

$$Z_e = 10\log_{10}\left[\frac{r^2}{2K_z}(W_1 + W_2)(1 + p\cos 2\beta)\right], \tag{5.34}$$

$$CDR = 10\log_{10}\left(\frac{1 - p\cos 2\beta}{1 + p\cos 2\beta}\right), \tag{5.35}$$

$$ORTT = \frac{|p\sin 2\beta|}{(1 - p^2\cos^2 2\beta)^{\frac{1}{2}}}, \tag{5.36}$$

$$Z_{DR}^c = 10\log_{10}\left(\frac{1 + p\sin 2\beta}{1 - p\sin 2\beta}\right), \tag{5.37}$$

where r is the range and K_z is a radar related constant.

Since the degree of polarization p is very close to unity and not materially affected by propagation (McGuinness *et al.*, 1987), one may expect that propagation effects on the radar parameters are almost wholly expressed in the behavior of β.

By using the fact that at S-band frequencies, propagation effects are entirely differential phase shift (differential attenuation is negligible) and assuming that any deviation in ALD from 0^o values can be attributed to differential phase shift, Bebbington *et al.* (1987) showed that ALD can be used to remove propagation effects on β. They derived the following relation for computing the corrected value of β, denoted by β':

$$\cos 2\beta' = (\cos^2 2\beta + \sin^2 2\beta \sin^2 2ALD)^{\frac{1}{2}}. \tag{5.38}$$

The corrected radar parameters can be derived by replacing β with β' in equations (5.34) through (5.37), i.e.,

$$Z_e' = 10\log_{10}\left[\frac{r^2}{2K_z}(W_1+W_2)(1+p\cos 2\beta')\right], \tag{5.39}$$

$$CDR' = 10\log_{10}\left(\frac{1-p\cos 2\beta'}{1+p\cos 2\beta'}\right), \tag{5.40}$$

$$ORTT' = \frac{|p\sin 2\beta'|}{(1-p^2\cos^2 2\beta')^{\frac{1}{2}}}, \tag{5.41}$$

$$Z_{DR}^{c'} = 10\log_{10}\left(\frac{1+p\sin 2\beta'}{1-p\sin 2\beta'}\right). \tag{5.42}$$

Another approach for removing the effects of propagation differential phase shift from circular polarization measurements at any given range bin was developed by Jameson and Davé (1988) (see also Jameson, 1987). This method was achieved by 1) re-expressing the circular polarization quantities in terms of linear polarization parameters, 2) identifying and removing terms which are affected by propagation differential phase shift, and 3) re-computing the circular polarization quantities from the linear polarization parameters which are not affected by propagation differential phase shift. The resulting equations for deriving corrected CDR and $ORTT$ are

$$CDR'' = 10\log_{10}\left(\frac{\varsigma+1-2\varsigma^{\frac{1}{2}}\rho_l}{\varsigma+1+2\varsigma^{\frac{1}{2}}\rho_l}\right), \tag{5.43}$$

$$ORTT'' = \frac{|\varsigma-1|}{[(1+\varsigma-2\varsigma^{\frac{1}{2}}\rho_l)(1+\varsigma+2\varsigma^{\frac{1}{2}}\rho_l)]^{\frac{1}{2}}}, \tag{5.44}$$

where ς is the differential reflectivity ($\varsigma = 10^{\frac{Z_{DR}}{10}}$) and ρ_l is the magnitude of the complex correlation v_l between the horizontally co-polarized and vertically cross polarized components

$$v_l = \rho_l e^{j\Phi_l}, \tag{5.45}$$

where Φ_l is the effective phase difference between the two orthogonal linearly polarized components.

Jameson and Davé (1988) showed that the linear polarization parameters ς and ρ_l can be derived from the circular polarization measurements through the following relations

$$\varsigma = \frac{1 + 2N^{\frac{1}{2}}}{1 - 2N^{\frac{1}{2}}}, \tag{5.46}$$

$$\rho_l = \mathrm{Re}(v_l) + \mathrm{Im}(v_l), \tag{5.47}$$

where

$$N = \frac{ORTT^2 10^{\frac{CDR}{10}}}{(1 + 10^{\frac{CDR}{10}})^2 (1 + \tan^2 \Phi_c)}, \tag{5.48}$$

$$\begin{aligned} \mathrm{Im}(v_l) &= \frac{(1 - \varsigma)\tan\Phi_c}{2\varsigma^{\frac{1}{2}}} && (5.49) \\ \mathrm{Re}(v_l) &= \frac{(\varsigma - 1) - M^{\frac{1}{2}}(\varsigma + 1)}{2(M\varsigma)^{\frac{1}{2}}}, && (5.50) \end{aligned}$$

$$M = \frac{ORTT^2 10^{\frac{CDR}{10}}}{(1 + \tan^2 \Phi_c)}. \tag{5.51}$$

Here $ORTT, CDR$, and Φ_c, which is related to ALD, represent radar measured quantities, and they are all affected by propagation as shown in Section 5.2.

It is apparent that Jameson and Davé's (1988) method does not consider the influence of propagation on Z_e. An advantage of this method is that even when circular polarization measurements are affected by propagation, they can still be transformed into corresponding linear polarization parameters which are unaffected by propagation.

As a test, the correction methods were applied to the theoretical calculations presented in Table 5.1, i.e., the values of ALD, which is related to Φ_c, were used to remove the effects of propagation on the other parameters. The results for the 100 mm/hr case are shown in Table 5.2. Corrected values should be equal to the true values at 1 km. It is apparent that for the 10 km path, Z_e and Z_{DR}^c correct very well while CDR and $ORTT$ correct within 0.3 dB and 2.7% respectively. Note that Jameson and Davé's (1988) method does not correct for Z_e. The results also show that the correction methods lead to identical results, probably because both methods assume that propagation effects are entirely due to differential phase shift (differential attenuation is negligible) and any deviation in the phase angle from 0° can be attributed to differential phase shift. In this research, we have adopted the method of Bebbington *et al.* (1987) given by equations (5.34) through (5.37)

5.4 Evidence of Propagation Effects on the ARC Radar Data

Measurements in heavy precipitation situations which exhibit prominent evidence of propagation effects will now be considered. Figure 5.1 presents a PPI map of measured $Z_e, CDR, \overline{ORTT}$, and ALD for a large storm on 31 July 1982 at 1850 MDT, at an elevation angle of 1.3°. Range rings are at 20 km intervals and azimuth

Table 5.2 Comparison between methods for correction of propagation effects. Corrected values should be equal to the true values at 1 km range.

Calculated							Correction Methods						
Effects of Propagation							Bebbington et al. (1987)				Jameson and Davé (1988)		
Rain rate (mm/hr)	Range (km)	Z_e (dBz)	CDR (dB)	ALD (deg.)	$ORTT$ (%)	Z_{DR}^c (dB)	Z_e' (dBz)	CDR' (dB)	$ORTT'$ (%)	$Z_{DR}^{c'}$ (dB)	CDR'' (dB)	$ORTT''$ (%)	$Z_{DR}^{c''}$ (dB)
100	1	53.1	-16.2	0.0	92.5	2.5	53.1	-16.2	92.5	2.5	-16.2	92.5	2.5
	2	53.1	-15.6	11.6	93.6	2.7	53.1	-16.2	92.6	2.5	-16.2	92.6	2.5
	3	53.0	-14.0	20.3	95.6	3.3	53.1	-16.3	92.7	2.5	-16.3	92.7	2.5
	4	52.9	-12.2	25.8	97.1	4.2	53.1	-16.3	93.0	2.5	-16.3	93.0	2.5
	5	52.8	-10.5	29.4	98.1	5.2	53.1	-16.3	93.3	2.5	-16.3	93.3	2.5
	6	52.7	-8.9	31.8	98.6	6.4	53.1	-16.4	93.7	2.5	-16.4	93.7	2.5
	7	52.5	-7.5	33.5	99.0	7.7	53.1	-16.4	94.1	2.5	-16.4	94.1	2.5
	8	52.2	-6.1	34.7	99.3	9.3	53.1	-16.4	94.5	2.5	-16.4	94.5	2.5
	9	52.0	-4.9	35.5	99.4	11.1	53.1	-16.5	94.9	2.5	-16.5	94.9	2.5
	10	51.6	-3.7	36.1	99.5	13.2	53.1	-16.5	95.3	2.5	-16.5	95.3	2.5

31 July 1982 1850 MDT El.=1.3°

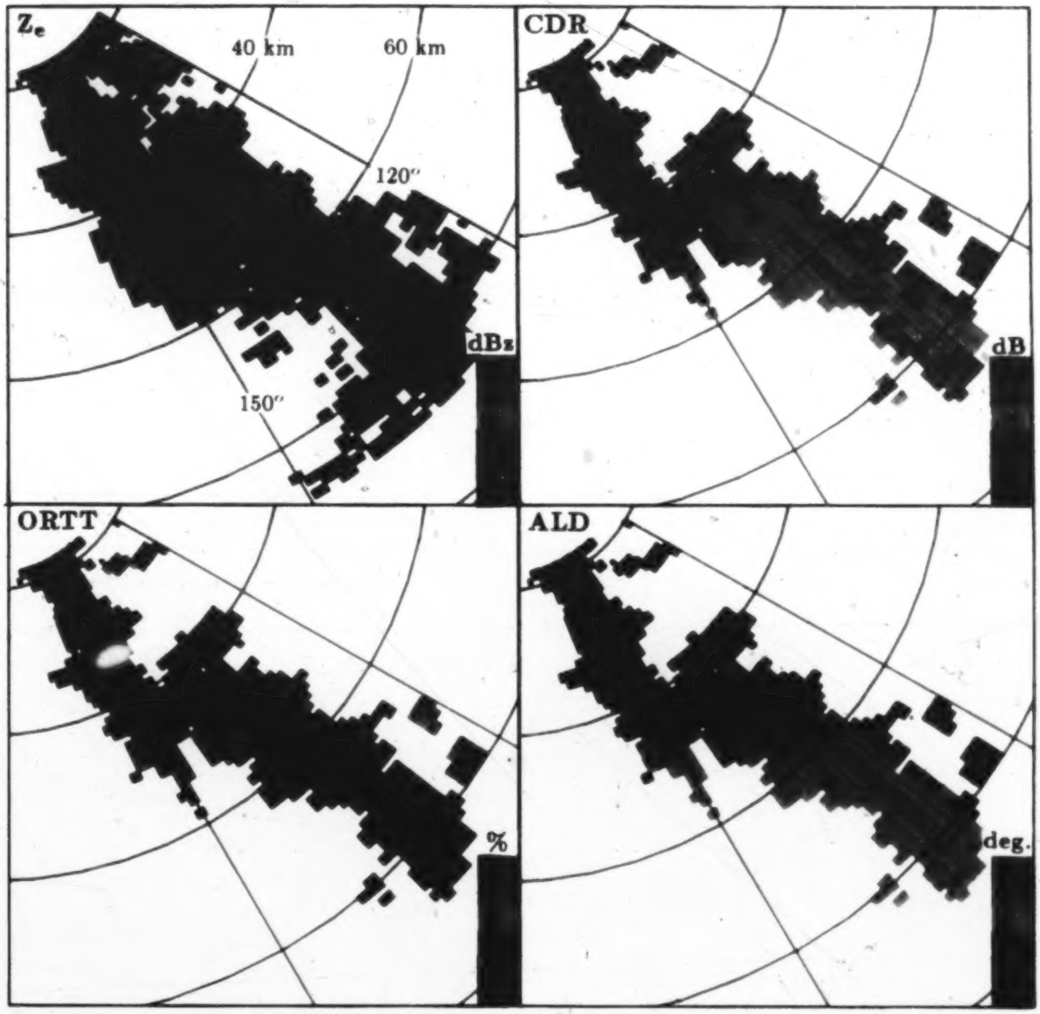
Z_e
40 km
60 km
120°
150°
dBz
CDR
dB
ORTT
%
ALD
deg.

Figure 5.1 PPI maps of Z_e, *CDR*, *ORTT*, and *ALD* for rain observations on 31 July 1982 at 1850 MDT at 1.3° elevation. Note the impact of propagation effects as *CDR* and *ALD* increased to values above -10 dB and 35° respectively at the far edge of the storm while *ORTT* remained high at values greater than 80% over the entire storm.

radials are at 30° intervals from north. No hail was observed on the ground at the locations covered by the radar echoes of Figure 5.1. Therefore the storm was assumed to be a heavy rain event.

Evidence of propagation effects on $CDR, ORTT$, and ALD resulting from the passage of the radar beam through the region of heavy rain can be seen in Figure 5.1. From the radar site outward through the storm, CDR increased from values close to -25 dB to values greater than -10 dB, $ORTT$ maintained high values (greater than 80%) over the entire storm, and ALD progressed from values near 0^o to values above 35^o. These are all indicative of propagation and consistent with the theoretical calculations of Table 5.1. Note that at the near side of the storm relative to the radar, where the propagation effects are expected to be insignificant, ALD was in the neighborhood of 0^o. This seems to be consistent with the idea that raindrops fall as oblate spheroids with their minor axes oriented vertical.

To estimate the extent of propagation effects and to see how well the correction method of Bebbington *et al.* (1987) could remove such effects from the data, a radial path through the high Z_e region was chosen. Figure 5.2 shows these results along the 135° azimuth radial which cuts through the pocket of high Z_e (greater than 60 dBz for two bins at about 50 km). The solid curves represent uncorrected values of $Z_e, CDR, ORTT, ALD$, and calculated Z_{DR}^c which were derived using McCormick's (1979) approximation (equation 3.82). The dotted curves represent the corresponding corrected values of Z_e, CDR, $ORTT$, and Z_{DR}^c. The correction method used the values of ALD to correct for Z_e, CDR, $ORTT$, and Z_{DR}^c. Again, the propagation effects on CDR and ALD are obvious, as they increased with increasing range.

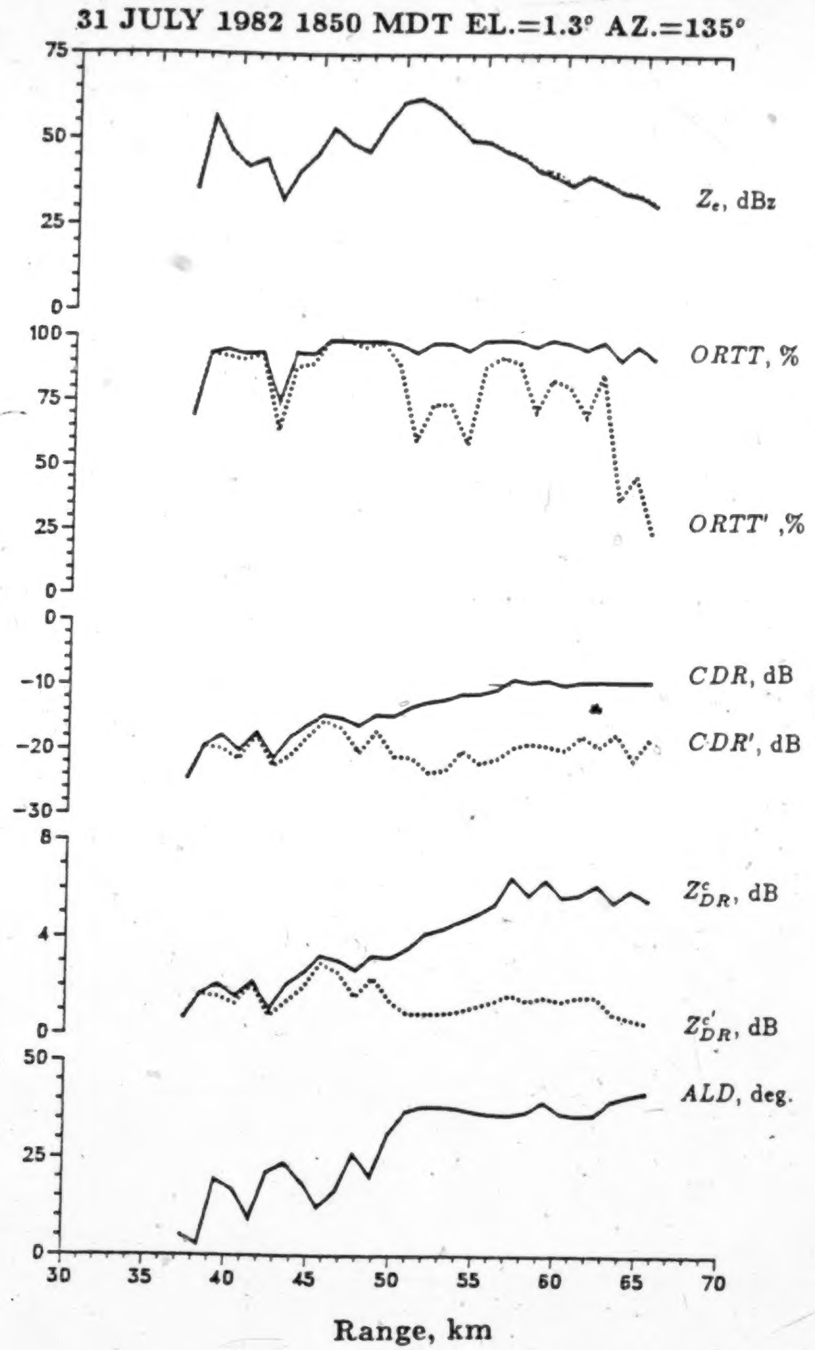

Figure 5.2 Comparison between uncorrected (solid curves) and corrected (dotted curves) radar parameters during rain observations on 31 July 1982 at 1850 MDT.

$ORTT$ was almost constant at the far edge of the storm. Consequently the values of the derived parameter, Z_{DR}^c, were likewise affected by propagation. Comparison between uncorrected and corrected values show that the corrected CDR, $ORTT$, and Z_{DR}^c were significantly improved in the sense that they were corrected towards expected values. Z_e was not greatly affected by propagation.

The corrected values of CDR, $ORTT$, and Z_{DR}^c show a good correlation with the Z_e pattern out to the 47 km range. High Z_e values (greater than 45 dBz) were associated with high $ORTT$ (greater than 80%), CDR between -21 and -17 dB, and Z_{DR}^c above 1 dB. These values are all typical of rainfall (Hendry *et al.*, 1976; Torlaschi *et al.*, 1984; Bringi *et al.*, 1984). The relatively low values of CDR, $ORTT$, and Z_{DR}^c at the region between 49 and 55 km where Z_e peaked to values greater than 60 dBz can probably be attributed to the penetration of the radar beam into a region of heavy rain mixed with ice particles which were either spherical or tumbling. The presence of such particles would act to decrease CDR,$ORTT$, and hence Z_{DR}^c relative to those received from rain only. The evidence for such situations will become more apparent in the next chapter.

Two more examples of observations and corrections along a radial will now be considered (Figures 5.3 and 5.4). Figure 5.3 presents uncorrected and corrected radar data along the 230° azimuth radial through a broad cell of heavy rain on 24 July 1983 at 2039 MDT at an elevation angle of 1.6°. The influence of propagation on CDR,$ORTT$, ALD, and Z_{DR}^c is apparent, as CDR degraded from -20 dB to -8 dB, $ORTT$ remained high (greater than 90%), ALD increased from 4° to 44°, and Z_{DR}^c increased to values near 8 dB. Near the radar, the differences between the

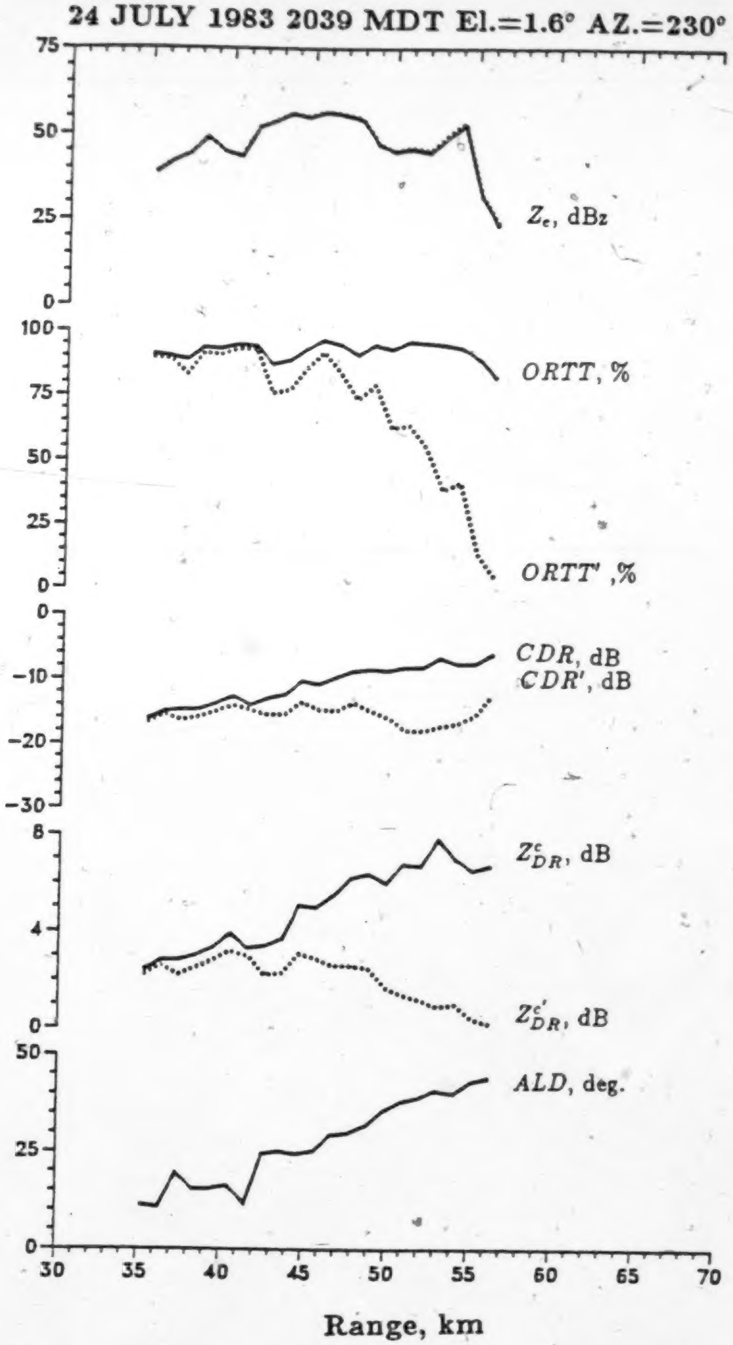

Figure 5.3 Comparison between uncorrected (solid curves) and corrected (dotted curves) radar parameters during rain observations on 24 July 1983 at 2039 MDT.

uncorrected and corrected values of CDR, $ORTT$, and Z^c_{DR} are relatively small, suggesting small propagation effects in that region. Further into the storm, the increasing differences indicate progressive propagation effects. The results also show that Z_e was not greatly affected by propagation. The corrected values of CDR, $ORTT$, and Z^c_{DR} were well correlated with the Z_e pattern. As in the previous example, the relatively low values of $CDR, ORTT$, and Z^c_{DR} between points of 52 and 54 km where Z_e values were greater than 45 dBz suggest heavy rain mixed with small hail particles. The 55 km range represents the back edge of the storm, beyond which the CDR', $ORTT'$, and $Z^{c'}_{DR}$ values should not be evaluated in terms of hail particles.

Figure 5.4 shows radar data along the 27° azimuth radial for a very strong precipitation cell of rain and hail mixture located on the near side of the storm (about 36 km from the radar site) on 5 July 1984 at 1900 MDT at an elevation angle of 1.1°. Evidence of severe propagation effects resulting from the penetration of the radar beam through a region of very heavy precipitation (Z_e greater than 60 dBz) are obvious. It can be seen that in less than 10 km, CDR jumped from -19 dB to a value close to 0 dB, $ORTT$ increased from 77% to 95%, ALD progressed from 0° to 40°, and Z^c_{DR} jumped to values near 20 dB, which are beyond the meteorological range (0 to 6 dB). As Z_e started to decrease at the 40 km point, $CDR, ORTT$, and ALD remained almost constant. These are all typical of severe propagation effects. It can also be seen that the correction method provided a very good enhancement of CDR, $ORTT$, Z^c_{DR}, and Z_e. Along the entire path, a good correlation exists between $CDR, ORTT, Z^c_{DR}$, and Z_e except at points 49, 61, and 69 km, where

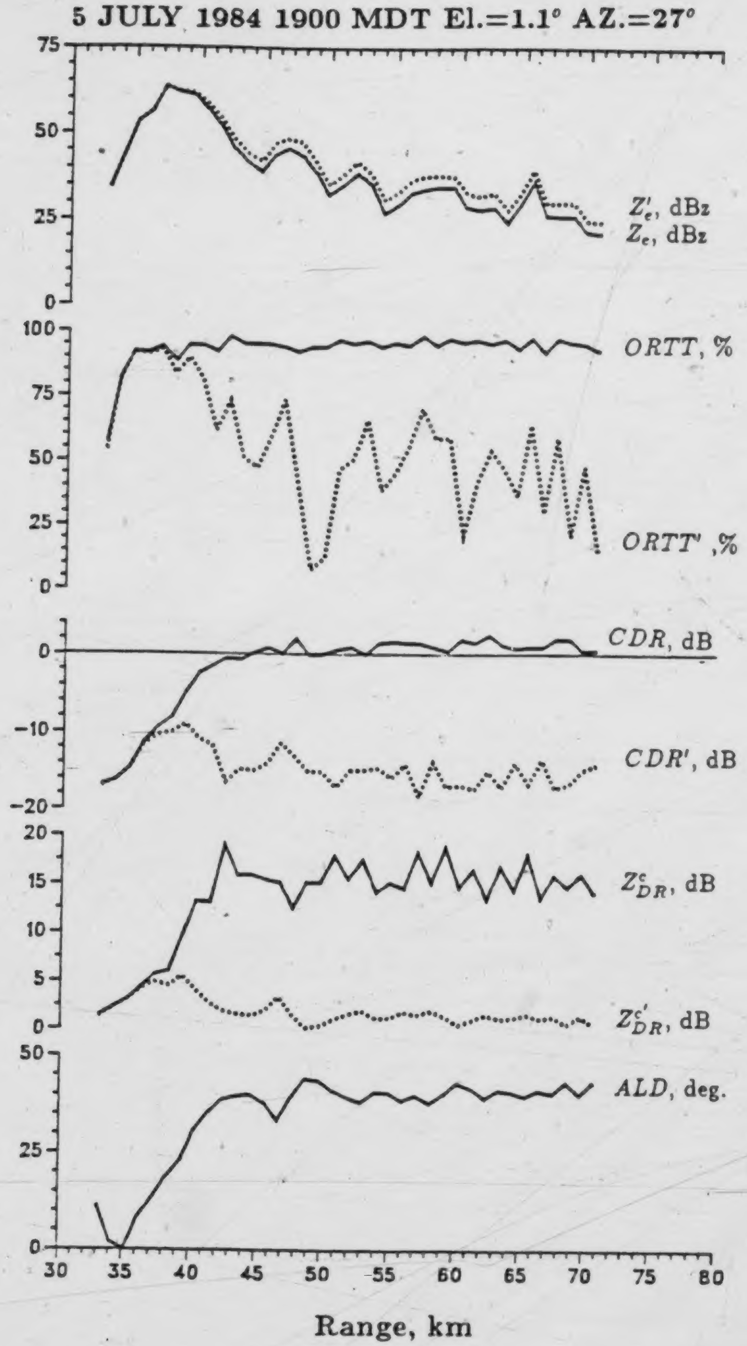

Figure 5.4 Comparison between uncorrected (solid curves) and corrected (dotted curves) radar parameters during observations of mixed rain and hail on 5 July 1984 at 1900 MDT.

corrected values of $ORTT$ dropped to very low values. This behavior was expected at points where ALD approaches the saturation value of 45°, in which case $ORTT$ and Z_{DR}^{c} approach zero values (see equations 5.38, 5.41, and 5.42). It should be noted that at the 36 km point, where the rain and hail mixture was observed at the ground level, readings of CDR, $ORTT$, and Z_{DR}^{c} were -10 dB, 95%, and 5 dB respectively. These values were extremely high for such mixture, because the presence of hail, as will be shown in the next chapter, usually results in low readings of CDR', $ORTT'$, and Z_{DR}^{c}. The only plausible explanation for this situation is that the hailstones had the shape and behavior of very large raindrops, i.e., oblate spheroids falling with their minor axes near vertical. This conclusion appears to be supported by ALD, which was close to 0^{o}.

In the three examples presented above, it can be seen that propagation effects can severely corrupt the measurements of CDR, $ORTT$, and ALD, making them larger than the intrinsic values for scattering alone. Consequently the derived parameter Z_{DR}^{c} can also be severely affected by propagation. The correction method of Bebbington *et al.* (1987) proved to be a useful means for apparently removing these propagation effects from the radar measurements and provides greater flexibility in interpreting the data. One must next compare corrected radar data to a detailed ground-based observations of precipitation to see whether radar signatures of rain and hail can be determined more clearly. This will be done in the next chapter.

CHAPTER VI

Polarization Observations of Rain and Hail

6.1 Introduction

Discrimination between rain and hail using polarization techniques is based on the differences in shape, orientation, and size distribution between raindrops and hailstones. The theoretical and experimental studies presented in Chapter II (e.g. Torlaschi *et al.*, 1984; Hendry and Antar, 1984a; Bringi *et al.*, 1984) suggested that, in general, hailstorms produce values of CDR, $ORTT$, and Z_{DR} different from those of precipitation consisting solely of rain for a given Z_e. Large raindrops, for example, are oblate and stable in their orientation (McCormick and Hendry 1970; Saunders, 1971; Beard and Jameson, 1983), thus producing values of CDR between -18 and -16 dB, $ORTT$ greater than 60%, and Z_{DR} greater than 1 dB. The irregular shapes and tumbling motions of hailstones (Roos and Carte, 1973) are expected to result in relatively lower values of CDR, $ORTT$, and Z_{DR} than those produced by rain only.

To establish the polarization signatures of rain and hail, it is necessary to compare radar measurements with the type of precipitation observed at the ground directly beneath and coincident with the radar information. This chapter presents an analysis of seven case studies ranging from a light rain-producing situation to a case of severe convection resulting in heavy rain and walnut-size hail at the ground. These cases were chosen on the basis of availability of simultaneous radar data and ground-based information. Preliminary analysis of most of these case studies was presented at the 23rd Conference on Radar Meteorology (Al-Jumily *et al.*, 1986). Several other cases were rejected because observations were taken far from the radar site. The radar in these cases was sensing precipitation at relatively high altitude and hence it was difficult to correlate the radar data with the ground measurements.

To observe precipitation as close as possible to the ground and to avoid using radar data from heights close to or above the melting level, radar measurements for an antenna elevation angle between 1° and 2° were chosen. Data for elevation scans less than 1° were not used, because the ground surface can alter and degrade the polarization properties of the received signal. Ground truth information consisted mainly of data collected by the crew of the storm chase truck. Reports of volunteer farmers were only used to indicate whether hail had fallen at particular locations during a particular time period. These farmer reports will be used again in the next chapter to carry out an analysis averaged over a whole storm passage. To account for the lag between times when precipitation was observed by the radar and when precipitation was intercepted by the storm chase vehicles, radar measurements were extracted at least three minutes prior to the end of the sampling period of the truck observations. Three minutes (the radar cycle time) is the time needed for a solid ice hailstone with an average diameter of 1 cm to fall a distance of about 3 km (drag coefficient 0.5 at air density of 1 kg m^{-3}) (Mason, 1971). The radar measurements were corrected for propagation effects using the method of Bebbington *et al.* (1987).

discussed in the previous chapter. The theoretical models of Torlaschi *et al.* (1984) are used to help interpret the radar data.

6.2 Rain Observations

8 July 1983: A rain storm developed in the late afternoon due west of the radar. Based on accumulated amounts measured at 30 s intervals, the sampling truck recorded a mean rainfall rate of 56 mm/hr between 1501 and 1509 MDT at about the 270° azimuth and 42 km range. Figure 6.1 shows the 1505 MDT, 1.7° elevation values[1] of Z_e', CDR', $ORTT'$, and $Z_{DR}^{c'}$ along a radial path which passed directly above the sampling site. It is evident that along the entire radial path, CDR',$ORTT'$, and $Z_{DR}^{c'}$ are well correlated with Z_e', indicating the presence of rain. Furthermore, the intense portion of the storm was located directly above the sampling site. At this point, Z_e' was about 48 dBz with CDR' of -18 dB, $ORTT'$ of 73%, and $Z_{DR}^{c'}$ of 1.5 dB. Based on Torlaschi *et al.*'s (1984) rain model, these observed values suggest a rainfall rate of 50 to 55 mm/hr, which is consistent with the ground-based measurements of 56 mm/hr rainfall rate.

24 July 1983: On the evening of 24 July 1983, a heavy to very heavy rainstorm was intercepted by the chase vehicle in the southwest section of the project area, approximately at the 221° azimuth and 48 km range from the radar site. Based on accumulated amounts measured at 30 s intervals, a mean rainfall rate of 77 mm/hr was measured between 2034 and 2052 MDT.

---

[1] Hereafter the prime indicates values corrected for propagation effects.

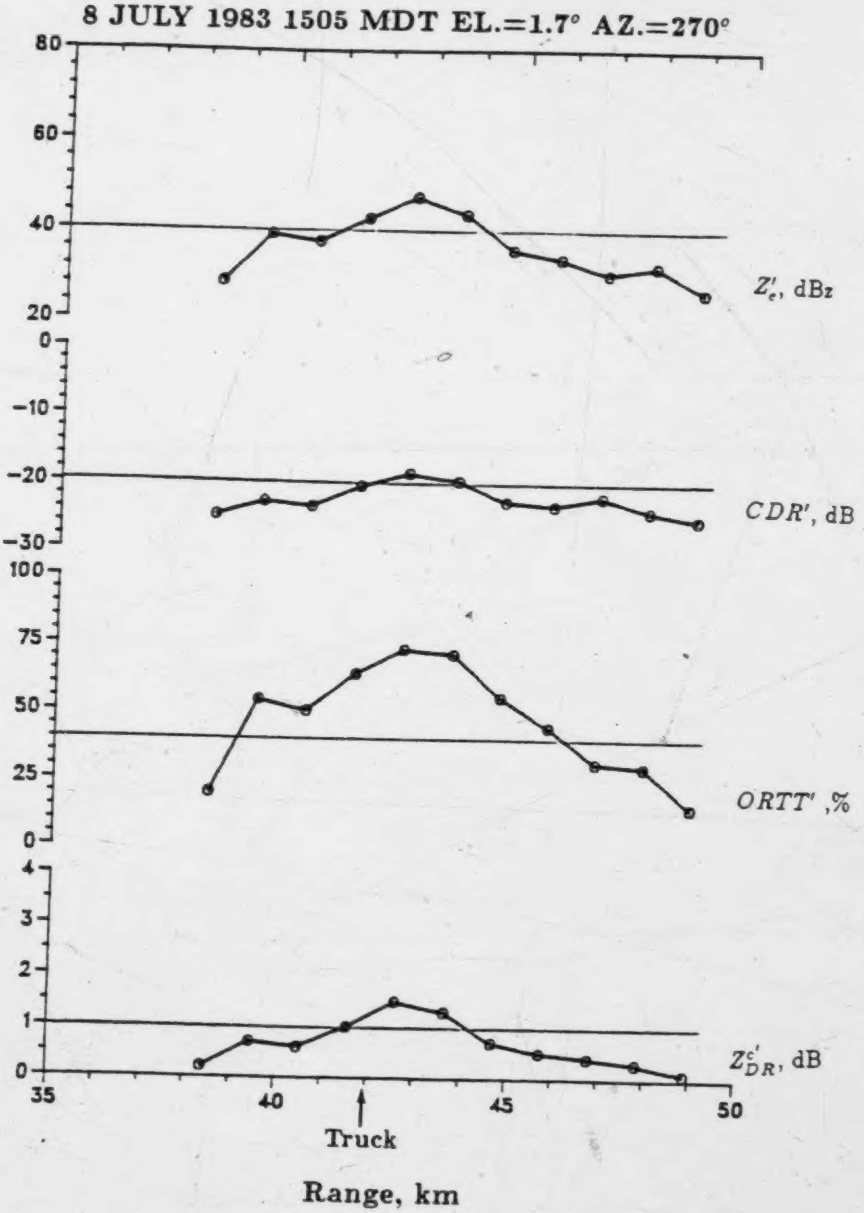

Figure 6.1 8 July 1983. Corrected radar observations along a radial at 1.7° elevation, 270° azimuth, at 1505 MDT. Rain only, 56 mm/hr, was observed at the truck location (42 km range).

Figure 6.2 shows the PPI maps of Z_e', CDR', $ORTT'$, and $Z_{DR}^{c'}$ for 24 July 1983 at 2039 MDT, at an elevation angle of 1.6°. In the vicinity of the truck location, which is marked by X on the maps, it can be seen that high values of Z_e' (40 to 60 dBz) were associated with values CDR' between -20 dB and -15 dB, $ORTT'$ greater than 60%, and $Z_{DR}^{c'}$ above the 1 dB level. These signatures are ideal for rain and are in agreement with ground observations. Farmers' reports for the day indicated that only rain had fallen in the area covered by the echoes in Figure 6.2.

At the far side of the storm relative to the radar, a pocket of high Z_e (greater than 60 dBz) with relatively low values of CDR', $ORTT'$ and $Z_{DR}^{c'}$ can be seen. When Z_e' reaches values greater than 60 dBz, there is a strong possibility of the presence of hail within the radar volume cell. This led to the conclusion that the slight drop in CDR', $ORTT'$, and $Z_{DR}^{c'}$ may have been produced by small hail aloft which melted before reaching the ground. More evidence to support this conclusion will be presented in Section 6.3. At the far edge of the storm, a pattern of low Z_e (less than 30 dBz), associated with low readings of $ORTT'$ (close to 0%) and $Z_{DR}^{c'}$ (near 0 dB), can be seen. These values were most likely to have resulted from a weak signal which can easily be contaminated by noise. Furthermore, the two orthogonal components of the received signal were close to the noise level, which is to be expected at the far edge of the storm.

The values of the polarization parameters along the 221° azimuth radial which passed directly over the truck location are illustrated in Figure 6.3. Between the 45 and 52 km range, the values of the radar parameters above the sampling site suggest a heavy rainfall rate of about 75 mm/hr (Torlaschi *et al.*, 1984) which is

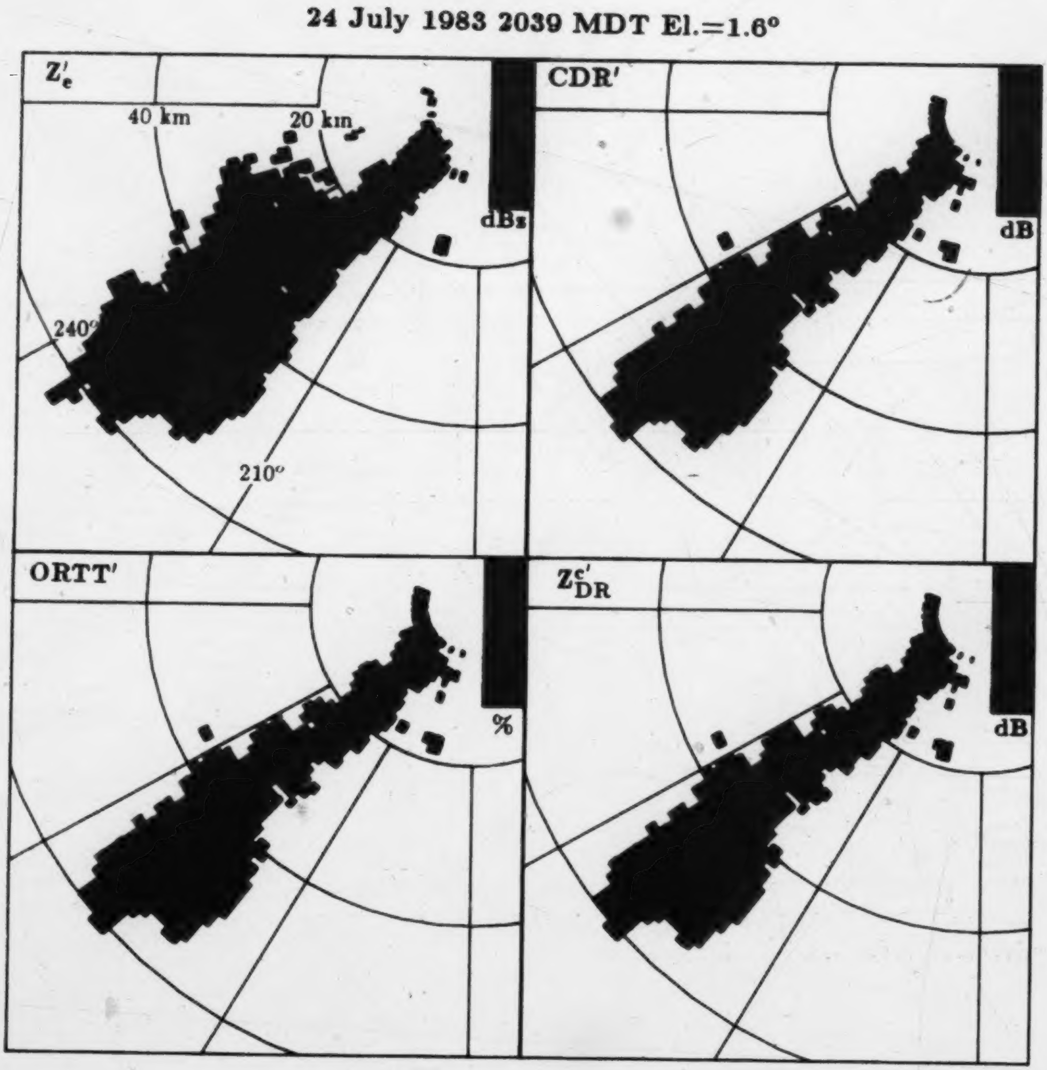
24 July 1983 2039 MDT El.=1.6°
Z_e'
40 km
20 km
dBz
240°
210°
CDR'
dB
ORTT'
%
$Z_{DR}^{c'}$
dB

Figure 6.2 24 July 1983. PPI maps of corrected radar parameters at 1.6° elevation, at 2039 MDT. Rain only, 77 mm/hr, was observed at the ground at the location marked by x. At this location Z_e' was greater than 50 dBz, CDR' ranged between -20 to -15 dB, $ORTT'$ was higher than 80%, and $Z_{DR}^{c'}$ was greater than 1 dB. These all indicate rain and are consistent with the truck observations.

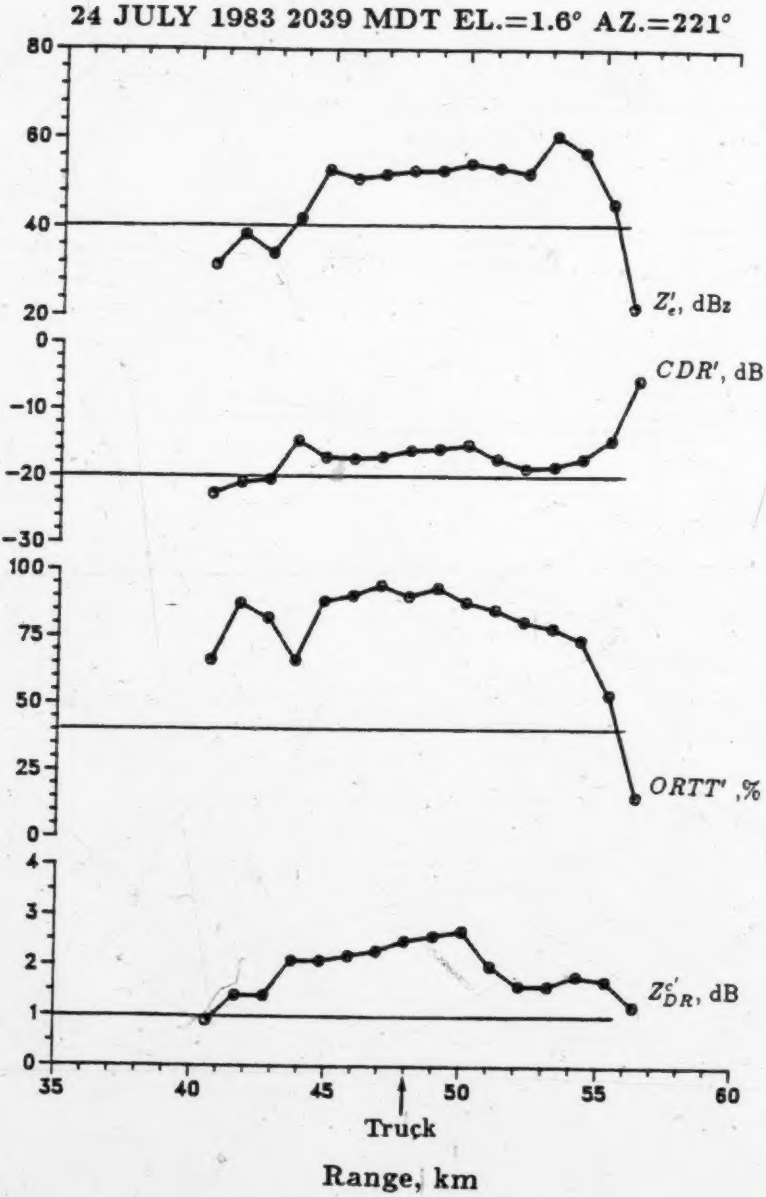

Figure 6.3 24 July 1983. Corrected radar observations along a radial at 1.6° elevation, 221° azimuth, at 2039 MDT. Rain only, 77 mm/hr, was observed at truck location (48 km range).

very consistent with the truck observation of 77 mm/hr at the 49 km point. Again the situation for the existence of hail aloft can be seen at the 53 km point where Z_e' locally increased to over 60 dBz while the three polarization parameters dropped slightly. Beyond the 54 km point, which coincides with the far edge of the storm, a trend of decreasing Z_e', $ORTT'$, and $Z_{DR}^{c'}$ with increasing CDR' can be seen. As suggested above, these values are attributed to the weak signals from that location.

28 July 1983: The storm was situated 60 km WNW of the radar. Light rainfall was measured by the storm chase crew at 282° azimuth and 67 km range from the radar site. A maximum rainfall rate of 5 mm/hr was observed in several 30 s periods, with a mean rate of 3 mm/hr recorded between 1710 and 1714 MDT . Figure 6.4 shows the values of the four parameters along a radial at 1.8° elevation and 282° azimuth at 1709 MDT. From the near edge across the storm, Z_e' increased gradually, with one minor peak near the truck, from values near 30 dBz to values near 50 dBz and then dropped to about 35 dBz. CDR' was rather uniform, remaining near -19 dB. The patterns of $ORTT'$ and $Z_{DR}^{c'}$ were very similar to the pattern of Z_e'. These all imply that only rain was produced by the storm. In the immediate vicinity of the sampling truck, Z_e' was about 32 dBz with CDR' value of -20 dB, $ORTT'$ of 54%, and $Z_{DR}^{c'}$ of 0.9 dB. Since only light rain was observed at the ground, these moderate values of the radar parameters were likely to have resulted from a concentration of small raindrops. Based on the rain model of Torlaschi *et al.* (1984), Z_e' values of 32 dBz and CDR' values of -20 dB would result from low rainfall rates of 5 mm/hr or so. The model predicts $ORTT'$ of 81%. However, the observed value

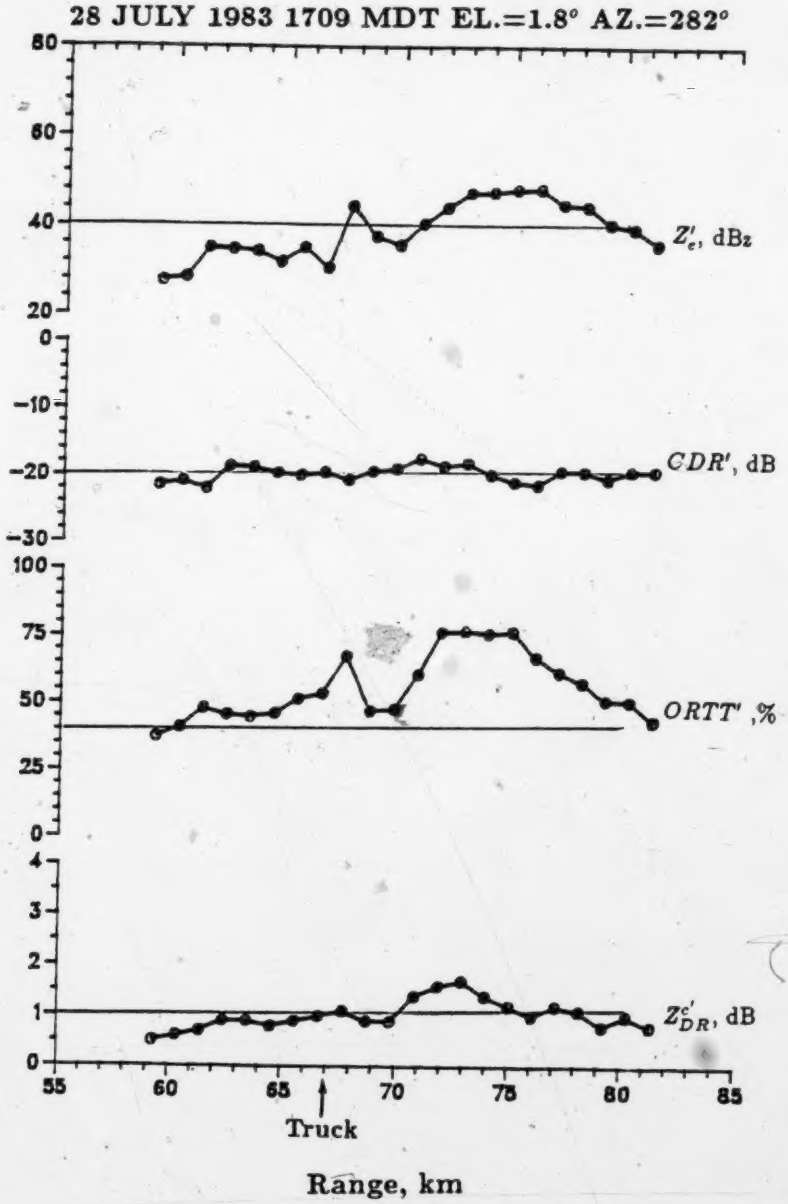

Figure 6.4 28 July 1983. Corrected radar observations along a radial at 1.8° elevation, 282° azimuth, at 1709 MDT. Rain only, 3 mm/hr, was observed at truck location (67 km range).

was 54%. It should be noted that for rain, the model assumes a distribution of canting angle about 0° so that $ORTT$ is expected to be high. This might not be true for small rain drops because they are usually nearly spherical and tend to oscillate (Goddard *et al.*, 1982), causing the degree of orientation $ORTT$ to assume moderate values. Previous observations of light rain (Humphries, 1974a) have also had values of $ORTT'$ between 40% and 60%.

The three rain storms discussed above illustrate that precipitation consisting of rain only is generally characterized by values of CDR' between -22 and -16 dB, $ORTT'$ values greater than 40%, and $Z_{DR}^{c'}$ values between 0.5 and 4 dB. Furthermore, the data suggest that in rain the polarization parameters are well correlated with Z_e'. This is expected, since an increase in Z_e' usually corresponds to an increase in rainfall rate, and the larger raindrops associated with increased rates are necessarily more oblate and tend to fall with their minor axes vertical (preferentially oriented); hence CDR', $ORTT'$, and $Z_{DR}^{c'}$ will also increase. It is important to note that the rain signatures of $Z_{DR}^{c'}$ are consistent with those determined by differential reflectivity radar measurements (Bringi *et al.*, 1984; Leito and Watson, 1984; Aydin *et al.*, 1986), suggesting that in addition to CDR and $ORTT$, circular polarization measurements offer a very good estimate of the Z_{DR}.

6.3 Hail Observations

31 July 1982: On the evening of 31 July 1982, heavy rainfall rate reaching 45 mm/hr with pea-size hail were observed northwest of the radar between 1850 and 1900 MDT. This mixture is suggested by the radial plots in Figure 6.5 taken along

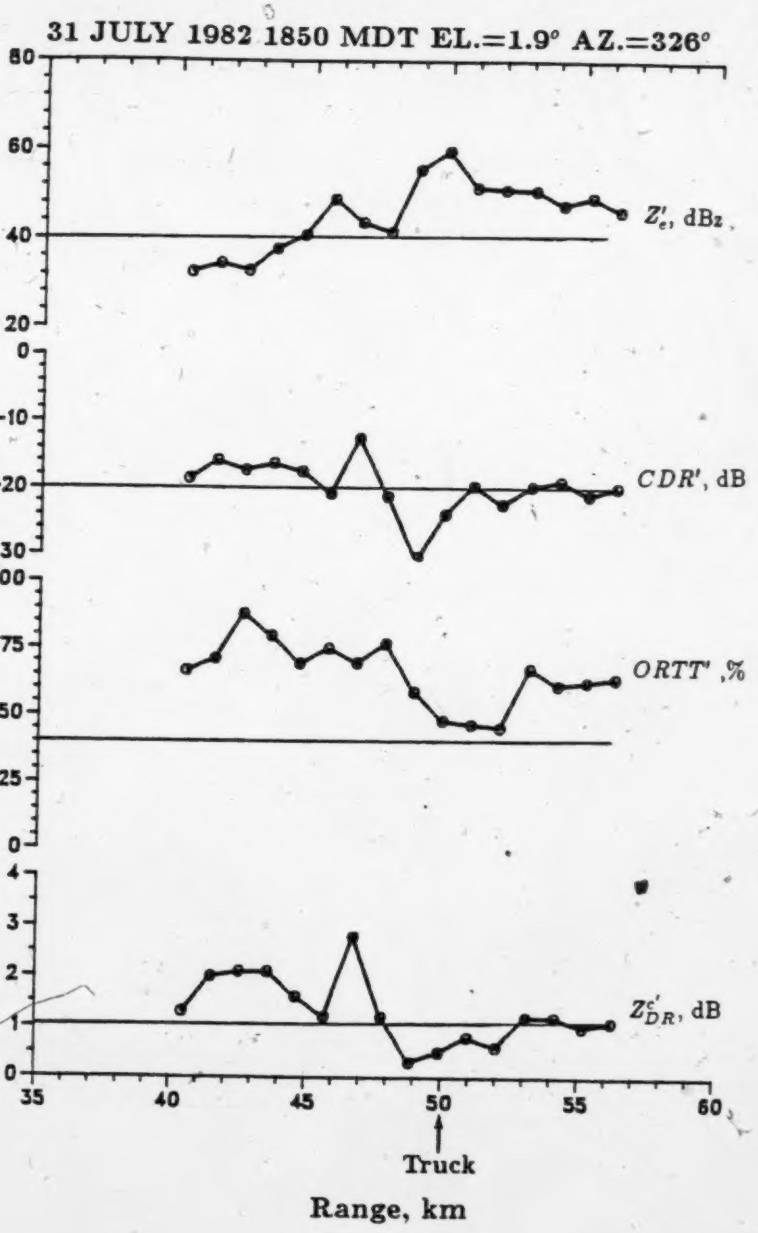

Figure 6.5 31 July 1983 Corrected radar observations along a radial at 1.9° elevation, 326° azimuth, at 1850 MDT. Heavy rainfall, 45 mm/hr, and pea-size hail was observed at the truck location (50 km range).

a line across the sampling site location at the 326° azimuth and 50 km range. Between 40 and 48 km, Z_e' ranged from 32 to 45 dBz, CDR' was greater than -20 dB, $ORTT$ was higher than 65%, and $Z_{DR}^{c'}$ was greater than 1 dB. As discussed in the previous section, these values indicate strongly that only rain was present at these ranges. Near the truck location (50 km range), where the mixture of heavy rain and hail was observed, Z_e' suddenly jumped to values near 60 dBz while CDR', $ORTT'$, and $Z_{DR}^{c'}$ dropped drastically to relatively low values of -22 dB, 50%, and 0.5 dB respectively. These appear to be confirmed by hail observation at the truck location. The rain and hail mixture model of Torlaschi *et al.* (1984) suggests that these observed values would result from a mixture of heavy rain and small hail. Beyond the truck location (50 km range), it is apparent that rain again started to dominate the signal as Z_e' decreased to values near 48 dBz while CDR' ,$ORTT'$, and $Z_{DR}^{c'}$ generally increased.

12 July 1983: During the afternoon of 12 July 1983, precipitation measurements of rain and hail up to grape-size were made at the 196° azimuth and 60 km range. A mean rainfall rate of 38 mm/hr was measured between 1647 and 1652 MDT, with grape-size hail observed between 1648 and 1652 MDT. Figure 6.6 shows the values of Z_e', CDR', $ORTT'$, and $Z_{DR}^{c'}$ along the 196° radial at 1.5° elevation, at 1649 MDT. From the near side up to the truck, located at 60 km range, Z_e' increased steadily from 40 dBz to about 58 dBz, CDR' decreased to less than -20 dB , $ORTT'$ dropped to less than 30%, and $Z_{DR}^{c'}$ decreased to less than 0.5 dB. These proposed hail signatures are consistent with the observations of grape-size hail. At the far

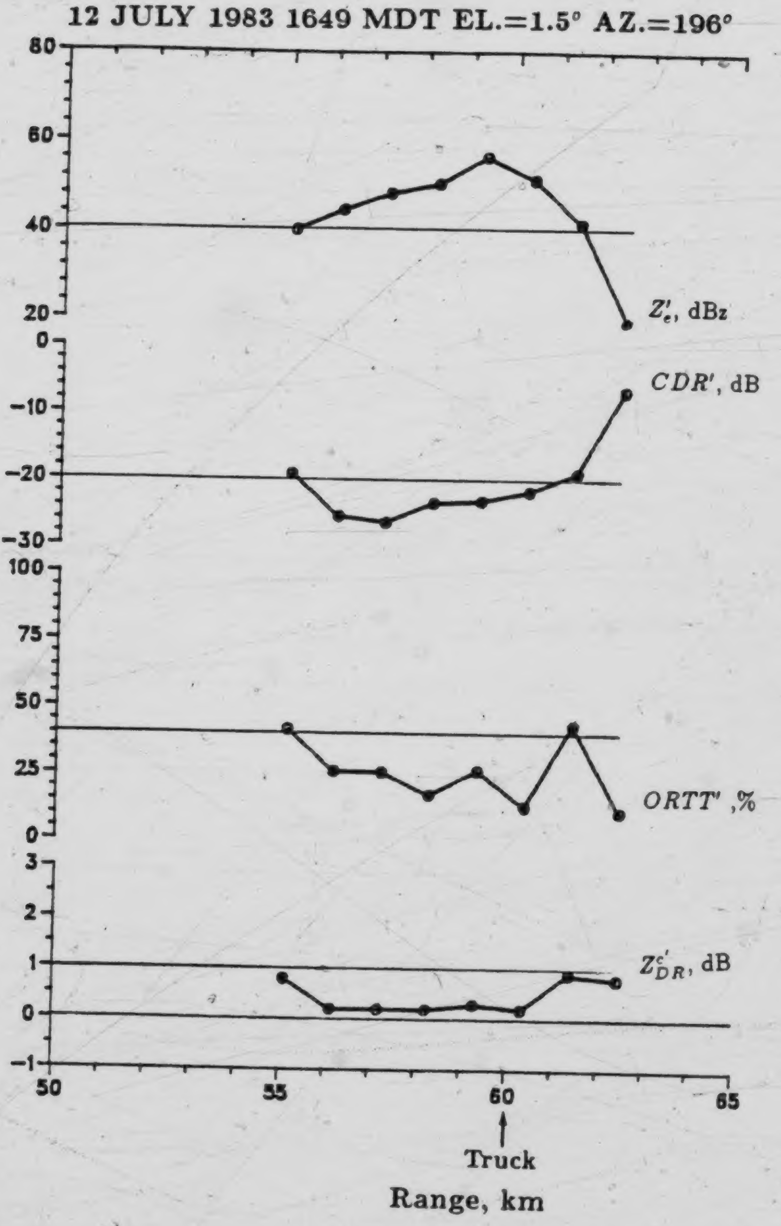

Figure 6.6 12 July 1983. Corrected radar observations along a radial at 1.5° elevation, 196° azimuth, at 1649 MDT. Heavy rainfall, 38 mm/hr, and grape-size hail was observed at the truck location (60 km range).

edge, trends of decreasing Ze' and $ORTT'$ and increasing CDR' are most likely due to the orthogonal signal being close to noise level rather than due to precipitation.

15 August 1983: At mid-afternoon on 15 August 1983, major storms developed south of the radar site. The storms intensified as they tracked eastward and eventually merged to form a line in the southeast quadrant of the project area. The two distinct hail swaths were at least 40 km long and oriented in an east-west direction. The storm produced heavy to very heavy rain with grape-size hail at the mobile collection site (the 121° azimuth and 34 km range) over 30 s periods, with an average rainfall rate of 83 mm/hr based on the accumulation between 1616 and 1620 MDT. Hailstone-size distributions were observed from 1618 to 1620 MDT. Grape-size hail was most common, but up to walnut-size was observed at times.

The 1.3° PPI maps of the radar parameters for 15 August 1983 at 1617 MDT are shown in Figure 6.7. In the north section of the storm there is a good pattern of the radar parameters for rainfall: low to moderate Z_e' with CDR' values between -25 to -15 dB, $ORTT'$ values greater than 60%, and $Z_{DR}^{c'}$ above 1 dB. Over a 24-hr period, only rain was reported by farmers in those localities. South of these regions, the existence of hail is suggested by the intensified Z_e' (greater than 60 dBz), very low $ORTT'$ (less than 30%), a moderately low CDR' (less than -20 dB), and low values of $Z_{DR}^{c'}$ (close to 0 dB). This was corroborated by the truck observations at the location marked X on the maps. The hailfall summary map of this date indicated that hail was observed by the farmer network in this area.

The values of the radar parameters for the 121° radial path, which passed directly

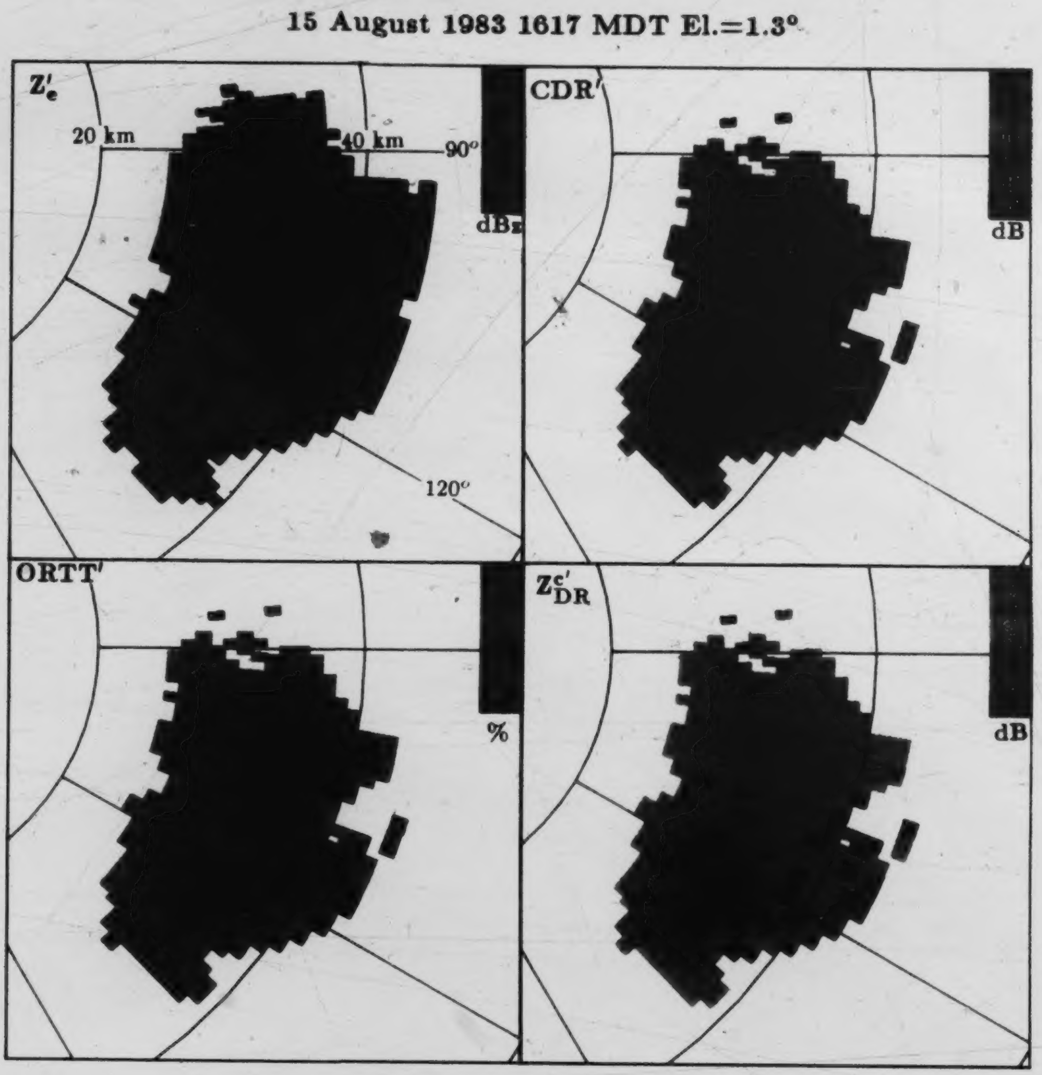
15 August 1983 1617 MDT El.=1.3°
Z'e
20 km
40 km
90°
120°
dBz
CDR'
dB
ORTT'
%
Z^c'_DR
dB

Figure 6.7 15 August 1983. PPI maps of corrected radar parameters at 1.3° elevation, at 1617 MDT. Very heavy rain, 83 mm/hr, and grape-size hail was observed at the ground at the location marked by x. Note that the presence of hail resulted in very high Z_e' (greater than 60 dBz) and low values of CDR' (less than 20 dB), $ORTT'$ (less than 40%), and $Z_{DR}^{c'}$ (less than 1 dB).

above the sampling site, are shown in Figure 6.8. From the near edge of the storm relative to the radar out to 34 km range (the truck location) Z'_e increased gradually to about 62 dBz, at which point CDR' decreased to -22 dB, $ORTT'$ dropped to about 35%, and $Z^{c'}_{DR}$ dropped to 0.5 dB. Based on the Torlaschi *et al.*'s (1984) rain/hail model, these values indicate the observed hail. Beyond this point, Z'_e decreased while $ORTT'$, CDR' and $Z^{c'}_{DR}$ increased, presumably due to relatively small hail and the increased presence of rain in the radar volume cell.

As a supporting example, Figures 6.9a through 6.9d show the Range-Height-Indicator (RHI) vertical cross sections of Z'_e, CDR', $ORTT'$, and $Z^{c'}_{DR}$, valid at the 121° azimuth at 1617 MDT for the 15 August 1983 storm. On this date, the 0 °C level was at about 3.8 km. At higher altitudes, it can be seen (Figure 6.9a) that the regions of very high Z'_e were associated with low readings of CDR' of less than 30 dB (Figure 6.9b), $ORTT'$ less than 30% (Figure 6.9c), and $Z^{c'}_{DR}$ close to 0 dB (Figure 6.9d), suggesting that there was a strong likelihood of the presence of precipitation particles other than rain. Among precipitation particles, only hail is believed capable of yielding very high Z'_e at high altitudes. Therefore, hail was responsible for the low values of the other three parameters. Closer to the ground, particularly below the 2° elevation (about 1.5 km) where it was warm (surface temperature was 26 °C), the presence of rain is suggested by the apparent increase in CDR', $ORTT'$, and $Z^{c'}_{DR}$. The data also show that the intense core of the storm (Z'_e greater than 60 dBz) was located directly above the sampling truck at 34 km range where a mixture of very heavy rain and grape-size hail was observed. In this region, CDR' values were less than -20 dB, and $ORTT'$ and $Z^{c'}_{DR}$ were less than

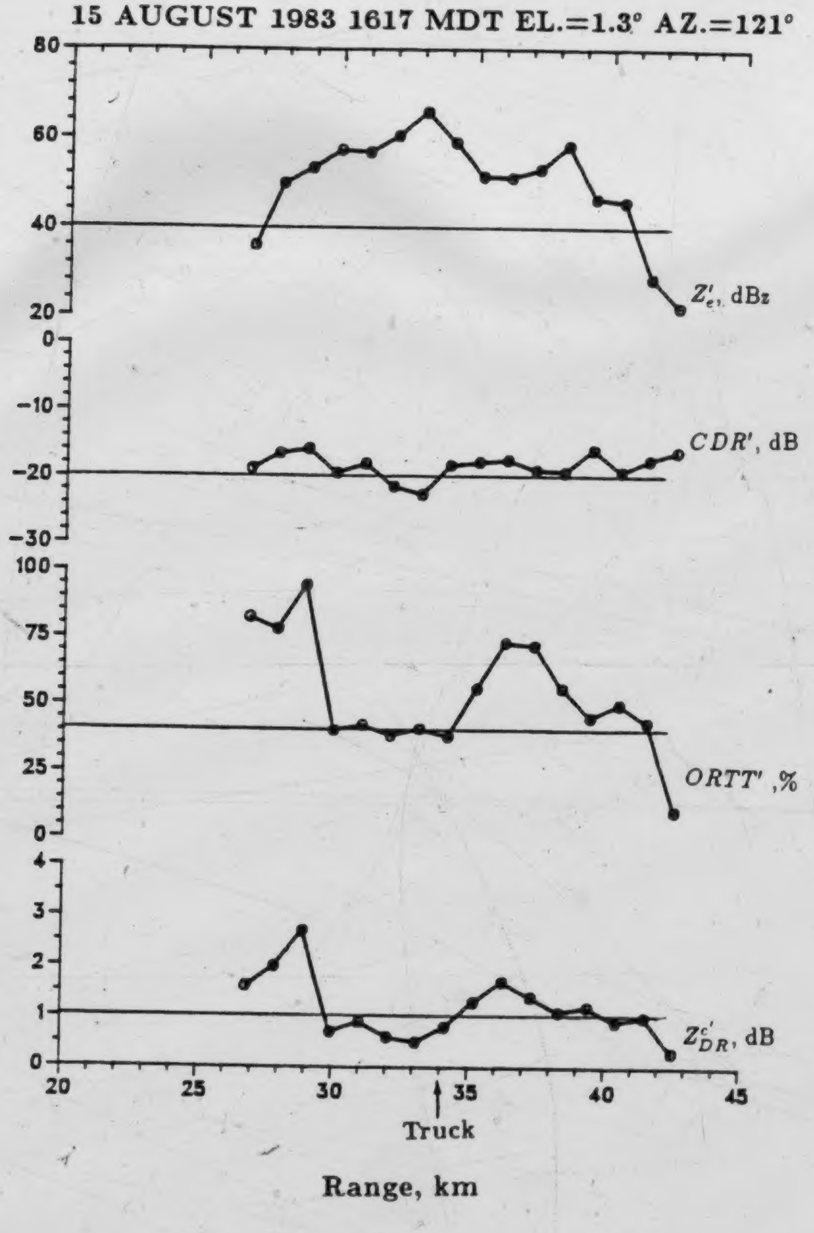

Figure 6.8 15 August 1983. Corrected radar observations along a radial at 1.3° elevation, 121° azimuth, at 1617 MDT. Very heavy rain, 83 mm/hr, and grape-size hail was observed at the truck location (34 km range).

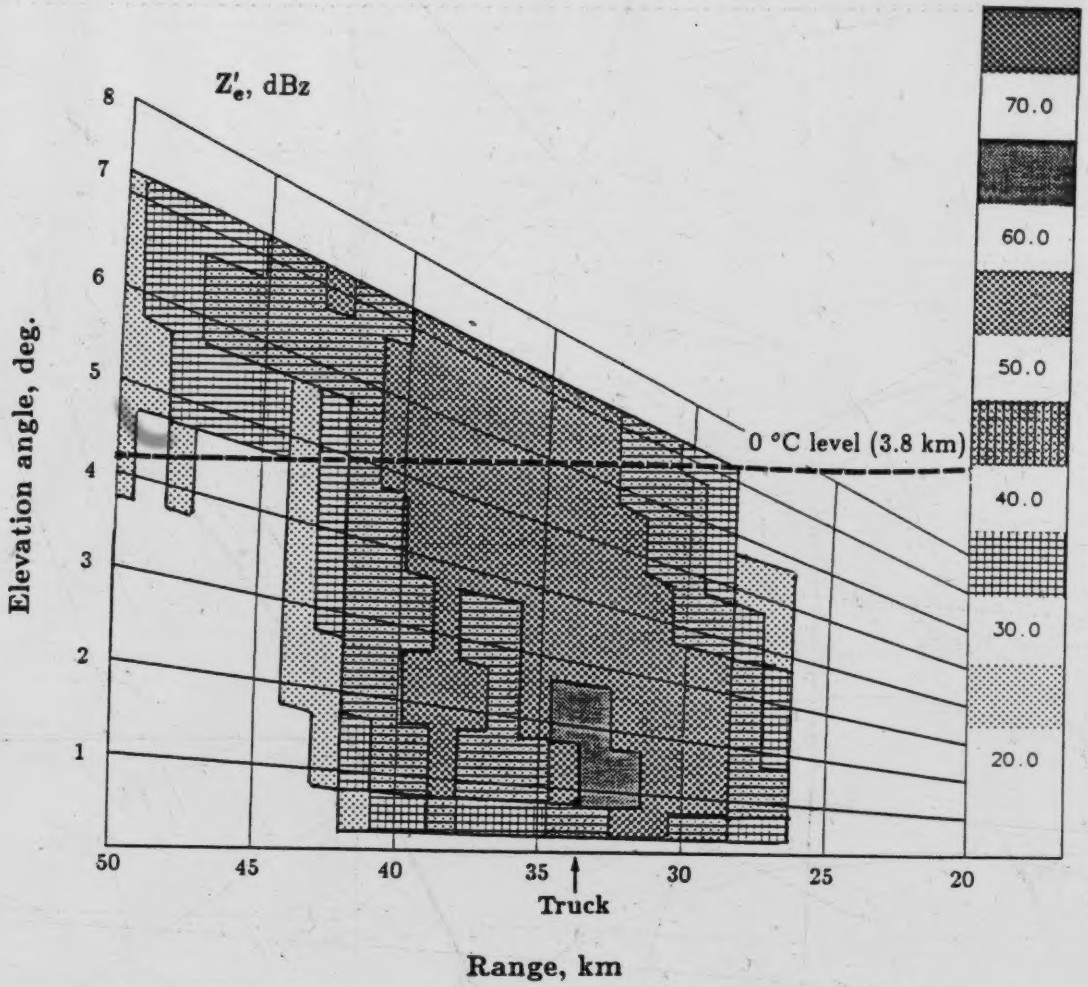

Figure 6.9a 15 August 1983. RHI map of Z_e' at 121° azimuth, at 1617 MDT. Very heavy rain, 83 mm/hr, and grape-size hail was observed at the truck location.

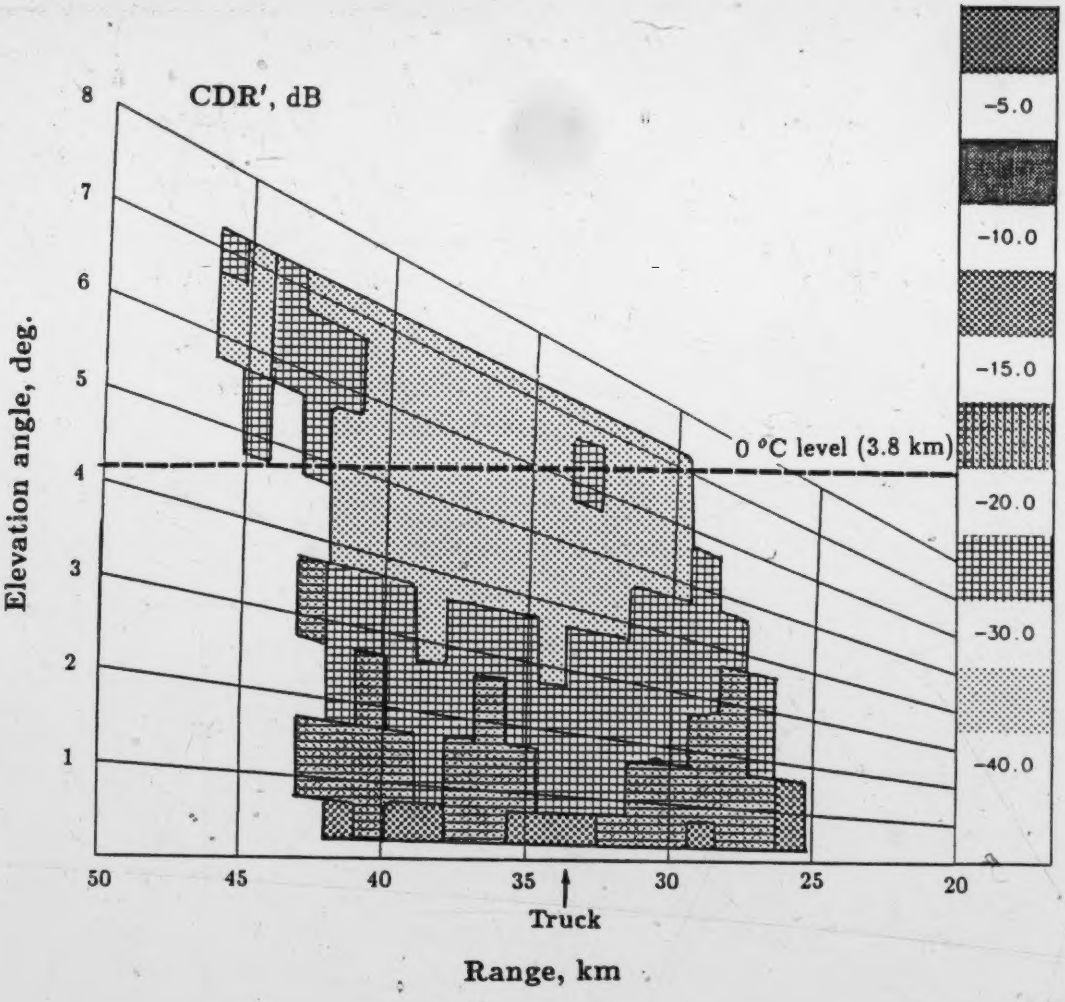

Figure 6.9b 15 August 1983. RHI map of *CDR′* at 121° azimuth, at 1617 MDT. Very heavy rain, 83 mm/hr, and grape-size hail was observed at the truck location.

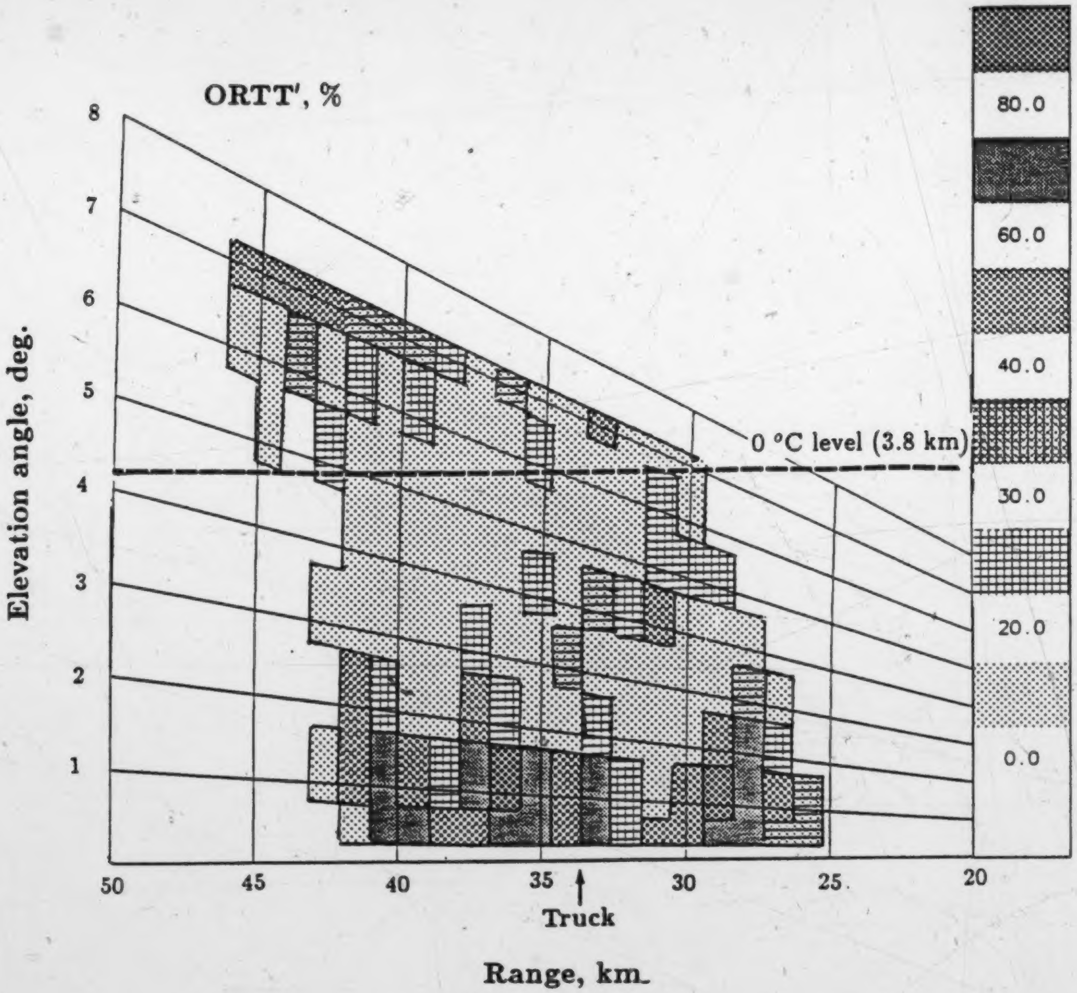

Figure 6.9c 15 August 1983. RHI map of *ORTT'* at 121° azimuth, at 1617 MDT. Very heavy rain, 83 mm/hr, and grape-size hail was observed at the truck location.

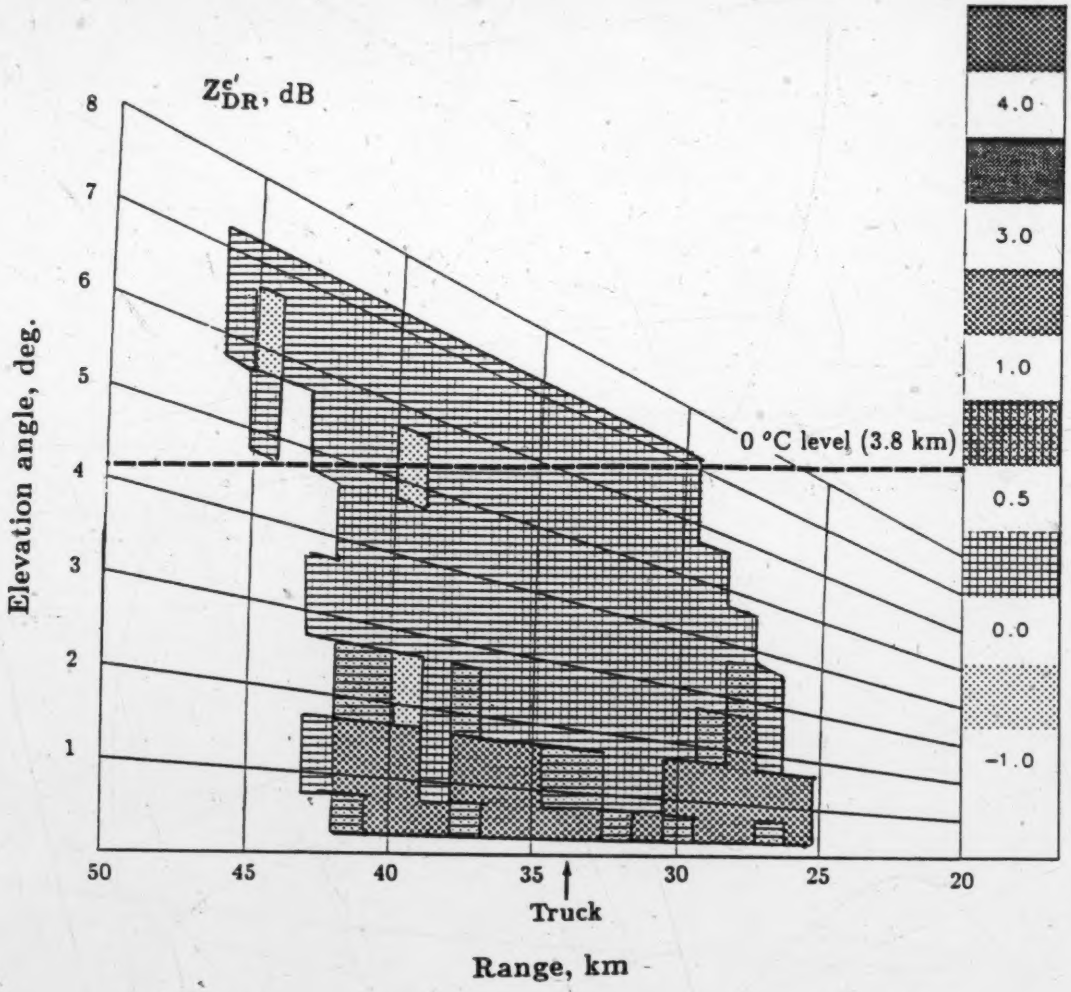

Figure 6.9d 15 August 1983. RHI map of $Z_{DR}^{c'}$ at 121° azimuth, at 1617 MDT. Very heavy rain, 83 mm/hr, and grape-size hail was observed at the truck location.

30% and 0.5 dB respectively. Again these are all due to the hailfall in that region.

25 June 1984: A severe storm with maximum reflectivity near 70 dBz developed in the afternoon of 25 June 1984 southwest of the radar site. Between 1650 and 1700 MDT, a mixture of heavy rain, 51 mm/hr, and walnut-size hail was observed by the truck at approximately 126° azimuth and 45 km range from the radar site. The radar data for the 126° azimuth and 1.3° elevation radial as a function of range are shown in Figure 6.10. Between 31 and 38 km range, an ideal situation for rainfall can be seen as Z_e' maintained values between 40 and 48 dBz with CDR' values near -18 dB, $ORTT'$ values greater than 65%, and $Z_{DR}^{c'}$ values above 1 dB. From 36 km to about 46 km, Z_e' rose gradually to 72 dBz while $ORTT'$ and $Z_{DR}^{c'}$ drastically dropped to values near 15% and 0 dB respectively. These values are consistent with the hail that was observed at the 45 km point. For this example, CDR' increased in the hail region instead of decreasing as expected. This may be attributed to the presence of large deformed hailstones.

The four hail-producing severe storms discussed above demonstrate that in the transit from a rain only region to a region containing hail, the large size of hailstones compared with raindrops causes Z_e' to increase while the irregular shapes and tumbling motions (random orientation) of the hail particles generally result in low readings of CDR', $ORTT'$, and $Z_{DR}^{c'}$. This opposite relationship between Z_e' and the polarization parameters during hailfall is contrary to the relationship seen in rain and suggests the usefulness of polarization techniques in distinguishing rain from the ice-phase or mixed precipitation in convective storms.

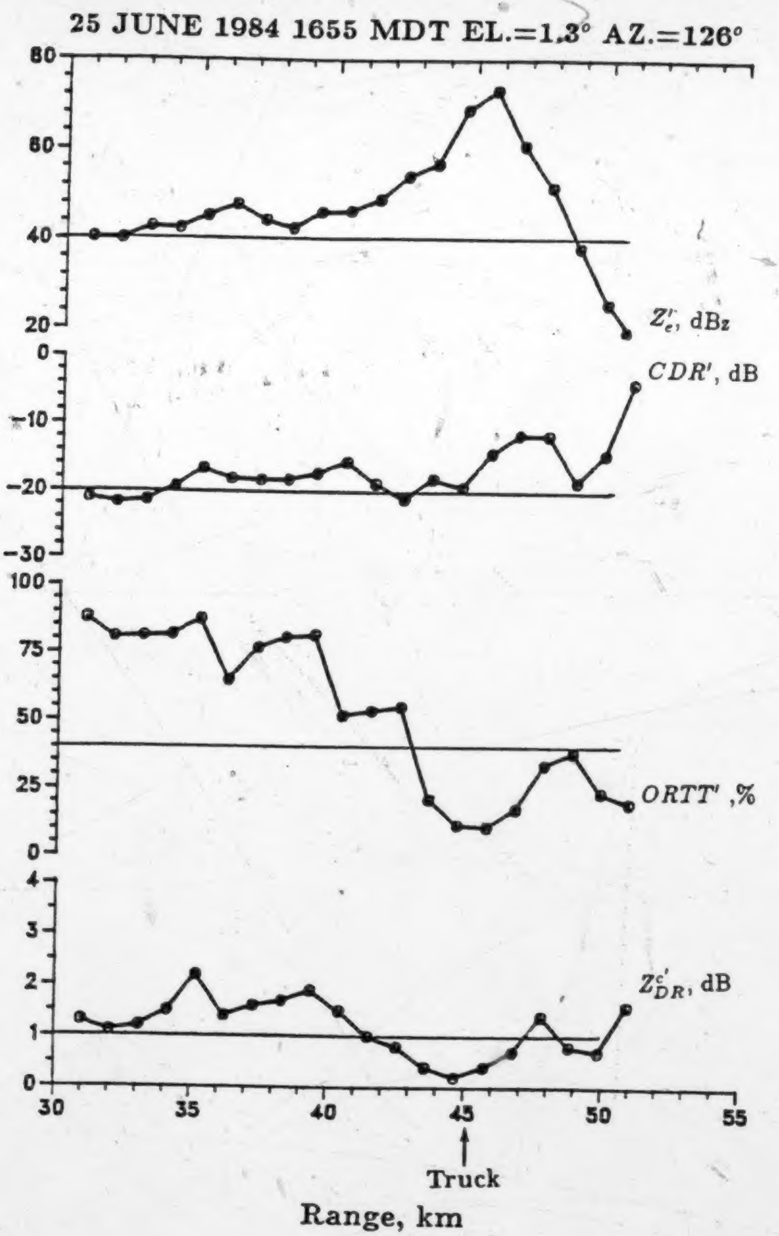

Figure 6.10 25 June 1984. Corrected radar observations for a radial at 1.3° elevation, 126° azimuth, at 1655 MDT. Heavy rainfall, 51 mm/hr, and walnut-size hail was observed at the truck location (45 km range).

One must now ask which polarization parameter best discriminates between rain and hail and if polarization techniques actually provide an improvement over the use of conventional radars which measure Z_e alone? These problems are the main concern of the following section.

6.4 Relationships between Z_e' and Polarization Parameters

This section sets out to discover which polarization parameters provide the best discrimination between rain and hail and whether a combination of Z_e and polarization parameters offers improvement for rain and hail identification over the use of Z_e alone. To increase the sampling, analyses were carried out by extracting radar data in the vicinity of the mobile precipitation sampling vehicles (± 1 km of the truck location) for the same time period as the ground truth data for three rain only cases and for four rain and hail mixture cases. All seven case studies were discussed in detail in the previous sections.

Figures 6.11, 6.12, and 6.13 are scatter plots of CDR' versus Z_e', $ORTT'$ versus Z_e', and $Z_{DR}^{c'}$ versus Z_e' respectively. The open symbols represent only rain observations and the filled symbols represent observations of rain and hail mixtures. All data were corrected for propagation effects so that the values shown correspond to the intrinsic properties of precipitation. From Figure 6.11 it can be seen that, in general, rain observations were associated with values of CDR' larger than those produced by rain and hail mixtures for a given Z_e', but the $Z_{e'} - CDR'$ relationship does not separate the points well. However, in the critical range of Z_e' values between 50 dBz and 60 dBz, CDR' values showed a good separation between rain

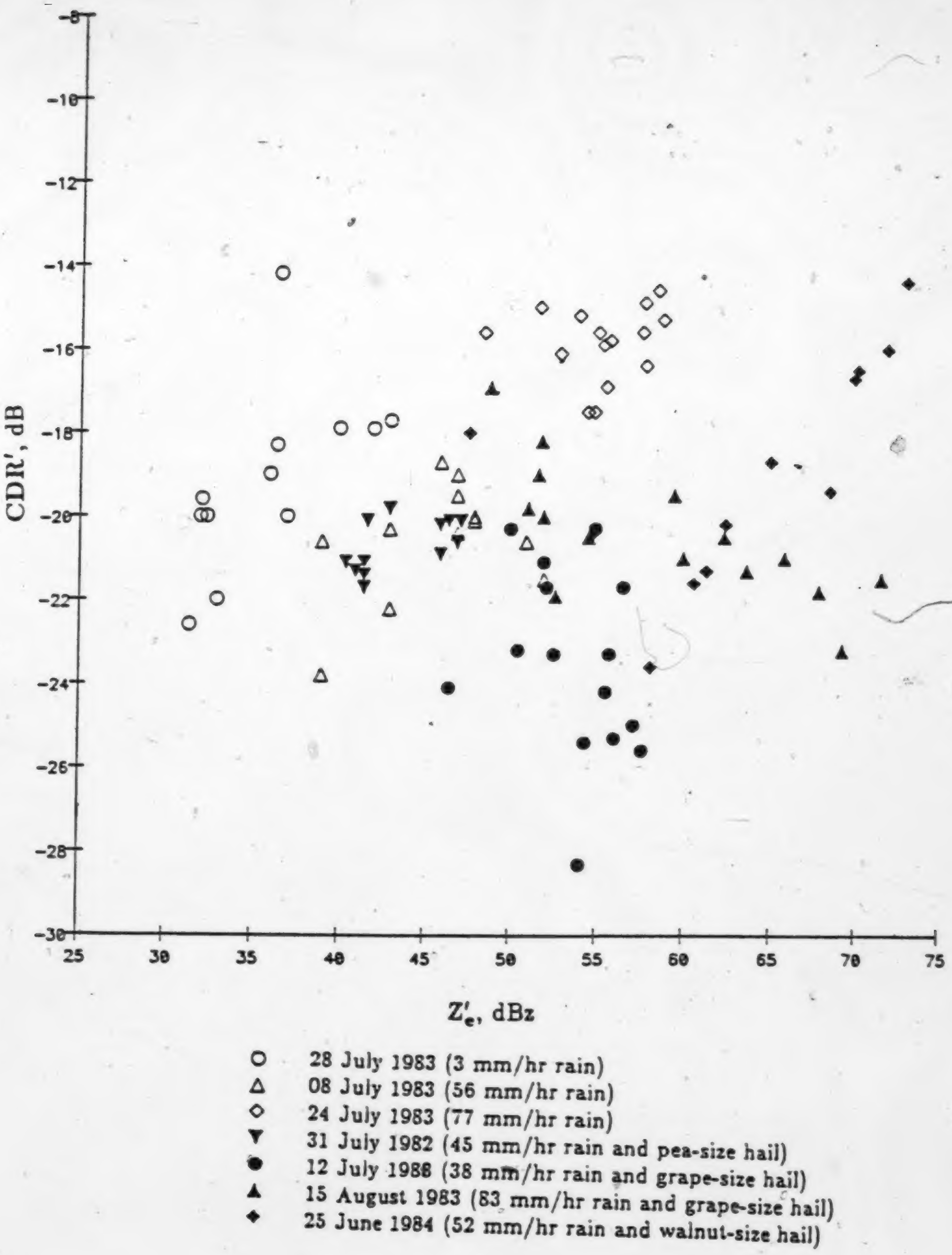

Figure 6.11 Scatter plot of CDR' versus Z'_e for three rain only storms and four rain and hail mixture storms.

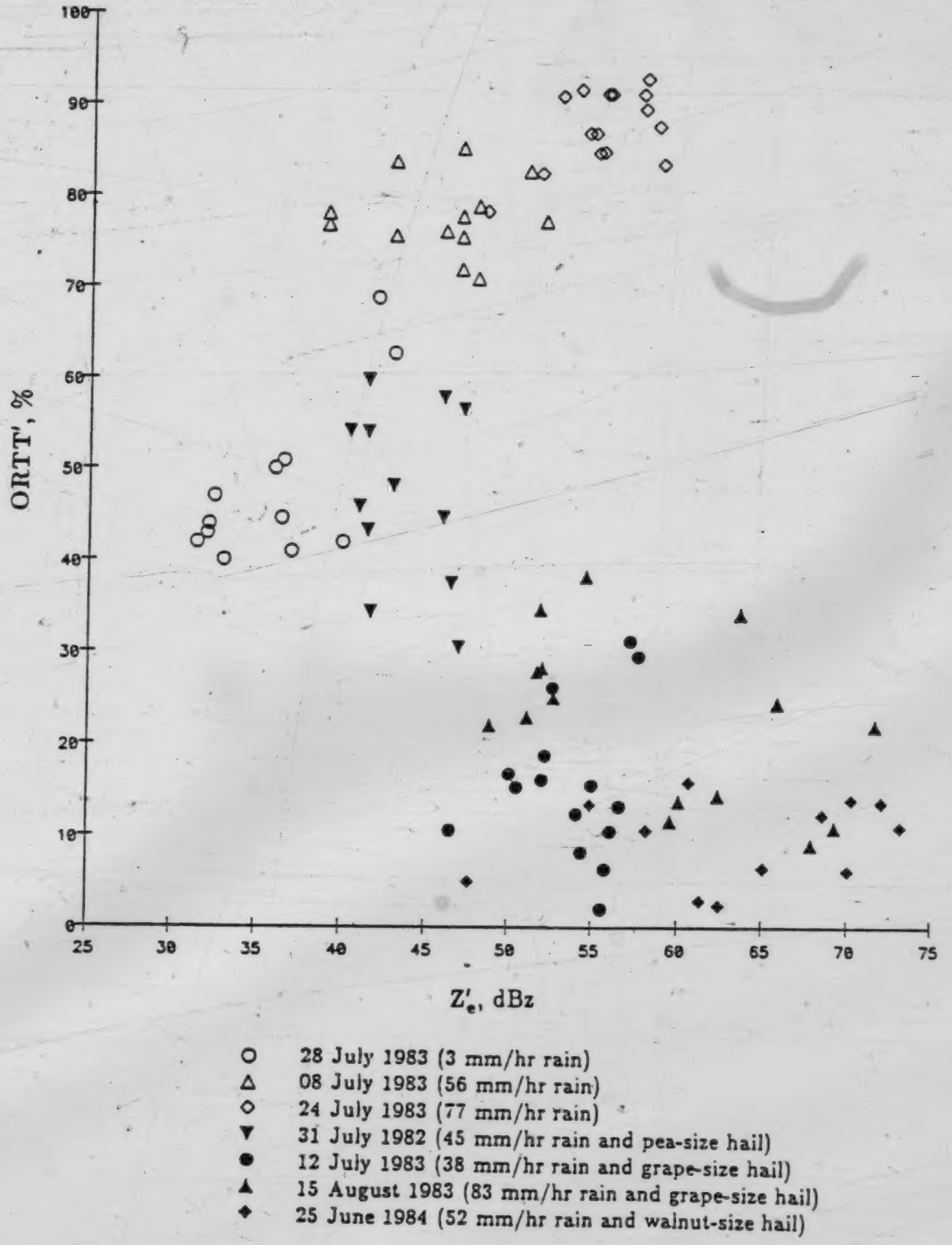

Figure 6.12 Scatter plot of $ORTT'$ versus Z'_e for three rain only storms and four rain and hail mixture storms.

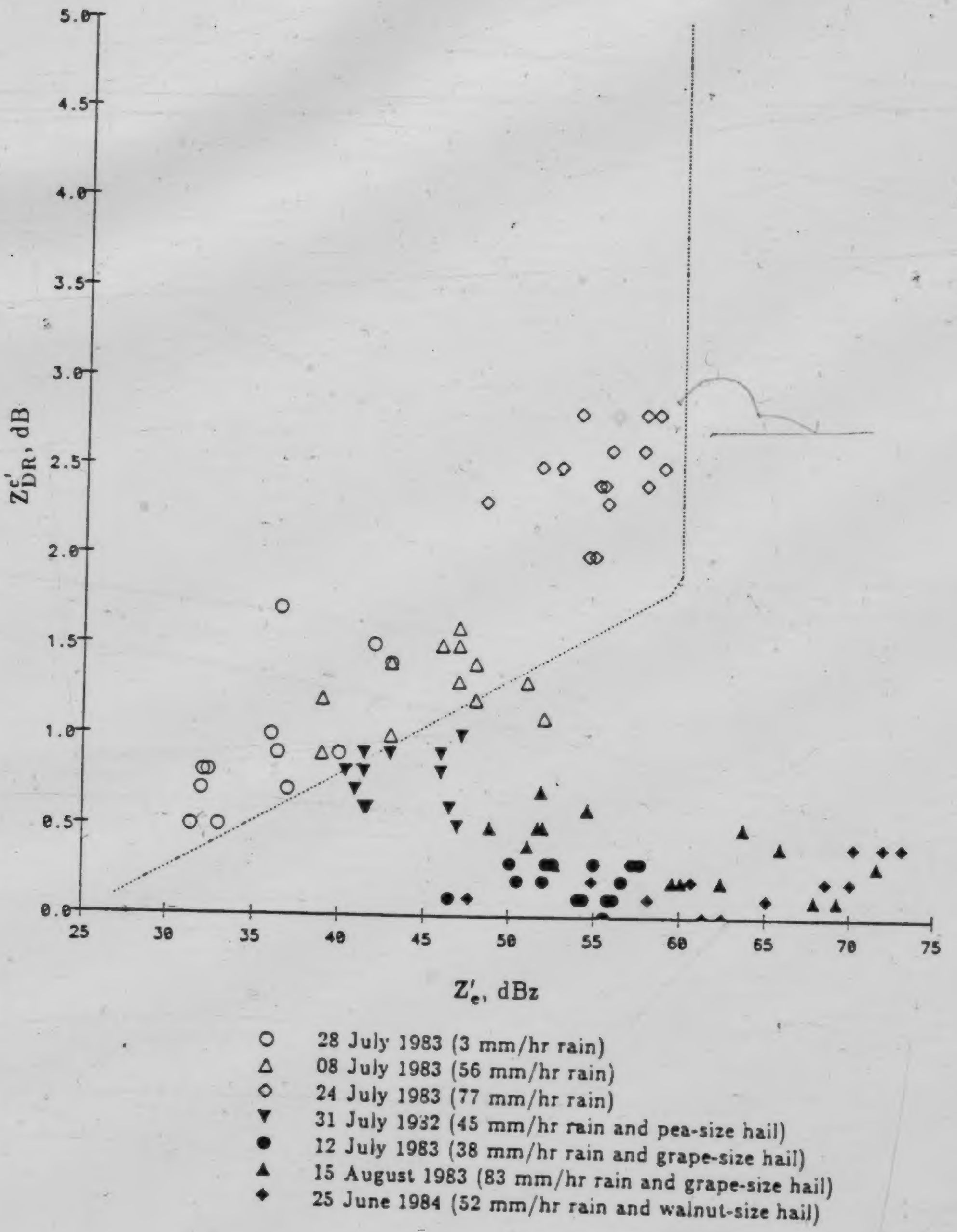

Figure 6.13 Scatter plot of $Z^{c'}_{DR}$ versus Z'_e for three rain only storms and four rain and hail mixture storms. The theoretical rain-hail boundary line is adopted from Aydin et al. (1986).

and hail. In Figure 6.12, it is apparent that rain observations were characterized by values of $ORTT'$ greater than 40% and that the higher values of $ORTT'$ corresponded to larger values of Z_e', i.e., heavier rainfall. Hail observations exhibited values of $ORTT'$ less than 40% with the exception of the 31 July 1983 case study where $ORTT'$ values ranged between 30 and 60%. Such values of $ORTT'$ were likely to have resulted from a heavy rainfall (45 mm/hr) mixed with small pea-size hail, in which case rain was dominating the signal. It can also be seen that the separation between rain and hail observations is clearer than it was for CDR' and that $ORTT'$ value of 40% seems to give the most appropriate boundary between rain and hail. Figure 6.13 shows that $Z_{DR}^{c'}$ also provides very good discrimination, with heavy rain giving values of $Z_{DR}^{c'}$ higher than 1 dB; hail resulted in relatively low values (less than 0.7 dB) in the critical Z_e' range between 40 and 60 dBz. This indicates that $Z_{DR}^{c'}$ is closely related to $ORTT'$, i.e., both exhibit high values for rain and low values for hail. The rain and hail signatures of $Z_{DR}^{c'}$ are very consistent with those obtained using linearly polarized radar (e.g., Bringi *et al.* 1984; Illingworth *et al.*, 1986). Furthermore, our $Z_{DR}^{c'}$ data appear to agree very well with the rain-hail boundary line (Figure 6.13) proposed by Aydin *et al.* (1986) where the line was given as

$$Z_e(\text{dBz}) = \begin{cases} 27, & Z_{DR} \leq 0 \text{ (dB)} \\ 19Z_{DR} + 27, & 0 \leq Z_{DR} \leq 1.74 \text{ (dB)} \\ 60, & Z_{DR} > 1.74 \text{ (dB)} \end{cases} \qquad (6.1)$$

This line was theoretically derived from disdrometer measurements of raindrop size distributions in central Illinois and Colorado assuming a frequency of 2.75 GHz and a temperature of 10 °C. This good agreement with our simultaneous field observations of precipitation and radar echoes suggests that circular and linear polarization techniques provide similar information. The results also imply that the theoretical relationship used to derive Z_{DR} from circular polarization quantities is valid provided that propagation effects are removed from the measurements.

The three scatter plots suggest that Z_e' can be high for both hail and very heavy rain. However, the polarization quantities $ORTT'$ and $Z_{DR}^{c'}$ and to a lesser degree CDR' assume values which show that the discrepancy can be settled in the majority of cases. To support these results, another type of analysis will be carried out in the next chapter whereby radar data are compared with the farmers' reports over a wide area and for day-long observations.

Further evaluation as to the utility of the correction method used to eliminate the propagation effects is shown in Figures 6.14 through 6.16 which compare corrected to uncorrected observations. These figures show that the separation between rain and hail became much clearer after CDR, $ORTT$, and Z_{DR}^{c} were corrected. It is apparent that the differences between corrected and uncorrected $ORTT$ and Z_{DR}^{c} for hail observations are larger than those for only rain observations. This is expected, since the effect of propagation on $ORTT$ and Z_{DR}^{c} is to increase them and for a given Z_e the intrinsic $ORTT'$ and $Z_{DR}^{c'}$ for hail are much lower than those for only rain.

It should be noted that our uncorrected $Z_e - CDR$ data do not conform to the rain-hail boundary line suggested by Barge (1974) and shown in Figure 6.14.

This line was based on uncorrected rain and hail data measured in central Alberta with the ARC radar. It is contrary to current theory and our observations in the sense that it suggests that, given a Z_e, hail is more likely than rain to produce high values of CDR. This discrepancy may be explained by the fact that over the past decade major improvements were made in the radar system, calibration, and data processing which led to more accurate measurements and reliable analysis. Clearly our data (Figure 6.14) appear to agree with the theoretical models of Torlaschi et al. (1984) in that for a given Z_e, hailstones produce CDR values less than those produce by raindrops, apparently because large raindrops are oblate spheroids.

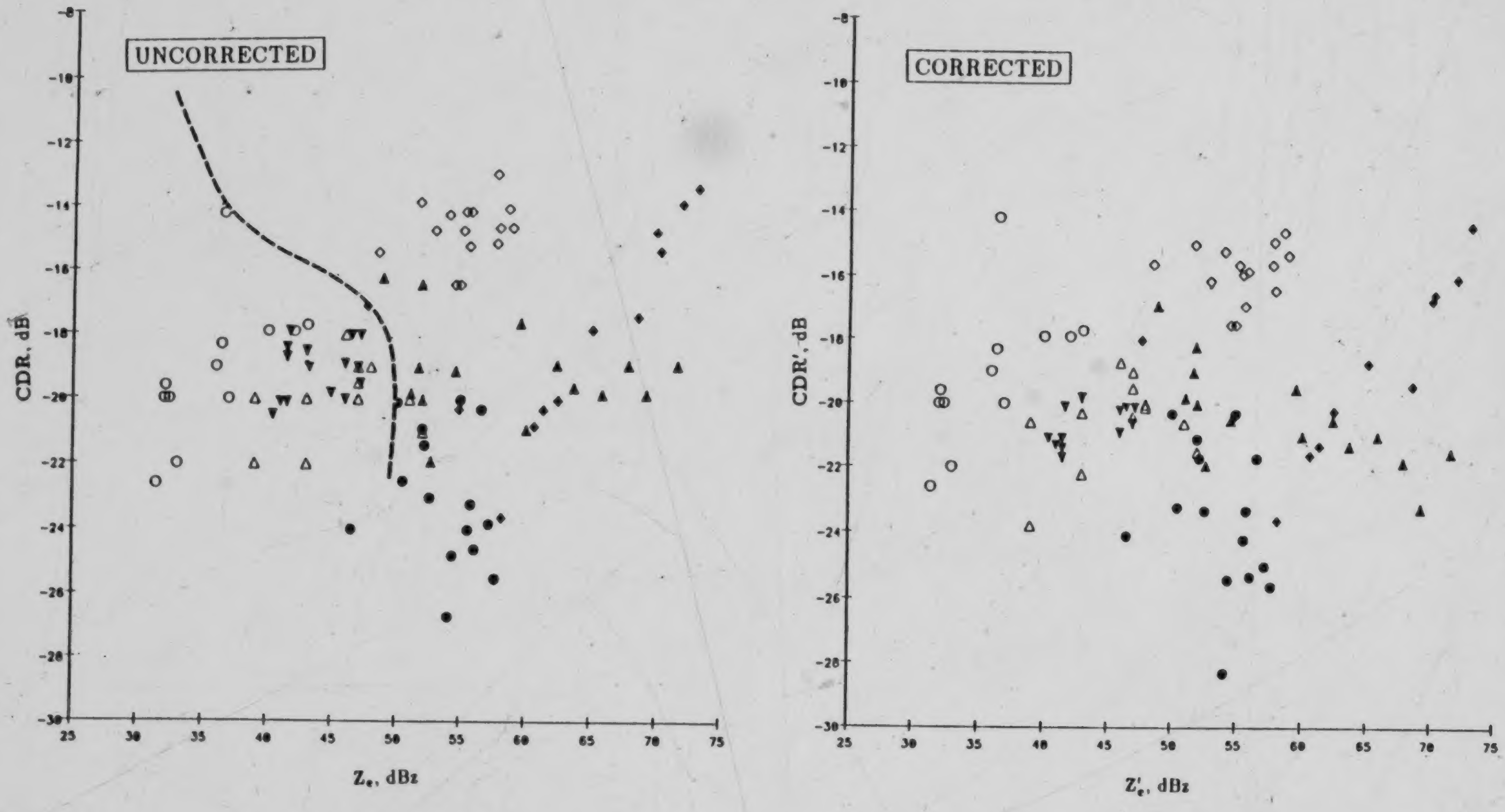

Figure 6.14 Comparison between uncorrected (left diagram) and corrected (right diagram) data for the Z_e-CDR relationship. See Figure 6.13 for the key to the plotted symbols. Barge (1974) rain-hail boundary with hail to the right is shown as dashed line (see text for discussion).

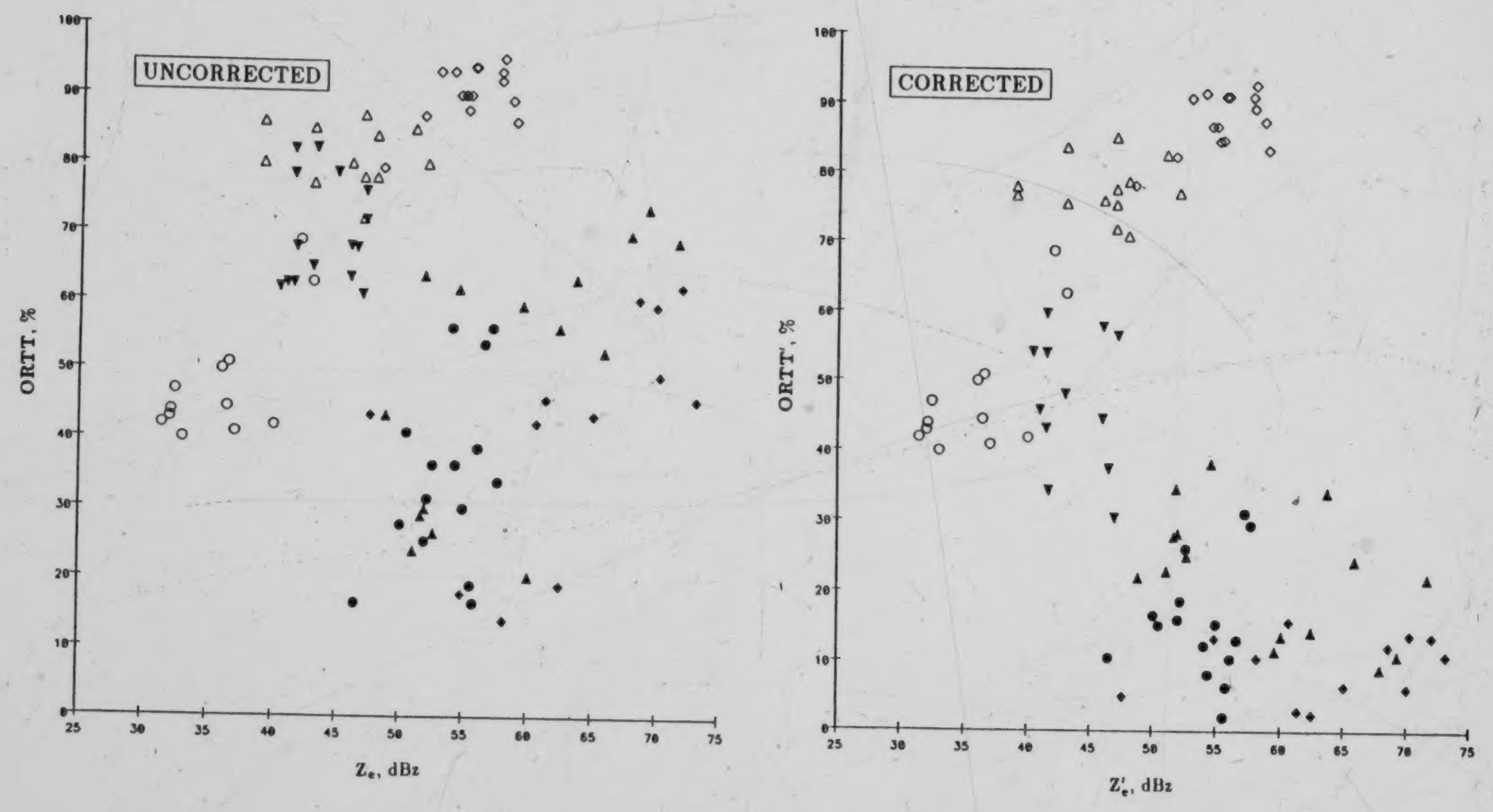

Figure 6.15 Comparison between uncorrected (left diagram) and corrected (right diagram) data for the Z_e-$ORTT$ relationship. See Figure 6.13 for the key to the plotted symbols.

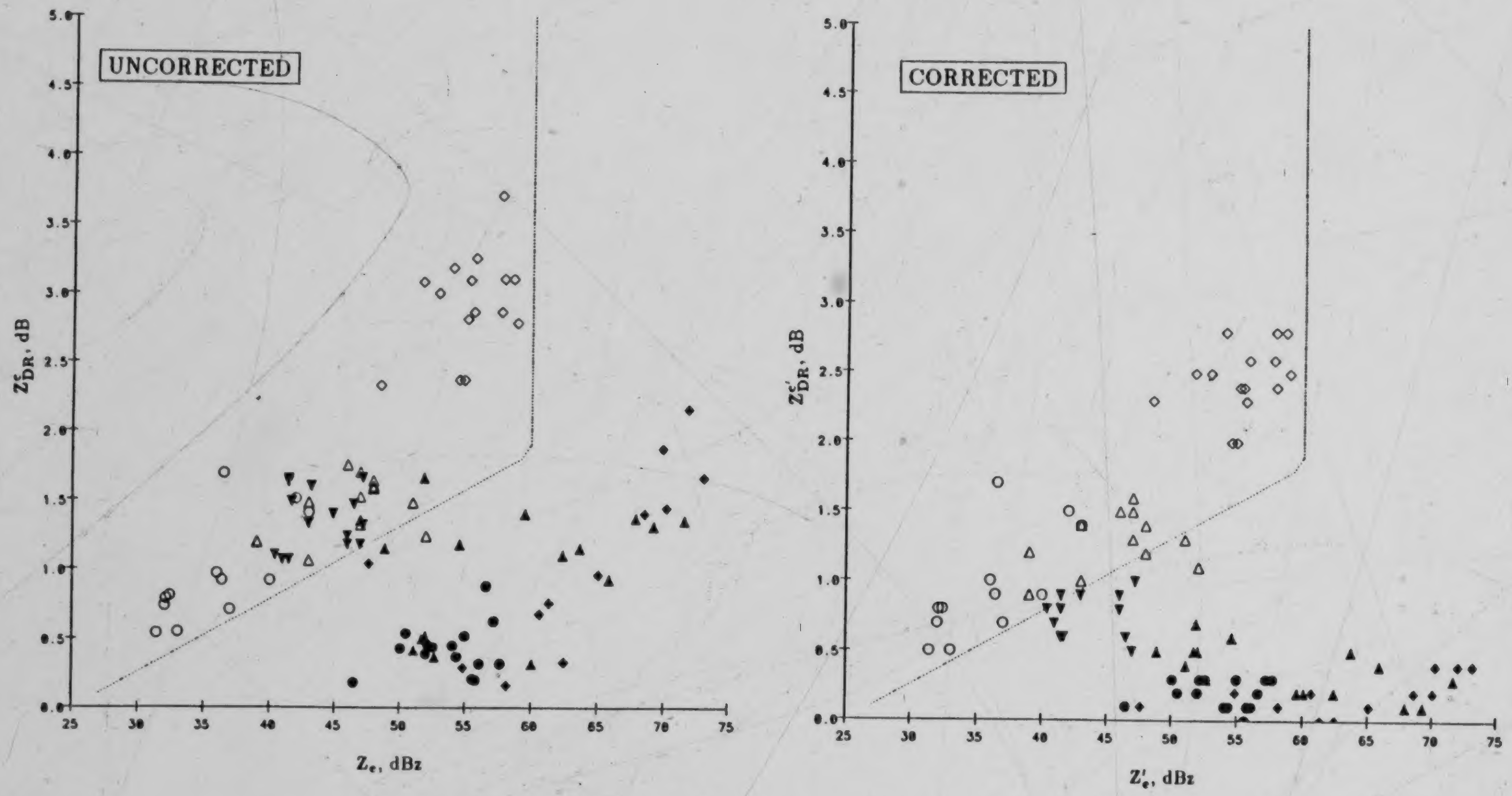

Figure 6.16 Comparison between uncorrected (left diagram) and corrected (right diagram) data for the Z_e-Z^c_{DR} relationship. See Figure 6.13 for the key to the plotted symbols.

CHAPTER VII

Verification of Polarization Techniques Using Rain and Hail Reports from Farmers

7.1 Identification Scheme and Evaluation Procedures

Results of the previous chapter indicate that polarization measurements are capable of separating rain regions from hail regions within storms and that certain combinations of polarization and reflectivity measurements are more appropriate than others for distinguishing rain from hail. $ORTT'$ and $Z_{DR}^{c'}$ provide similar information and offer much better discrimination between rain and hail than does CDR'. For these reasons, a combination of Z_e' and $Z_{DR}^{c'}$ was chosen to carry out the analysis in this chapter. This combination was based on the line dividing the rain and hail observations in Figure 6.13. Regions below the line, where the majority of the hail observations were located, were used to imply the increasing likelihood of hail whereas the regions above the line indicate rain.

To evaluate the ability of the combined Z_e' and $Z_{DR}^{c'}$ for differentiating between rain and hail regions over large areas and to ascertain whether this combination offers improvement over the use of Z_e' measurements alone, radar data and farmers' reports from three major severe storms in central Alberta were analyzed. The radar information was that obtained when the elevation angle was between 1° and

2^o. The measurements were corrected for propagation effects using the method of Bebbington *et al.* (1987) discussed in Chapter V. Farmers' reports were routinely gathered during the years of the Alberta Hail Project.

For each storm, evaluation procedures involved the following:

1. Scanning successive radar PPIs of Z_e' to determine the maximum point values during the time period of the surface reports.

2. Comparing regions in which maximum Z_e' exceeded 40 and 45 dBz to determine which of these regions best matched the surface hail pattern determined by using farmers' reports of maximum hail size. It was found that, in most cases, the maps of Z_e' greater than 45 dBz correspond to the observed surface hail regions better than those of Z_e' greater than 40 dBz. Barge (1972) has suggested that if Z_e' were to be used to discriminate between rain and hail in Alberta, a value of 44 dBz would be the most appropriate. Nevertheless, the objective of this work is to improve upon hail detection using more than Z_e'.

3. Scanning simultaneous PPIs of Z_e' and $Z_{DR}^{c'}$ to see whether the hail situations defined by the combinations of Z_e' and $Z_{DR}^{c'}$ for hail discussed above are met for a given point during the time period covered in step (1) and thereby generating a hail occurrence map which can be compared with the observed surface hail pattern.

4. Comparing the results of Z_e' alone (step 2) and those of $Z_e' - Z_{DR}^{c'}$ (step 3) to the farmers' reports by way of contingency tables. Figure 7.1 shows a standard 2×2 contingency table representing the four types of prediction-observation

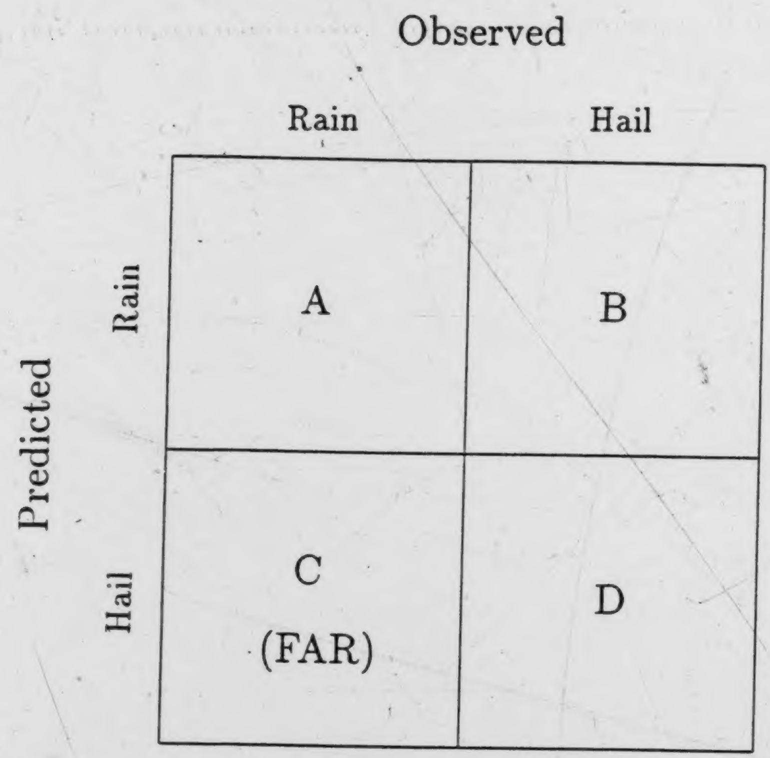

		Observed	
		Rain	Hail
Predicted	Rain	A	B
	Hail	C (FAR)	D

Figure 7.1 A 2 × 2 contingency table delineating all prediction-observation combinations that can result from comparing radar prediction to ground truth data of precipitation. Indicated are correctly predicted rain events (A), incorrectly predicted rain events (B), false alarms (C), and correctly predicted hail events (D). The false alarm rate (FAR) is defined as the ratio of the false alarms to the total surface observations of rain. FAR=C/(A+C).

combinations that can result from comparing radar predictions to ground truth observations. The method used for the evaluation defines correctly predicted rain events (A); incorrectly predicted rain events (B); false alarms, i.e., hail predicted when rain was observed at the ground, (C); and correctly predicted hail events (D). The false alarm rate (FAR) is defined as the ratio of the false alarms to the total number of surface observations of rain, i.e. $\mathrm{FAR} = \frac{C}{A+C}$.

7.2 Observations from Three Storms

24 July 1983: The first storm to be discussed developed south-west of the radar site during the evening of 24 July 1983. It produced widespread rain with a localized area of small hail. Figure 7.2a shows the maximum Z_e' map at 1.6° elevation for the time period between 2000 and 2100 MDT. Figure 7.2b maps the predicted $Z_e' - Z_{DR}^{c'}$ hail occurrences for this time period. It can be seen that the $Z_e' - Z_{DR}^{c'}$ identification scheme predicted mostly rain with relatively small regions of hail. Note that in some of the predicted rain regions, particularly near the 40 km range, Z_e' reached values of 50 to 60 dBz. At this location, only rain was observed to fall to the ground. These suggest that the combination of Z_e' and $Z_{DR}^{c'}$ correctly identified regions of rain where Z_e' exceeded the 50 dBz. In Figure 7.2c, the farmers' reports are compared to the rain and hail areas predicted by $Z_e' - Z_{DR}^{c'}$ information (left diagram) and by Z_e' alone (right diagram). It is evident that many of the rain reports were located inside the 45 dBz contour line while all the rain reports were within the rain regions of the $Z_e' - Z_{DR}^{c'}$ map. The contingency tables (see Figure 7.2d) show that, in this example, the use of Z_e' data resulted in a FAR of 55% whereas $Z_e' - Z_{DR}^{c'}$ information

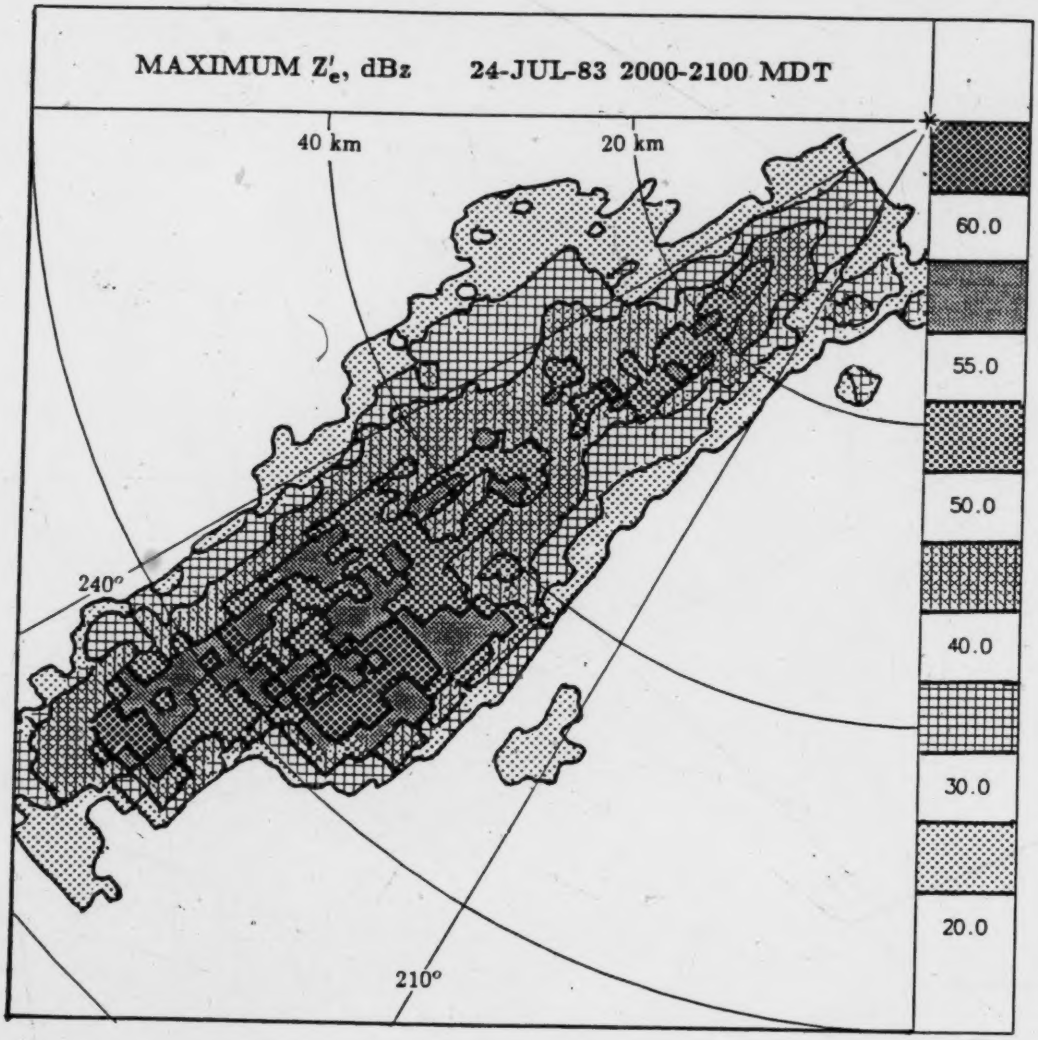
MAXIMUM Z'_e, dBz
24-JUL-83 2000-2100 MDT
40 km
20 km
240°
210°
60.0
55.0
50.0
40.0
30.0
20.0

Figure 7.2a Maximum Z'_e PPI map at 1.6° elevation for 2000-2100 MDT 24 July 1983.

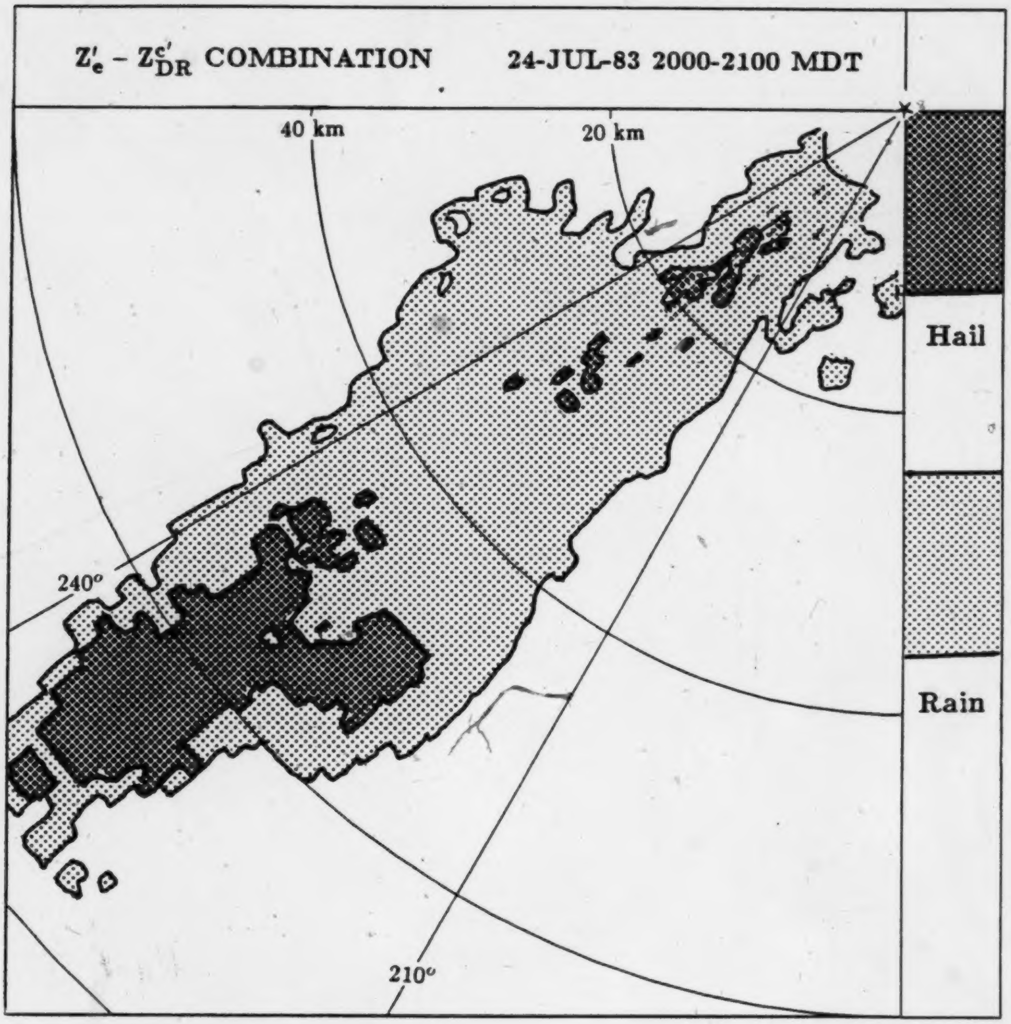
Z'_e - $Z^{c'}_{DR}$ COMBINATION
24-JUL-83 2000-2100 MDT
40 km
20 km
240°
210°
Hail
Rain

Figure 7.2b Predicted hail occurrences at 1.6° elevation for 2000-2100 MDT 24 July 1983. The map is produced by a combination of Z'_e and $Z^{c'}_{DR}$ (see text).

24 JULY 1983 2000-2100 MDT

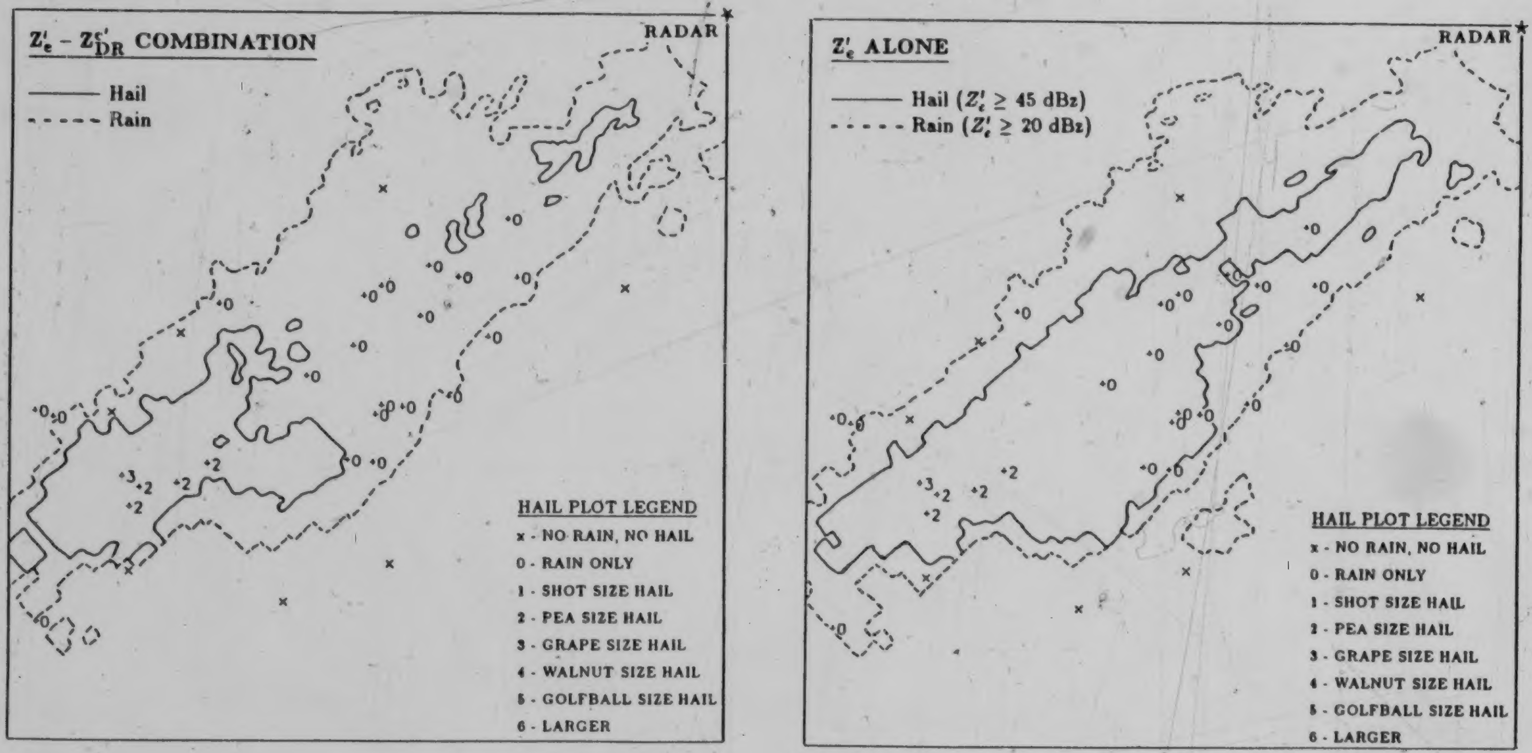
$Z'_e - Z^{c'}_{DR}$ COMBINATION
Hail
Rain
RADAR
HAIL PLOT LEGEND
x - NO RAIN, NO HAIL
0 - RAIN ONLY
1 - SHOT SIZE HAIL
2 - PEA SIZE HAIL
3 - GRAPE SIZE HAIL
4 - WALNUT SIZE HAIL
5 - GOLFBALL SIZE HAIL
6 - LARGER
Z'_e ALONE
Hail ($Z'_e \geq 45$ dBz)
Rain ($Z'_e \geq 20$ dBz)
RADAR
HAIL PLOT LEGEND
x - NO RAIN, NO HAIL
0 - RAIN ONLY
1 - SHOT SIZE HAIL
2 - PEA SIZE HAIL
3 - GRAPE SIZE HAIL
4 - WALNUT SIZE HAIL
5 - GOLFBALL SIZE HAIL
6 - LARGER

Figure 7.2c Surface observations of precipitation for 24 July 1983 compared to outlines of rain regions (dashed lines) and hail regions (solid lines) predicted by a combination of Z'_e and $Z^{c'}_{DR}$ (left diagram) and by Z'_e (right diagram). See Figure 7.2b for the map scale.

Rain-Hail Identification Criterion

		Observed at the ground	
		Rain	Hail
Predicted by the radar	Rain	20	0
	Hail	0 (0%)	5

$Z_e' - Z_{DR}^{c'}$ combination (see text)

……

		Observed at the ground	
		Rain	Hail
Predicted by the radar	Rain	9	0
	Hail	11 (55%)	5

$Z_e' \geq 45$ dBz Hail

$Z_e' \geq 20$ dBz Rain

Figure 7.2d Contingency tables for the 24 July 1983 storm showing that the combination of Z_e and $Z_{DR}^{c'}$ resulted in a false alarm rate of 0% whereas Z_e' produced a false alarm rate of 55%.

gave a FAR of 0%. This indicates that the simultaneous Z_e' and $Z_{DR}^{c'}$ data offer a big improvement over Z_e' for identifying rain events in regions where Z_e' exceeded 50 dBz. The few hail observations were located at the far side of the storm. At this location, hail was predicted by both Z_e' and $Z_e' - Z_{DR}^{c'}$ data. However, this case study was selected on the basis that mostly rain was reported at the ground. The following example will illustrate the situation where hail was observed over a large area.

15 August 1983: On this date, two major hailstorms developed in mid-afternoon due south-west of the radar site. They intensified as they moved eastward and eventually merged together to form a large storm. Two distinct hail swaths oriented in an east-west direction resulted from these storms. Figures 7.3a and 7.3b show the maximum Z_e' map and the corresponding $Z_e' - Z_{DR}^{c'}$ hail occurrences map for an elevation angle of 1.3° and for a time period between 1500 and 1800 MDT. Figure 7.3c illustrates the surface reports compared to the regions of rain and hail predicted by $Z_e' - Z_{DR}^{c'}$ (left diagram) and by Z_e' (right diagram). It is apparent that the $Z_e' - Z_{DR}^{c'}$ map delineates the surface observations of rain and hail better than the Z_e' map, especially in the areas close to the radar where near perfect agreement can be seen. Moreover, most of the disagreement points, i.e., rain reports located inside predicted hail regions, were situated very close to the contour line separating the hail and rain regions. The results are summarized in Figure 7.3d, they indicate that the combined Z_e' and $Z_{DR}^{c'}$ were capable of distinguishing rain from hail. For instance, in hail regions 83 of 85 reports were hail reports while only 16 of 61

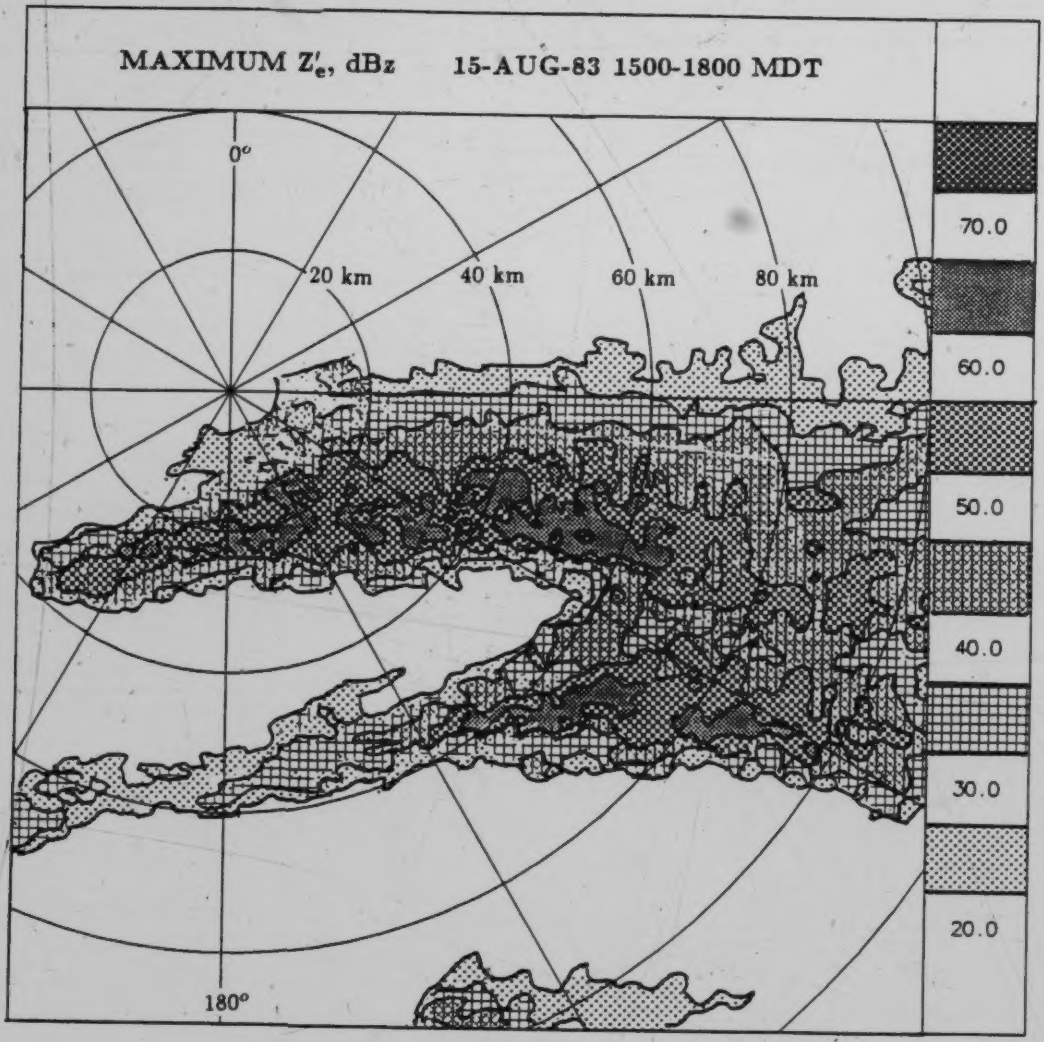
MAXIMUM Z'e, dBz
15-AUG-83 1500-1800 MDT
0°
20 km
40 km
60 km
80 km
180°
70.0
60.0
50.0
40.0
30.0
20.0

Figure 7.3a Maximum Z_e' PPI map at 1.3° elevation for 1500-1800 MDT 15 August 1983.

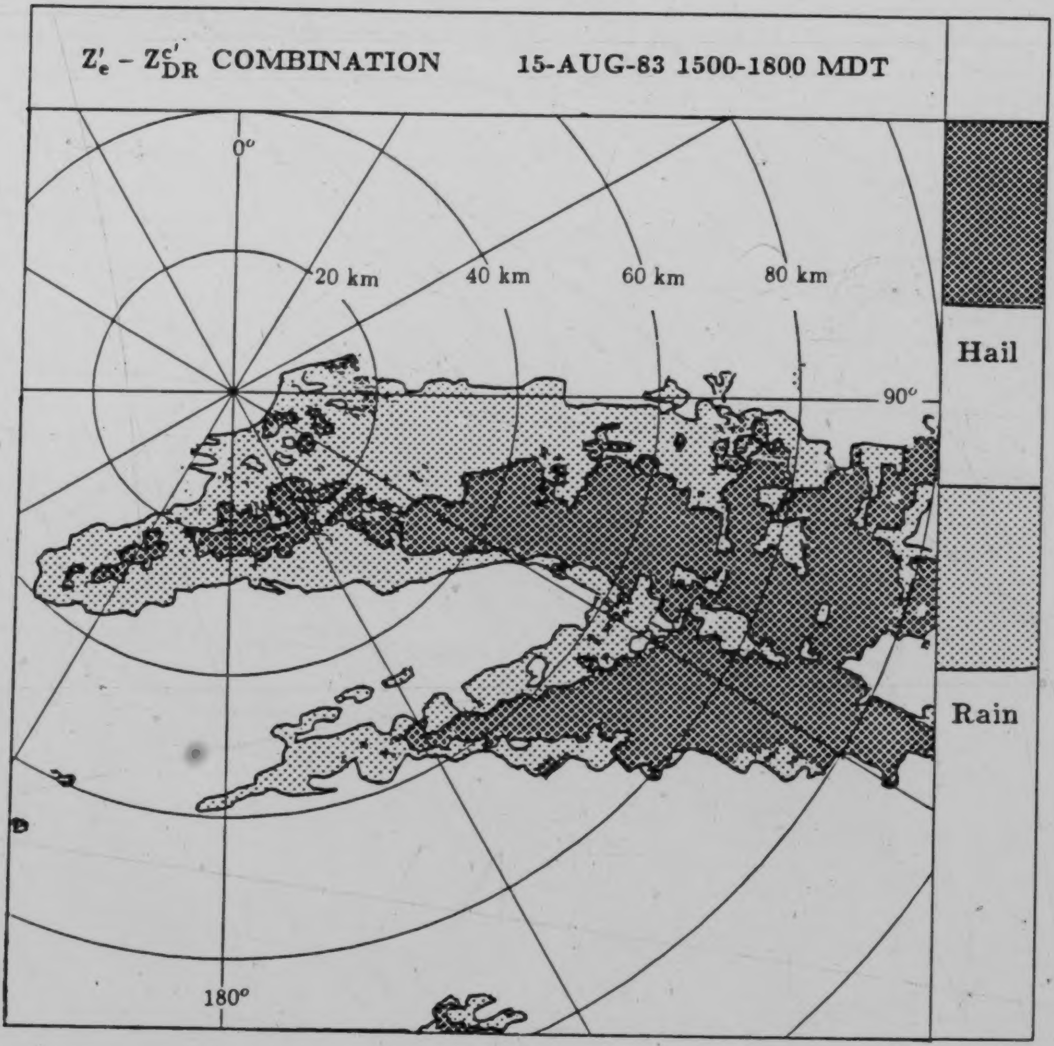
Z'e - Zc'DR COMBINATION
15-AUG-83 1500-1800 MDT
0°
20 km
40 km
60 km
80 km
90°
180°
Hail
Rain

Figure 7.3b Predicted hail occurrences at 1.3° elevation for 1500-1800 MDT 15 August 1983. The map is produced by a combination of Z'_e and $Z^{c'}_{DR}$ (see text).

15 AUGUST 1983 1500-1800 MDT

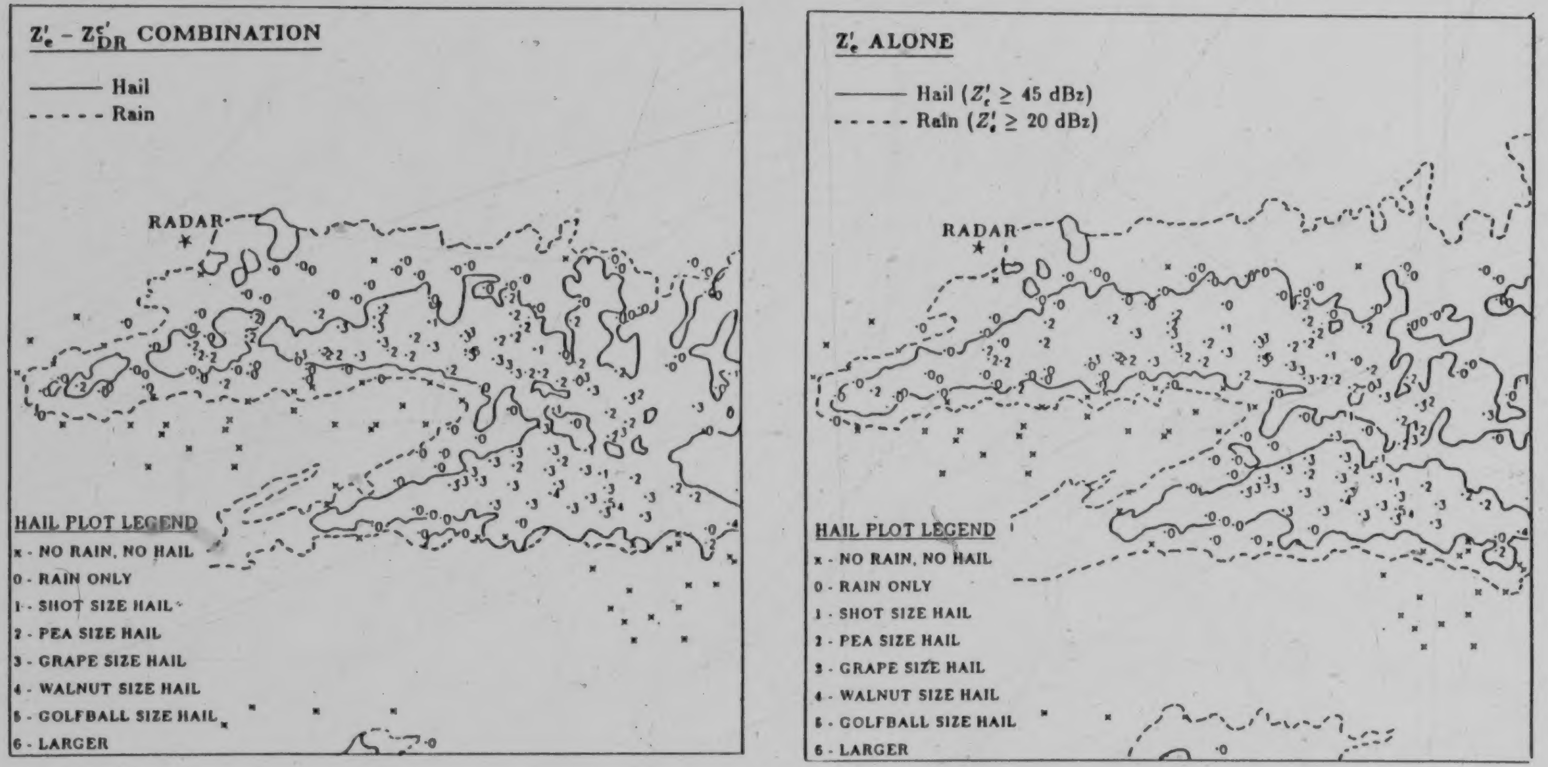
$Z'_e - Z^{c'}_{DR}$ COMBINATION
—— Hail
- - - - Rain
RADAR
HAIL PLOT LEGEND
x - NO RAIN, NO HAIL
0 - RAIN ONLY
1 - SHOT SIZE HAIL
2 - PEA SIZE HAIL
3 - GRAPE SIZE HAIL
4 - WALNUT SIZE HAIL
5 - GOLFBALL SIZE HAIL
6 - LARGER
Z'_e ALONE
—— Hail ($Z'_e \geq 45$ dBz)
- - - - Rain ($Z'_e \geq 20$ dBz)
RADAR
HAIL PLOT LEGEND
x - NO RAIN, NO HAIL
0 - RAIN ONLY
1 - SHOT SIZE HAIL
2 - PEA SIZE HAIL
3 - GRAPE SIZE HAIL
4 - WALNUT SIZE HAIL
5 - GOLFBALL SIZE HAIL
6 - LARGER

Figure 7.3c Surface observations of precipitation for 15 August 1983 compared to outlines of rain regions (dashed lines) and hail regions (solid lines) predicted by a combination of Z'_e and $Z^{c'}_{DR}$ (left diagram) and by Z'_e (right diagram). See Figure 7.3b for the map scale.

Rain-Hail Identification Criterion

		Observed at the ground	
		Rain	Hail
Predicted by the radar	Rain	45	2
	Hail	**16** (26%)	83

$Z'_e - Z^{c'}_{DR}$ combination (see text)

……

		Observed at the ground	
		Rain	Hail
Predicted by the radar	Rain	27	3
	Hail	**34** (56%)	82

$Z'_e \geq 45$ dBz Hail

$Z'_e \geq 20$ dBz Rain

Figure 7.3d Contingency tables for the 15 August 1983 storm showing that the combination of Z_e and $Z^{c'}_{DR}$ resulted in a false alarm rate of 26% whereas Z'_e produced a false alarm rate of 56%.

(FAR=26%) were rain reports. As mentioned above, many of the 16 false alarms were located very close to the predicted rain regions. In the Z_e' map, 34 of the 61 rain reports were located inside the 45 dBz contour line (FAR=56%), suggesting that the use of the combined Z_e' and $Z_{DR}^{c'}$ data differentiates between rain and hail much better than that of Z_e' alone.

5 July 1984: On the evening of 5 July 1984, an intense storm formed north to north-east of the radar site. The storm produced a mixture of heavy rain and hail. Figure 7.4a presents the maximum Z_e' map for an elevation angle of 1.1° and for a time period between 1800 and 2000 MDT. The contoured regions of Z_e' above 50 dBz extended over significantly large areas (about 1200 km^2). The rain and hail regions predicted by simultaneous measurements of Z_e' and $Z_{DR}^{c'}$ are shown in Figure 7.4b. As expected, the largest hail (grape size shown in Figure 7.4c) was associated with the most intense portion of the storm where Z_e' was greater than 60 dBz. Of greater interest is the fact that rain regions were predicted within areas of Z_e' between 50 and 60 dBz and that no hail was observed under these predicted rain regions. Figure 7.4c compares the ground truth data to the rain and hail regions delineated by the $Z_e' - Z_{DR}^{c'}$ and Z_e' alone. Clearly, the hail regions of the $Z_e' - Z_{DR}^{c'}$ map correlate with the observed surface hail pattern much better than the hail regions of the Z_e' map. In fact, the contingency tables of Figure 7.4d indicate that only 3 of 61 rain observations were within the hail regions of the $Z_e' - Z_{DR}^{c'}$ map (FAR=6%) while 21 of these rain reports were inside the contour line of 45 dBz (FAR=45%).

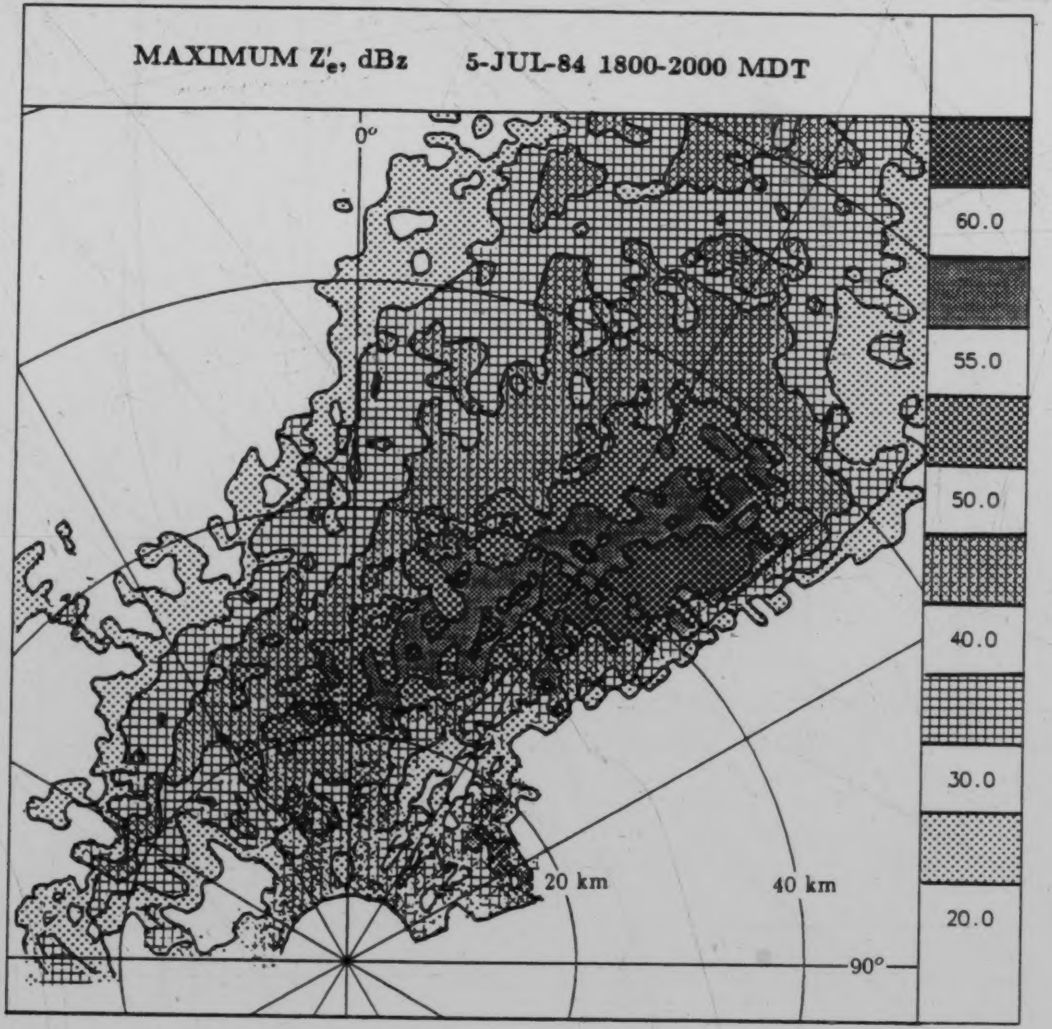
MAXIMUM Z'_e, dBz 5-JUL-84 1800-2000 MDT
0°
20 km
40 km
90°
60.0
55.0
50.0
40.0
30.0
20.0

Figure 7.4a Maximum Z'_e PPI map at 1.1° elevation for 1800-2000 MDT 5 July 1984.

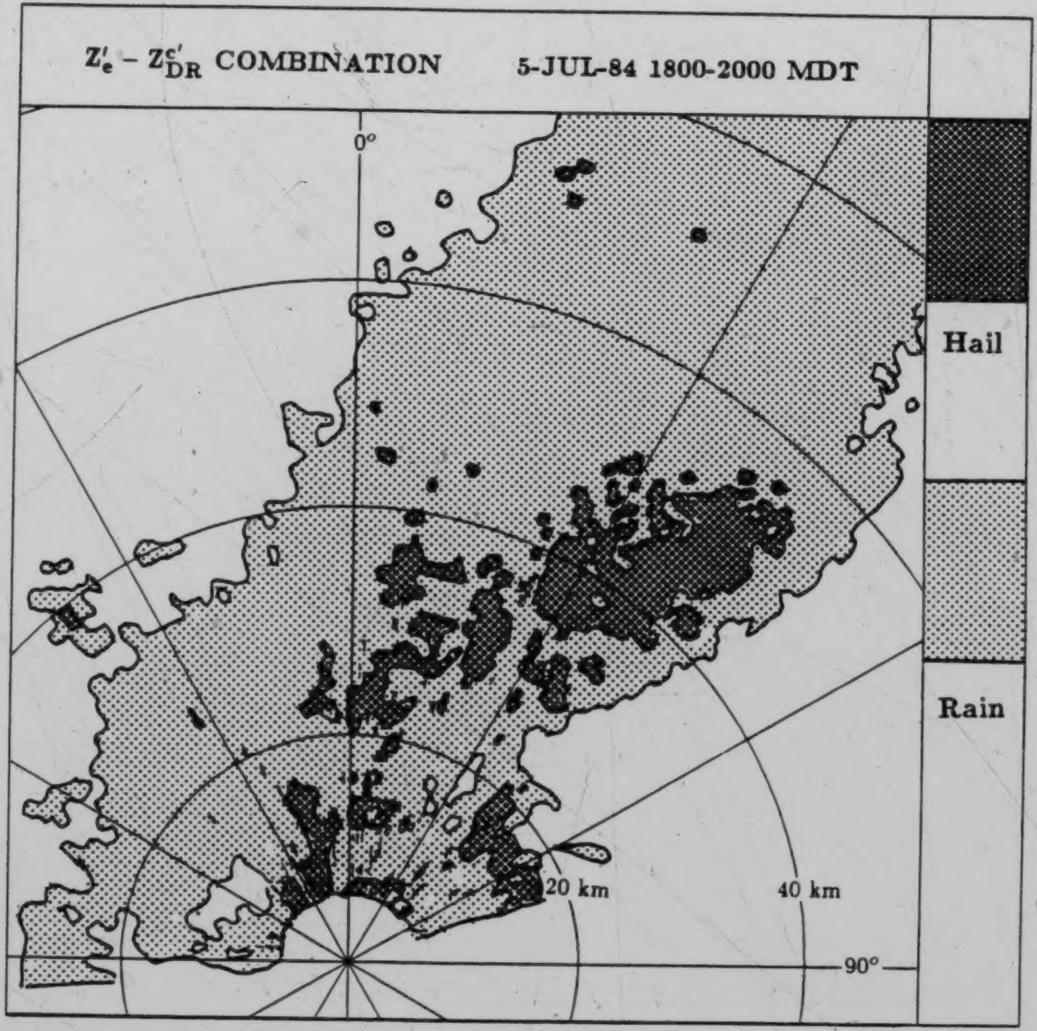
$Z'_e - Z^{c'}_{DR}$ COMBINATION
5-JUL-84 1800-2000 MDT
0°
Hail
Rain
20 km
40 km
90°

Figure 7.4b Predicted hail occurrences at 1.1° elevation for 1800-2000 MDT 5 July 1984. The map is produced by a combination of Z'_e and $Z^{c'}_{DR}$ (see text).

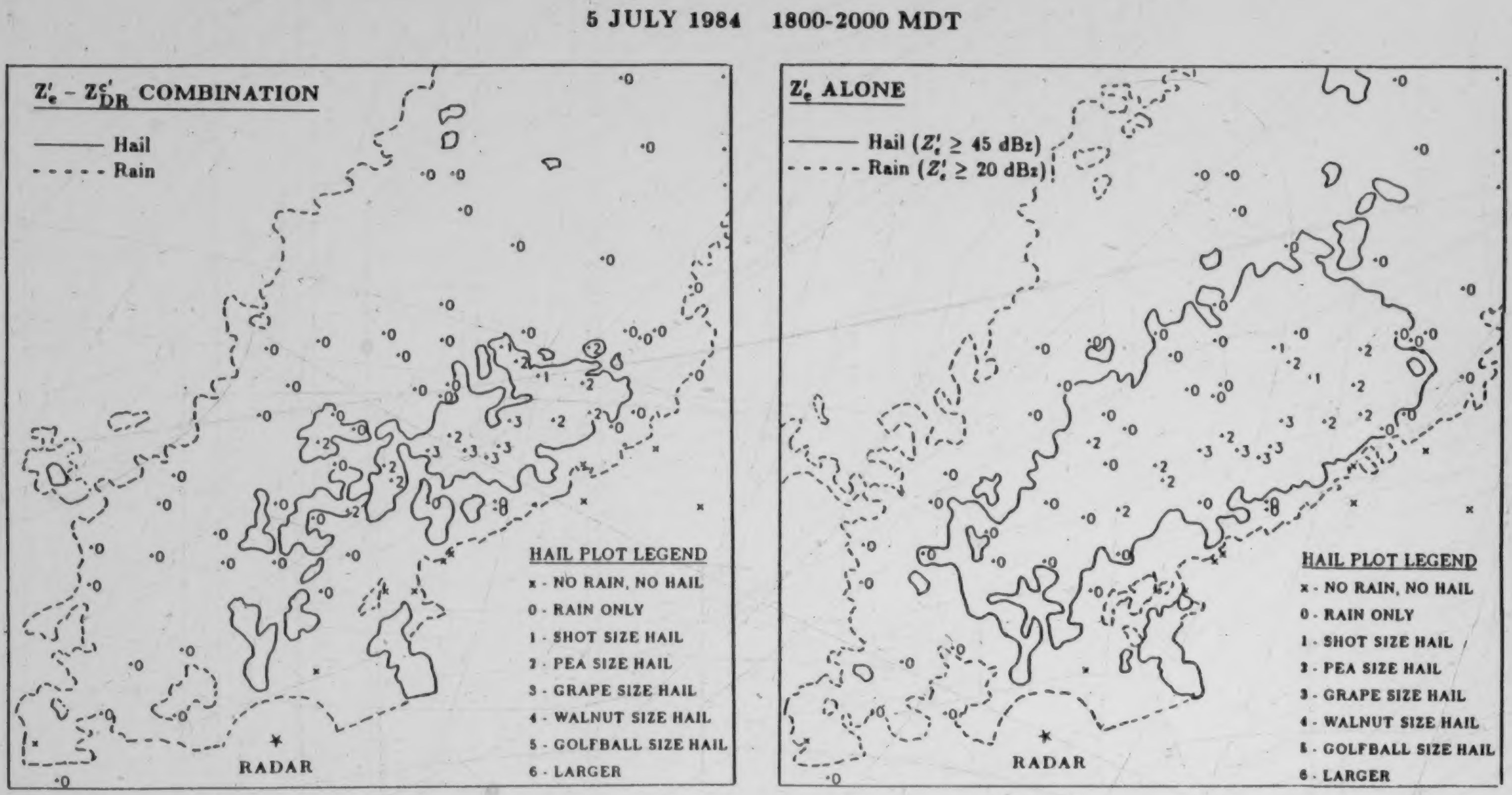
5 JULY 1984 1800-2000 MDT
$Z_e' - Z_{DR}^{c'}$ COMBINATION
Hail
Rain
Z_e' ALONE
Hail ($Z_e' \geq 45$ dBz)
Rain ($Z_e' \geq 20$ dBz)
HAIL PLOT LEGEND
x - NO RAIN, NO HAIL
0 - RAIN ONLY
1 - SHOT SIZE HAIL
2 - PEA SIZE HAIL
3 - GRAPE SIZE HAIL
4 - WALNUT SIZE HAIL
5 - GOLFBALL SIZE HAIL
6 - LARGER
RADAR

Figure 7.4c Surface observations of precipitation for 5 July 1984 compared to outlines of rain regions (dashed lines) and hail regions (solid lines) predicted by a combination of Z_e' and $Z_{DR}^{c'}$ (left diagram) and by Z_e' (right diagram). See Figure 7.4b for the map scale.

Rain-Hail Identification Criterion

		Observed at the ground	
		Rain	Hail
Predicted by the radar	Rain	44	0
	Hail	**3** (6%)	17

$Z_e' - Z_{DR}^{c'}$ combination (see text)

……

		Observed at the ground	
		Rain	Hail
Predicted by the radar	Rain	26	0
	Hail	**21** (45%)	17

$Z_e' \geq 45$ dBz Hail

$Z_e' \geq 20$ dBz Rain

Figure 7.4d Contingency tables for the 5 July 1984 storm showing that the combination of Z_e and $Z_{DR}^{c'}$ resulted in a false alarm rate of 6% whereas Z_e' produced a false alarm rate of 45%.

In summary, the radar information and the farmers' reports of precipitation for the three severe storms show that combined Z_e' and $Z_{DR}^{c'}$ can more accurately distinguish rain regions from hail regions within storms. The false alarms resulting from this technique were remarkably low when compared with those obtained from measurements using solely Z_e'. Polarization diversity radar measurements clearly provide more reliable information about the type of precipitation than do measurements of reflectivity alone.

CHAPTER VIII

Summary and Conclusions

This research set out to improve detection of and discrimination between rain and hail by comparing polarization diversity radar measurements to ground-based precipitation observations.

To assure accuracy and consistency in the analysis, an algorithm was developed to determine the radar calibration constants required to extract, from the recorded raw data, the correlation and phase angle between the two orthogonal components of the received signal. Careful examination of the calibration data showed that the correlation channels have slightly different phase and gain characteristics and that differences between successive calibrations over four summers were not significant.

Propagation effects on the S-band circularly polarized radar were considered to illustrate the relative sensitivity of various radar parameters to these effects and to test the correction procedures of Bebbington *et al.* (1987) and Jameson and Davé (1988). Theoretical calculations carried out for a 10 km long uniform rain-filled path suggested that propagation effects depend on the rainfall rate and the distance through rain. These effects were shown to seriously corrupt the circular depolarization ratio. The influence on the correlation and orientation angle is to increase them nearer to 100% and 45° respectively. Consequently, the differential reflectivity derived from these circular polarization parameters is also severely affected. The effect on the equivalent reflectivity factor using the S-band radar is detectable only at very heavy rainfall rates. Application of the two correction procedures to the calculations of propagation effects indicated that these effects can be removed and need no longer restrict the use of circular polarization measurements for meteorological research. The results also showed that the correction methods provide essentially identical information. This is probably because both methods are based on similar assumptions such as that propagation effects are entirely due to differential phase shift (differential attenuation is negligible) and any deviation in the phase angle from 0° values is attributed to differential phase shift. In other words, both methods use the phase angle to correct the other parameters. These theoretical findings were confirmed by observations of severe propagation effects selected from the Alberta Research Council's S-band radar archives. In this work, the correction method of Bebbington *et al.* (1987) has been adopted.

Radar measurements were compared with well-documented and carefully timed ground observations of precipitation. These case studies included light rain, heavy rain, and various mixtures of rain and hail. To observe precipitation as close as possible to the ground surface, radar information was obtained when the antenna elevation angle was between 1° and 2°. The theoretical models of Torlaschi *et al.* (1984) were used to help interpret the radar data. The results of the analysis suggested that storm cells which produce significant hailfall nearly always result in different measurements than storm cells which produce only rain. Furthermore, in rain regions the polarization parameters are well correlated with the reflectivity factor. This is expected, since an increase in reflectivity usually corresponds to an increase in rainfall rate. The larger raindrops associated with increased rainfall rates are necessarily more oblate and tend to fall with their minor axes vertical (preferred orientation) and the polarization parameters also increase. In the transition from rain regions to regions containing hail and as the hailstones develop sizes larger than those of raindrops, the reflectivity factor increases while the irregular shapes and tumbling motion (random orientation) of the hailstones result in low readings of the polarization parameters. The results also indicated that the rain and hail signatures of the differential reflectivity derived from circular polarization quantities were highly consistent with those determined in other studies using linear polarization measurements (e.g., Bringi *et al.*, 1984; Aydin *et al.* 1986). This suggests that circular and linear polarization techniques are compatible. It is important to point out that the correction for propagation effects was very effective in obtaining a better correlation between radar measurements and ground truth data.

Relationships between the reflectivity factor and various polarization parameters illustrated that the correlation and differential reflectivity were closely related and both offered better discrimination between rain and hail than the circular depolarization ratio provided that propagation effects are removed from the measurements. The data also suggested that certain combinations of reflectivity factors and polarization measurements can be used to discriminate between rain and hail. A scheme for the remote identification of rain and hail was developed. The method was based on a combination of reflectivity and differential reflectivity. Radar data and farmers' surface observations collected over large areas for the storm's time period were used to confirm the method. It was found that, in most cases, hail regions predicted by the combined reflectivity and differential reflectivity data were much better correlated with the surface hail pattern than hail regions predicted using reflectivity alone. This demonstrated that polarization diversity radar provides an effective and reliable means to discriminate between rain and hail.

While the results of this research represent a significant achievement, there remain many areas to be investigated. The rain and hail identification scheme developed in this study might be revised so that a third parameter, such as correlation or circular depolarization ratio, can be included to see whether this would prove more helpful in discriminating between rain and hail; it could possibly determine the proportions of hail to rain and their individual precipitation rates. Further research should be conducted on the relationship between circular and linear polarization measurements to assess which can provide the best information and of what parameters. This would give insight into the cost effectiveness of the two systems. Another analysis could be carried out to compare radar and research aircraft measurements to study the nature, growth process, and vertical extent of hailstorms, especially before and after cloud seeding operations. This is expected to be a useful means for evaluating hail suppression operations.

The ground-based precipitation observations used in this study, along with the radar observations, have shown in a more detailed way than previously reported that most recent theories on polarization diversity radar are correct and highly applicable to the study of thunderstorms and thunderstorm modification.

Bibliography

Al-Jumily, K.J., Humphries, R.G., and Phillips L.D., 1986: Discrimination between rain and hail with polarization diversity radar. *Proc. 23rd Conf. Radar Meteorology*, Snowmass, Amer. Meteo. Soc., 70-73.

Antar, Y.M.M., and A. Hendry, 1987: Correlation techniques in two-channel linearly polarized radar systems. *Electromagnetics*, **7**, 17-27.

Atlas, D., M. Kerker and W. Hitschfeld, 1953: Scattering and attenuation by non-spherical atmospheric particles. *J. Atmos. and Terrest. Phys.*, **3**, 108-119.

Aydin, K., T.A. Seliga and V.N. Bringi, 1984: Differential radar scattering properties of model hail and mixed-phase hydrometeors. *Radio Sci.*, **19**, 58-66.

Aydin, K., T.A. Seliga and V. Balaji, 1986: Remote sensing of hail with a dual linear polarization radar. *J. Clim. Appl. Meteor.*, **25**, 1475-1484.

Azzam R.M.A., and N.M. Bashara, 1977: Ellipsometry and Polarized Light. North-Holland Publishing Company. Amsterdam.

Barge, B.L., 1972: Hail detection with a polarization diversity radar. Sci. Rep. MW-71, Stormy Weather Group, McGill University, Montreal, Canada, 80 pp.

Barge, B.L., 1974: Polarization measurements of precipitation backscatter in Alberta. *J. Rech. Atmos.*, **8**, 163-173.

Barge, B.L., and G.A. Isaac, 1973: The shape of Alberta hailstones. *J. Rech. Atmos.*, **7**, 11-20.

Barge, B.L., R.G. Humphries and M.R. Johnson, 1976: Alberta hail radar-computer consideration. Atmospheric Sciences Division Report 76-1, Alberta Research Council, Edmonton, Alberta, Canada, 45-67.

Barge, B.L., and R.G. Humphries, 1980: Identification of rain and hail with polarization and dual-wavelength radar. *Proc. 19th Conf. Radar Meteorology*, Miami, Amer. Meteo. Soc., 507-516.

Battan, L.J., 1973: Radar Observation of the Atmosphere. The University of Chicago press, Chicago.

Beard, K.V., and A.R. Jameson, 1983: Raindrop canting. *J. Atmos. Sci.*, **40**, 448-454.

Bebbington, D.H.O., R. McGuinness and A.R. Holt, 1987: Correction of propagation effects in S-band circular polarization-diversity radars. *IEE Proc., Part H, Microwave, Antennas, and Propagation*, **134**, 431-437.

Beckman, P., 1968: The Depolarization of Electromagnetic Waves. Golem Press, Boulder, Colorado.

Born, M., and E. Wolf, 1964: Principles of Optics. 2nd ed., McMillan, New York, 808 pp.

Bringi, V.N., V. Chandresekhar, T.A. Seliga, P.L. Smith and T. Hari, 1983: Analysis of differential reflectivity (Z_{DR}) radar measurements during the cooperative convective precipitation experiment. *Proc. 21st Conf. Radar Meteorology,* Edmonton, Amer. Meteor. Soc., 494-499.

Bringi, V.N., T.A. Seliga and K. Aydin. 1984: Hail detection with a differential reflectivity radar. *Science*, **225**, 1145-1147.

Browne, I.C., and N.P. Robinson. 1952: Cross-polarization of the radar melting band. *Nature*, **170**, 1078-1079.

Cheng, L., and M. English, 1983: A relationship between hailstone concentration and size. *J. Atmos. Sci.*, **40**, 204-213.

Cook, B., 1958: Hail determination by radar analysis. *Mon. Wea. Rev.*, **86**, 435-438.

Crispin, J.W., Jr., and K.M. Siegel, 1968: Method of Radar Cross-section Analysis. Academic Press Inc., New York and London, 426 pp.

Donaldson, R.J., Jr., 1961: Radar reflectivity profiles in thunderstorms. *J. Meteor.*, **18**, 292-305.

Douglas, R.H., and W. Hitschfeld, 1958: Studies of Alberta hailstorms. Sci. Rep. MW-27, Stormy Weather Group, McGill University, Montreal, Canada, 79 pp.

Gans, R., 1912: Über die Form Ultramikroskopischer Goldteilchen (On the form of ultra-microscopic gold particles). *Ann. Phys.*, **37**, 881-900.

Gent, H., I.M. Hunter and N.P. Robinson, 1963: Polarization of radar echoes, including aircraft, precipitation, and terrain. *IEE Proc.*, **110**, 2139-2148.

Geotis, S.G., 1963: Some radar measurements of hailstorms. *J. Appl. Meteor.*, **2**, 270-275.

Gershenzon, Yu.M., and A.B. Shupiatskii, 1961: Scattering of elliptically polarized radio waves by non-spherical atmospheric particles. *Tsenral'naia Aerologicherkaia Observatoriia*, Trudy, **No. 36**, 102-118.

Goddard, J.W.F., S.M. Cherry, and V.N. Bringi, 1982: Comparison of dual-polarization radar measurements of rain with ground-based disdrometer measurements. *J. Appl. Meteor.*, **21**, 252-256.

Goddard, J.W.F., and S.M. Cherry, 1984: The ability of dual polarization radar (copolar linear) to predict rainfall rate and microwave attenuation. *Radio Sci.*, **19**, 201-208.

Hall, M.P.M., S.M. Cherry, J.W.F. Goddard and G.R. Kennedy, 1980: Raindrop size and rainfall rate measured by dual-polarization radar. *Nature*, **285**, 195-198.

Hendry, A., and G.C. McCormick, 1971: Polarization properties of polarization scattering. Quart. Bull. of Radio and Electrical Engineering Division, National Research Council of Canada, **21**, 9-20.

Hendry, A., G.C. McCormick and B.L. Barge, 1976: The degree of common orientation of hydrometeors observed by polarization diversity radars. *J. Appl. Meteor.*, **15**, 633-640.

Hendry, A. and Y.M.M. Antar, 1984a: Precipitation particle identification with centimeter wavelength dual-polarization radars. *Radio Sci.*, **19**, 115-122.

Hendry, A., and Y.M.M. Antar, 1984b: Comparison of circular and linear polarization radar measurements on the melting layer. *Electron Lett.*, **20**, 419-420.

Hendry, A., Y.M.M. Antar and G.C. McCormick, 1986: On the relationship between the degree of preferred orientation in precipitation and dual- polarization radar echo characteristics. *Radio Sci.*, **22**, 37-50.

Holt, A.R., 1984: Some factors affecting the remote sensing of rain by polarization diversity radar in the 3 to 35 GHz frequency range. *Radio Sci.*, **19**, 1399-1412.

Humphries, R.G., 1974a: Depolarization effects at 3 GHz due to precipitation. Sci. Rep. MW-82, Stormy Weather Group, McGill University, Montreal, Canada, 81 pp.

Humphries, R.G., 1974b: Observations and calculations of depolarization effects at 3 GHz due to precipitation. *J. Rech. Atmos.*, **8**, 156-161.

Humphries, R.G., B.L. Barge and M.R. Johnson, 1977: Alberta Hail Radar-Computer Considerations II, Atmospheric Sciences Division Report 77-3, Alberta Research Council, Edmonton, Alberta, Canada.

Humphries, R.G., and B.L. Barge, 1979: Polarization and dual-wavelength radar observations of the bright band. *IEEE Trans. Geosci. Electron.*, GE-17, 190-195.

Hunter, I.M., 1954: Polarization of radar echoes from meteorological precipitation. *Nature*, **173**, 165-166.

Illingworth, A.J., J.W.F. Goddard and S.M. Cherry, 1986: Detection of hail by dual-polarization radar. *Nature*, **320**, 431-433.

Jameson, A.R., 1987: Relations among linear and circular polarization parameters measured in canted hydrometeors. *J. Atmos. Oceanic. Technol.*, **4**, 634-645.

Jameson, A.R., and J.H. Davé, 1988: An interpretation of circular polarization measurements affected by propagation differential phase shift. *J. Atmos. Oceanic. Technol.*, **5**, 405-415.

Kerker, M., and W. Hitschfeld. 1950: Particle shape and secondary scattering on microwave reflections from clouds and precipitation. Sci. Rep. MW-1, Stormy Weather Group, McGill University, Montreal, Canada, 32 pp.

Ko, H.C., 1962: On the reception of quasi-monochromatic partially polarized radio waves. *IRE Proc.*, **50**, 1950-1957.

Kraus, J.D., and K.R. Carver, 1973: Electromagnetics. McGraw-Hill, New York.

Labrum, N.R., 1952: The scattering of radio waves by meteorological particles. *J. Appl. Phys.*, **23**, 1324-1330.

Leitao, M.J., and P.A. Watson, 1984: Application of dual-linearly polarized radar data to prediction of microwave path attenuation at 10-30 GHz. *Radio Sci.*, **19**, 209-221.

Leung, S.K., 1976: The Alberta Hail Project Radar Systems. Atmospheric Sciences Division Report 77-4, Alberta Research Council, Edmonton, Alberta, Canada, 153 pp.

Marshall, J.S., and W.McK. Palmer, 1948: The distribution of raindrops with size, *J. Meteor.*, **5**, 165-166.

Marshall, J.S., and W.E. Gordon, 1957: Radiometeorology. Meteor. Monographs, 3, 73-113.

Mason, B.J., 1971: The Physics of Clouds. Clarendon, Oxford, 671 pp.

McCormick, G.C., 1968: An antenna for obtaining polarization-related data with the Alberta Hail Radar. *Proc. 13th Conf. Radar Meteorology*, Montreal, Amer. Meteor. Soc., 340-347.

McCormick, G.C., and A. Hendry, 1970: The study of precipitation backscatter at 1.8 cm with a polarization diversity radar. *Proc. 14th Conf. Radar Meteorology*, Tucson, Amer. Meteor. Soc., 225-230.

McCormick, G.C., and A. Hendry, 1972: Results of precipitation backscatter measurements at 1.8 cm with a polarization diversity radar. *Proc. 15th Conf. Radar Meteorology*, Champaign-Urbana, Amer. Meteor. Soc., 35-38.

McCormick, G.C., A. Hendry and B.L. Barge, 1972: The anisotropy of precipitation medium. *Nature*, **238**, 214-216.

McCormick, G.C., 1975: Propagation through a precipitation medium: theory and measurements. *IEEE Trans. Antennas and Propagation*, **AP-23**, 266-269.

McCormick, G.C., and A. Hendry, 1975: Principles for the determination of the polarization properties of precipitation. *Radio Sci.*, **10**, 421-434.

McCormick, G.C., and A. Hendry, 1976: Polarization-related parameters for rain: Measurements obtained by radar. *Radio Sci.*, **11**, 731-740.

McCormick, G.C., 1979: Relationship of differential reflectivity to correlation in dual-polarization radar.*Electron. Lett.*, **15**, 265-266.

McCormick, G.C., and A. Hendry, 1979: Techniques for the determination of the polarization properties of precipitation. *Radio Sci.*, **14**, 1027-1040.

McGuinness, R., D.H.O. Bebbington and A.R. Holt, 1987: Modelling propagation effects in the use of S-band polarization diversity radars. *IEE Proc., Part H, Microwaves, Antenna, and Propagation*, **134**, 423-430.

Metcalf, J.I., 1980: Theory and experimental concepts for coherent polarization-diversity meteorological radar. Final report, Project B-529. Engineering experiment station. Georgia Inst. Tech., 88 pp.

Metcalf, J.I., 1981: Propagation effects on a coherent polarization diversity radar. *Radio Sci.*, **16**, 1373-1383.

Morganov, S.P., and A.P. Shupiatskii, 1964: Evaluation of artificial-modification efficiency from the polarization characteristics of echo signal. *Tr. Tsent. Aerol. Observ.*, **No. 57**, 49-54.

Morrison, J.A., M.J. Cross and T.S. Chu, 1973: Rain-induced differential attenuation and differential phase shift of microwave frequencies. *Bell System Tech. J.*, **52**, 599-608.

Mott, H., 1986: Polarization in Antennas and Radar. John Wiley & Sons. New York.

Newell, R.E., S.G. Geotis, M.L. Stone and A. Fleisher, 1955: How round are raindrops? *Proc. 5th Weather Radar Conf.*, Fort Monmouth, Amer. Meteor. Soc., 261-268.

Newell, R.E., S.G. Geotis and A. Fleisher, 1957: The shape of rain and snow at microwavelengths. MIT Weather Radar Research Rep., No. 28, 103 pp.

Oguchi, T., 1960: Attenuation of electromagnetic wave due to rain with distorted raindrops. *J. Radio Res. Lab.*, **7**, 467-485.

Oguchi, T., 1964: Attenuation of electromagnetic wave due to rain with distorted raindrops (Part II). *J. Radio Res. Lab.*, **11**, 19-43.

Oguchi, T., 1966: Scattering and absorption of millimeter wave due to rain and melting hailstones. *J. Radio Res. Lab.*, **13**, 141-147.

Oguchi, T., 1983: Electromagnetic wave propagation and scattering in rain and other hydrometeors. *Proc. IEEE*, **71**, 1029-1078.

Pell, J., 1969: The Alberta hailstorm as observed on the ground and by radar. Ph. D. thesis, McGill University, Montreal, Canada, 298 pp.

Peter, T.V., 1966: The polarization of radar returns from rain. *Trans. South African Inst. Elec. Engr.*, Nov., 234-250.

Pruppacher, H.R., and R.L. Pitter, 1971: A semi-empirical determination of the shape of cloud and raindrops. *J. Atmos. Sci.*, **28**, 86-94.

Roos, D. v.d. S., and A.E. Carte, 1973: The falling behaviour of oblate and spiky hailstones. *J. Rech. Atmos.*, **7**, 39-52.

Saunders, M.J., 1971: Cross polarization at 18 and 30 GHz due to rain. *IEEE Trans. on Antenna and Propagation.* **AP-19**, 273-277.

Seliga, T.A., and V.N. Bringi, 1976: Potential use of radar differential reflectivity measurements of orthogonal polarizations for measuring precipitation. *J. Appl. Meteor.*, **15**, 69-76.

Seliga, T.A., K. Aydin and V.N. Bringi, 1984: Differential reflectivity and circular depolarization ratio radar signals and related drop oscillation and propagation effects in rainfall. *Radio Sci.*, **19**, 81-89.

Seliga, T.A., R.G. Humphries, and J.I. Metcalf, 1987: Polarization diversity in radar meteorology: Early developments. *Battan Memorial and 40th Anniversary Conf. Radar Meteorology*, Boston, Amer. Meteor. Soc.

Semplak, R.A., 1974: Simultaneous measurements of depolarization by rain using linear and circular polarization at 18 GHz. *Bell Syst. Tech. J.*, **53**, 400-404.

Shupiatskii, A.B., 1959: Radar scattering by non-spherical particles. Tsentral'naia Aerologicheskaia Observatoriia, Trudy, No. **30**, 39-52.

Shupiatskii, A.B., and S.P. Morgunov, 1963: The application of polarization methods to radar studies of clouds and precipitation. Trudy Veseoiuzone Nauchi Meteorogcheskoi Soveshchania Leningrad, 295-305.

Stanley-Jones, M.L., A.S. Philipchuh and G.C. Cardinal, 1984: Field Site Radar Systems. Atmospheric Sciences Department Report 510-2/R2-0, Alberta Research Council, Edmonton, Alberta, Canada.

Stevenson, A.F., 1953: Electromagnetic scattering by an ellipsoid in the third approximation. *J. Appl. Phys.*, **24**, 1143-1151.

Stokes, G.G., 1901: Stokes' Mathematical and Physical Papers. Univ. Press, Cambridge.

Torlaschi, E., R.G. Humphries and B.L. Barge, 1984: Circular polarization for precipitation measurements. *Radio Sci.*, **19**, 193-204.

Van de Hulst, H.C., 1957: Light Scattering by Small Particles. John Wiley and Sons, Inc., New York, 470 pp.

Weltner K., J. Grosjean, P. Schuster, and W.J. Weber, 1986: Mathematics for Engineers and Scientists. Stanley Thornes Ltd. Great Britain.

Watson, P.A., and M. Arbabi, 1973: Rainfall cross polarization at microwave frequencies. *IEE Proc.*, **120**, 413-418.

Wexler, R., 1955: An evaluation of the physical effects in the melting layer. *Proc. 5th Weather Radar Conf.* Fort Monmouth, Amer. Meteor. Soc., 329-334.

APPENDIX A

Algorithm and Computer Programs Related to Phase Discriminator Calibration

A.1 Numerical Algorithm for Phase Shifter Method

In general, the output of port 3 or port 4 of the phase shifter method may be expressed as

$$P = A\sin(\theta + \gamma) + C, \tag{A.1}$$

where P is the output of port 3 or port 4 and θ is the phase shifter setting. A, γ, and C are the amplitude, phase offset,and zero offset respectively.

Given a set of $\{\ \theta_i,\ \hat{P}_i\ \}$ pairs, it is desired to determine A, γ and C for the best-fit curve of the form

$$P_i = A\sin(\theta_i + \gamma) + C. \tag{A.2}$$

The method of least squares (Weltner *et al.*, 1986) is used to develop the required equations for determining the three unknowns A, γ, and C. In our particular case, the sum of the squares of vertical deviations from the data points to the curve is minimized.

The error squared is defined by

$$E^2 = \sum_{i=1}^{n}(P_i - \hat{P}_i)^2, \tag{A.3}$$

where n is the number of data points.

Substituting for P_i from equation (A.2) gives

$$E^2 = \sum_{i=1}^{n} \left[A \sin(\theta_i + \gamma) + C - \hat{P}_i\right]^2, \tag{A.4}$$

which can be rewritten as

$$E^2 = \sum_{i=1}^{n} \left[D s_i + F c_i + C - \hat{P}_i\right]^2, \tag{A.5}$$

where

$$\begin{aligned} D &= A \cos \gamma, \\ F &= A \sin \gamma, \\ s_i &= \sin \theta_i, \\ c_i &= \cos \theta_i, \end{aligned}$$

For E^2 to be minimum, we must set

$$\frac{\partial E^2}{\partial D} = \frac{\partial E^2}{\partial F} = \frac{\partial E^2}{\partial C} = 0. \tag{A.6}$$

Hence

$$\frac{\partial E^2}{\partial D} = 2 \sum_{i=1}^{n} (D s_i + F c_i + C - \hat{P}_i) s_i = 0, \tag{A.7}$$

$$D \sum_{i=1}^{n} s_i^2 + F \sum_{i=1}^{n} c_i s_i + C \sum_{i=1}^{n} s_i - \sum_{i=1}^{n} \hat{P}_i s_i = 0, \tag{A.8}$$

$$\frac{\partial E^2}{\partial F} = 2 \sum_{i=1}^{n} (D s_i + F c_i + C - \hat{P}_i) c_i = 0, \tag{A.9}$$

$$D\sum_{i=1}^{n} s_i c_i + F\sum_{i=1}^{n} c_i^2 + C\sum_{i=1}^{n} c_i - \sum_{i=1}^{n} \hat{P}_i c_i = 0, \tag{A.10}$$

$$\frac{\partial E^2}{\partial C} = 2\sum_{i=1}^{n}(Ds_i + Fc_i + C - \hat{P}_i) = 0, \tag{A.11}$$

$$D\sum_{i=1}^{n} s_i + F\sum_{i=1}^{n} c_i + nC - \sum_{i=1}^{n} \hat{P}_i = 0. \tag{A.12}$$

Equations (A.8), (A.10), and (A.12) form a set of three equations from which the three unknowns D ($D = A\cos\gamma$), F ($F = A\sin\gamma$), and C can be determined.

This algorithm has been incorporated into the Fortran program SINE.

A.2 Listing of Program SINE

```
C
C     ............................................................
C
C     PROGRAM SINE DETERMINES THE BEST-FIT CURVE TO THE
C     PORT 3 OR PORT 4 PHASE SHIFTER CALIBRATION DATA.
C
C     INPUT PARAMETERS
C        NUM   = NUMBER OF DATA POINTS
C        THETA = PHASE SHIFTER SETTING, DEG
C        P     = RAW DATA VALUE OF PORT 3 OR PORT 4
C
C     OUTPUT PARAMETERS
C        AMP   = AMPLITUDE
C        PHASE = PHASE OFFSET
C        F     = ZERO OFFSET
C
C     ............................................................
C
      DIMENSION THETA(50),P(50),A(3,3),B(3,1),WK(9)
C
C     READ IN NUMBER OF DATA POINTS IN SERIES, NUM
      READ(5,100) NUM
  100 FORMAT(I4)
C
C     READ IN ANGLES (THETA) AND CORRESPONDING DATA VALUE (P)
      READ(5,101) (THETA(I),P(I),I=1,NUM)
  101 FORMAT(2F8.2)
C
C     CONVERT RAW DATA VALUES TO PORT 3 OR 4 VALUES USING
C               CV=(RDV/1.6)-64.0
C
      DO 10 I=1,NUM
      P(I)=(P(I)/1.6)-64.0
   10 CONTINUE
C
      SI=0.0
      CI=0.0
      SISI=0.0
      CICI=0.0
      SICI=0.0
      PISI=0.0
      PICI=0.0
      PI=0.0
C
C     COMPUTE SUMS
C
      PI=3.141592654
C     RAD=PI/180.
      RAD=0.017453292
      DO 3 I=1,NUM
C
C     SI=SUM OF SIN(THETA(I))
      SI=SI+SIN(RAD*THETA(I))
C
C     CI=SUM OF COS(THETA(I))
      CI=CI+COS(RAD*THETA(I))
C
C     SISI=SUM OF SIN(THETA(I))*SIN(THETA(I))
```

```
      SISI=SISI+SIN(RAD*THETA(I))*SIN(RAD*THETA(I))
C
C     CICI=SUM OF COS(THETA(I))*COS(THETA(I))
      CICI=CICI+COS(RAD*THETA(I))*COS(RAD*THETA(I))
C
C     SICI=SUM OF SIN(THETA(I))*COS(THETA(I))
      SICI=SICI+SIN(RAD*THETA(I))*COS(RAD*THETA(I))
C
C     PISI=SUM OF P(I)*SIN(THETA(I))
      PISI=PISI+P(I)*SIN(RAD*THETA(I))
C
C     PICI=SUM OF P(I)*COS(THETA(I))
      PICI=PICI+P(I)*COS(RAD*THETA(I))
C
C     PI=SUM OF P(I)
      PI=PI+P(I)
C
    3 CONTINUE
C
C     READ IN MATRIX OF COEFFICIENTS.
C
      A(1,1)=SISI
      A(1,2)=SICI
      A(1,3)=SI
      A(2,1)=SICI
      A(2,2)=CICI
      A(2,3)=CI
      A(3,1)=SI
      A(3,2)=CI
      A(3,3)=NUM
C
C     READ IN MATRIX OF CONSTANTS
C
      B(1,1)=PISI
      B(2,1)=PICI
      B(3,1)=PI
C
C     DEFINE IMSL PARAMETERS FOR SUBROUTINE LEQIF
C
      N=3
      MA=1
      IA=3
      IB=3
      M=1
      IJOB=0
C
      CALL LEQIF(A,IA,N,MA,B,IB,M,IJOB,WK,IER)
C
      D=B(1,1)
      E=B(2,1)
      F=B(3,1)
C
C     COMPUTE AMPLITUDE AMP = SQRT(D*D+E*E)
C
      AMP=SQRT(D*D+E*E)
C
C     COMPUTE PHASE ANGLE, BETA = ACOS(D/A), ASIN(E/A)
C
```

```
      BCOS=ACOS(D/AMP)
      BCOS=BCOS/RAD
C
C     BSIN=ASIN(E/AMP)
      BSIN=BSIN/RAD
C     CHECK WHICH PHASE ANGLE IS CORRECT
C
      IF (BCOS.LT.0.0) BCOS=BCOS+360.0
      BCOSA=360.0-BCOS
      ECHK=AMP*SIN(RAD*BCOS)
      IF(ABS(E-ECHK).LT.1.0) PHASE=BCOS
      ECHK=AMP*SIN(RAD*BCOSA)
      IF(ABS(E-ECHK).LT.1.0) PHASE=BCOSA
      IF(PHASE.EQ.0.0) WRITE(6,99)
   99 FORMAT(' NO UNIQUE PHASE ANGLE - CHECK CAREFULLY!')
C
      WRITE(7,200) AMP,F,PHASE
  200 FORMAT(' AMPLITUDE=',F7.3,',OFFSET=',F7.3,
     1 ', PHASE ANGLE=',F7.3,/)
C
C     WRITE OUTPUT
C
      WRITE (7,300)
  300 FORMAT(' THETA  RDV      CV  CURVE',/)
C
      DO 20 I=1,NUM
      FIT=AMP*SIN((THETA(I)+PHASE)*RAD)+F
      RDV=(P(I)+64.0)*1.6
      WRITE(7,400) THETA(I),RDV,P(I),FIT
  400 FORMAT(1X,F4.0,2X,F5.1,2X,F5.1,1X,F5.1)
   20 CONTINUE
      STOP
      END
```

A.3 Listing of Program GAMMA

```
C
C     ................................................................
C
C     PROGRAM GAMMA COMPARES THE MONITOR CALIBRATION
C     DATA WITH THE BEST-FIT OBTAINED USING BOTH POSSIBILITIES
C     OF GAMMA' (EQUATIONS 4.9 AND 4.10) AND CHOOSES THAT
C     WHICH MINIMIZES THE MEAN SQUARE ERROR. THIS PROGRAM
C     CAN BE USED FOR PORT 3 OR PORT 4 DATA.
C
C     INPUT PARAMETERS:
C        AN    = AMPLITUDE
C        GN    = PHASE OFFSET
C        CN    = ZERO OFFSET
C        P     = RAW DATA VALUE OF PORT 3 OR PORT 4
C        ALPHA = ORIENTATION OF THE DIPOLE SCATTERER
C
C     OUTPUT PARAMETERS:
C        SQ1= MEAN SQUARE ERROR FOR FIRST POSSIBILITY
C        SQ2= MEAN SQUARE ERROR FOR SECOND POSSIBILITY
C
C     ................................................................
C
      PI=3.141592654
C
C     READ IN AMPLITUDE AN, PHASE ANGLE GAMAN, AND OFFSET CN
      TYPE 1000
 1000 FORMAT('$ ENTER AMPLITUDE, PHASE ANGLE AND ',
     1 'OFFSET (WITH BLANKS IN BETWEEN)',/)
      READ(5,*) AN,GN,CN
      GN1=180.+GN
      GN2=-GN
      WRITE(6,1002) GN1,GN2
 1002 FORMAT(' GAMA PRIME = ', F7.2,' OR ',F7.2)
C
      SQ1=0.0
      SQ2=0.0
C
C     READ IN MINIMUM MAXIMUM AND DELTA ALPHA''
      TYPE 1001
 1001 FORMAT('$ ENTER MINIMUM, MAXIMUM AND DELTA ALPHA')
      TYPE 1005
 1005 FORMAT('$ ENTER "999. 0. 0." FOR IRREGULARLY SPACED DATA',/)
      READ (5,*) ALPHAO, ALPHAF, DALPHA
      IF (ALPHAO.EQ.999.) GO TO 3
      ALPHA=ALPHAO
      GO TO 1
    3 TYPE 1006
 1006 FORMAT(/,'$ ENTER ALPHA VALUE (999. IF REACHED END): ')
      READ(5,*) ALPHA
      IF (ALPHA.EQ.999.) GO TO 2
C
C     COMPUTE P3 VALUE CORRESPONDING TO DELTA
C
    1 PN1=AN*SIN((2.*ALPHA+GN1)*PI/180.)+CN
      PN2=AN*SIN((2.*ALPHA+GN2)*PI/180.)+CN
C
C     ENTER OBSERVED PORT VALUE
C
```

```
      WRITE (6,1003) ALPHA
1003  FORMAT('$ ENTER OBSERVED PORT VALUE FOR ALPHA =',
     1 F5.0,': ')
      READ (5,*) P
      P=P/1.6-64.0
      SQ1=SQ1+(PN1-P)*(PN1-P)
      SQ2=SQ2+(PN2-P)*(PN2-P)
      IF(ALPHAO.EQ.999.) GO TO 3
      ALPHA=ALPHA+DALPHA
      IF(ALPHA.GT.ALPHAF) GO TO 2
      GO TO 1
    2 WRITE (6,1004) GN1,SQ1
1004  FORMAT(' SUM OF SQUARES FOR GAMA PRIME =',F7.2,
     1 ' IS ',F12.4)
      WRITE (6,1004) GN2,SQ2
      STOP
      END
```

APPENDIX B

Listing of Program JORTT

```
C
C     ......................................................................
C
C     PROGRAM JORTT COMPUTES J (CORRELATION) FOR GIVEN ORTT USING
C     EQUATION (4.24)
C
C     J=(1/ORTT)(E(ORTT*ORTT)-(1-ORTT*ORTT)K(ORTT*ORTT))
C
C     WHERE
C        K=COMPLETE ELLIPTIC INTEGRAL OF FIRST KIND
C        E=COMPLETE ELLIPTIC INTEGRAL OF SECOND KIND
C
C     THE ELLIPTIC INTEGRALS ARE COMPUTED USING IBM SUBROUTINE DCEL2.
C
C     ......................................................................
C
      IMPLICIT REAL*8 (A-Z)
      INTEGER IER,I,IORTT
      WRITE(7,100)
  100 FORMAT(' ',' ORTT  ','  J',/)
C
C     COMPUTE J FOR ORTT=0.05 TO 1.00
      DO 10 IORTT=1,20
      ORTT=IORTT/20.0
      ORTT2=ORTT*ORTT
C
C     EORTT2= E(ORTT*ORTT) = COMPLETE ELLIPTIC INTEGRAL OF SECOND KIND
C     KORTT2= K(ORTT*ORTT) = COMPLETE ELLIPTIC INTEGRAL OF FIRST KIND
C
      A=1
      B=1-ORTT*ORTT
      CALL DCEL2(EORTT2,ORTT,A,B,IER)
      B=1
      CALL DCEL2(KORTT2,ORTT,A,B,IER)
      J=EORTT2-(1-ORTT2)*KORTT2
      J=J/ORTT
      WRITE(7,200) ORTT,J
  200 FORMAT(' ',F5.2,F10.5)
   10 CONTINUE
      STOP
      END
C
C     ......................................................................
C
C     SUBROUTINE DCEL2
C
C     PURPOSE
C        COMPUTES THE GENERALIZED COMPLETE ELLIPITIC INTEGRAL
C        OF SECOND KIND.
C
C     USAGE
C        CALL DCEL2(RES,AK,A,B,IER)
C
C     DESCRIPTION OF PARAMETERS
C        RES   -  RESULT VALUE OF DOUBLE PRECISION
C        AK    -  MODULUS (INPUT) IN DOUBLE PRECISION
C        A     -  DOUBLE PRECISION CONSTANT TERM IN NUMERATOR
C        B     -  DOUBLE PRECISION FACTOR OF QUADRATIC TERM
```

```
C                  IN NUMERATOR
C            IER   -  RESULTANT  ERROR CODE WHERE
C                  IER=O NO ERROR
C                  IER=1 AK NOT IN RANGE OF -1 TO +1
C
C         REMARKS
C            FOR AES(AK) GE 1 THE RESULT IS SET TO 1.E75 IF B IS
C            POSITIVE, TO -1.E75 IF B IS NEGATIVE.
C            SPECIAL CASES ARE
C            K(K) OBTAINED WITH A = 1, B = 1
C            E(K) OBTAINED WITH A = 1, B= CK*CK WHERE CK IS
C            COMPLEMENTARY MODULUS.
C            B(K) OBTAINED WITH A = 1, B = C
C            C(K) OBTAINED WITH A = C, B= 1
C            WHERE K, E, B, C DEFINE SPECIAL CASES OF THE GENERALIZED
C            COMPLETE ELLIPTIC INTEGRAL OF SECOND KIND IN THE USUAL
C            NOTATION, AND THE ARGUMENT K OF THESE FUNCTIONS MEANS
C            THE MODULUS.
C
C         SUBROUTINES AND FUNCTION SUBPROGRAMS REQUIRED
C            NONE
C
C         METHOD
C            DEFINITION
C            RES=INTEGRAL(A*B*T*T)/(SQRT((1+T*T)*(1+CK*T)**2))*(1+T*T))
C            SUMMED OVER T FROM O TO INFINITY
C            EVALUATION
C            LANDENS TRANSFORMATION IS USED FOR CALCULATION.
C            REFERENCE
C            R. BULIRSCH, 'NUMERICAL CALCULATION OF ELLIPTIC INTEGRALS
C            AND ELLIPTIC FUNCTIONS', HANDBOOK SERIES SPECIAL FUNCTIONS,
C            NUMERISCHE MATHEMATIK, VOL. 7. , 1965, PP. 78-90.
C
C         ..............................................................
C
          SUBROUTINE DCEL2(RES,AK,A,B,IER)
          DOUBLE PRECISION RES,AK,A,B,GEO,ARI,AARI,BO,A1
          IER=O
          ARI=2.DO
          GEO=(0.5DO-AK)+0.5DO
          GEO=GEO+GEO*AK
          RES=A
          A1=A+B
          BO=B+B
          IF(GEO) 1,2,6
    1     IER=1
    2     IF(B) 3,8,4
    3     RES=-1.D37
          RETURN
    4     RES=+1.D37
          RETURN
    5     GEO=GEO*AARI
    6     GEO=DSQRT(GEO)
          GEO=GEO+GEO
          AARI=ARI
          ARI=ARI+GEO
          BO=BO+RES*GEO
          RES=A1
```

```
      BO=BO+BO
      A1=BO/ARI+A1
      IF(GEO/AARI-0.999999995D0) 5,7,7
    7 RES=A1/ARI
      RES=RES+0.57079632679489662*RES
    8 RETURN
      END
```

APPENDIX C

Representation of Circular Polarization in Terms of p and β

The Cartesian coherency matrix, as defined by equation (1.23), is

$$\mathbf{J} = \frac{I}{2}\begin{pmatrix} 1 + p\cos 2\alpha \sin 2\beta & p(\sin 2\alpha \sin 2\beta + j\cos 2\beta) \\ p(\sin 2\alpha \sin 2\beta - j\cos 2\beta) & 1 - p\cos 2\alpha \sin 2\beta \end{pmatrix}. \qquad \text{(C.1)}$$

The circular coherency matrix is obtained by using the unitary transformation (Azzam and Bashara, 1977)

$$\mathbf{J}' = \mathbf{U}\mathbf{J}\mathbf{U}^{-1}, \qquad \text{(C.2)}$$

where

$$\mathbf{U} = \frac{1}{\sqrt{2}}\begin{pmatrix} 1 & -j \\ 1 & j \end{pmatrix}. \qquad \text{(C.3)}$$

The combination of equations (C.1), (C.2), and (C.3) gives

$$\mathbf{J}' = \frac{I}{2}\begin{pmatrix} 1 - p\cos 2\beta & p(\sin 2\alpha \sin 2\beta - j\cos 2\beta) \\ p(\sin 2\alpha \sin 2\beta + j\cos 2\alpha \sin 2\beta) & 1 + p\cos 2\beta \end{pmatrix}, \qquad \text{(C.4)}$$

which can be rewritten as

$$\mathbf{J}' = \frac{I}{2}\begin{pmatrix} 1 - p\cos 2\beta & p\sin 2\beta e^{-2j\alpha} \\ p\sin 2\beta e^{2j\alpha} & 1 + p\cos 2\beta \end{pmatrix}. \tag{C.5}$$

Using McCormick's (1968) notation, the circular coherency matrix may be expressed as

$$\mathbf{J}' = \begin{pmatrix} W_1 & W^* \\ W & W_2 \end{pmatrix}. \tag{C.6}$$

The comparison of equations (C.5) and (C.6) leads to

$$I = W_1 + W_2 \tag{C.7}$$

$$W_2 = \frac{I}{2}(1 + p\cos 2\beta), \tag{C.8}$$

$$CDR = 10\log_{10}\frac{W_1}{W_2} = 10\log_{10}\left(\frac{1 - p\cos 2\beta}{1 + p\cos 2\beta}\right), \tag{C.9}$$

$$ORTT = \frac{|W|}{\sqrt{W_1 W_2}} = \frac{|p\sin 2\beta|}{(1 - p^2\cos^2 2\beta)^{\frac{1}{2}}}, \tag{C.10}$$

$$ALD = \frac{1}{2}(\arg W - \pi) = \alpha, \tag{C.11}$$

$$Z_{DR}^c = 10\log_{10}\frac{1 + \frac{2\mathrm{Re}(W/W_2)}{1 + W_1/W_2}}{1 - \frac{2\mathrm{Re}(W/W_2)}{1 + W_1/W_2}} = 10\log_{10}\frac{1 + p\sin 2\beta}{1 - p\sin 2\beta}. \tag{C.12}$$

Now from equation (C.10), it can be shown that

$$\beta = \frac{1}{2} \arctan \left[\frac{2|W|}{(W_2 - W_1)} \right]; \qquad \text{(C.13)}$$

The degree of polarization p, as defined by equation (1.15), is

$$p = \sqrt{1 - \frac{4 \det|\mathbf{J}|}{(\mathrm{Tr}|\mathbf{J}|)^2}}, \qquad \text{(C.14)}$$

which upon substitution for $\mathrm{Tr}|\mathbf{J}|$ and $\det|\mathbf{J}|$ from equation (C.6) becomes

$$p = \sqrt{1 - \frac{4(W_1 W_2 - |W|^2)}{(W_1 + W_2)^2}}. \qquad \text{(C.15)}$$